NOVEL HONEYCOMB NANOSTRUCTURES FOR ENERGY STORAGE AND NANOSCALE DEVICE DESIGN

A DISSERTATION SUBMITTED TO
THE GRADUATE SCHOOL OF ENGINEERING AND SCIENCE
OF BILKENT UNIVERSITY
IN PARTIAL FULFILLMENT OF THE REQUIREMENTS FOR
THE DEGREE OF
DOCTOR OF PHILOSOPHY
IN
MATERIALS SCIENCE AND NANOTECHNOLOGY

By
Veli Ongun Özçelik
June, 2015

Novel Honeycomb Nanostructures for Energy Storage and Nanoscale Device Design

By Veli Ongun Özçelik

June, 2015

We certify that we have read this thesis and that in our opinion it is fully adequate, in scope and in quality, as a dissertation for the degree of Doctor of Philosophy.

Prof. Dr. Salim Çıracı(Advisor)

Asst. Prof. Dr. Aykutlu Dana

Assoc. Prof. Dr. Ceyhun Bulutay

Prof. Dr. Mehmet Cankurtaran

Asst. Prof. Dr. Olcay Üzengi Aktürk

Approved for the Graduate School of Engineering and Science:

Prof. Dr. Levent Onural
Director of the Graduate School

ABSTRACT

NOVEL HONEYCOMB NANOSTRUCTURES FOR ENERGY STORAGE AND NANOSCALE DEVICE DESIGN

Veli Ongun Özçelik
Ph.D. in Materials Science and Nanotechnology
Advisor: Prof. Dr. Salim Çıracı
June, 2015

This thesis presents a variety of new two dimensional honeycomb-like structures and heterostructures; the main objective being to determine their fundamental electronic, magnetic, mechanical and optical properties for new device and material design. Utilization of existing two dimensional materials for nanoscale device design, understanding the fundamental properties of their composite structures, explaining the existing data on known two dimensional materials and using computational simulations to discover new materials are the main concerns of this thesis.

We begin by assessing the validity of density functional theory on monolayer composites of graphene and boron nitride. We show that it is possible to grow vertical graphene / boron nitride heterostructures on top of each other and reveal the growth mechanisms at the atomistic level. We then utilize this vertical heterostructure for a nanoscale capacitor design by applying an external electric field. We test and show how first principles methods can be used to investigate the properties of materials under electric field. After explaining the reliable methods, capacitance values are calculated for the model for various thicknesses, which show quantum mechanical size effects at small separations that recede as the separations get larger; as the later is confirmed by experimental observations.

The next part of the thesis, investigates the electronic properties of lateral graphene / boron nitride heterostructures, and show how these composites act differently depending on the concentrations of graphene and boron nitride in the composite system. Namely, different behaviors of alloys, δ-doping and line compounds are revealed. Following this, these lateral heterostructures are utilized as nanoscale planar capacitors for atomically thin circuitry.

As a final remark on carbon and boron nitride nanocomposites, the next chapter of this thesis describes the growth mechanisms of one dimensional carbon/boron nitride short atomic chains and show their stabilities at elevated

temperatures. The electronic and magnetic properties of these chains exhibit even/odd disparity depending on the number of atoms in the chain. These chains also construct another two dimensional allotrope of graphene, namely graphyne, when connected to each other on the same plane. The properties of graphyne and its boron nitride analogue described in the following chapter introduces a new monolayer allotrope of carbon and boron nitride.

The following chapter turns to silicon and germanium analogue of graphene, silicene and germanene. Dumbbell type reconstructions of silicene and germanene are introduced, which lead to layered silicene and germanene. Dumbbell units introduced here form the fundamental building blocks of experimentally observed layered silicene and germanene.

The last chapter of the thesis looks at new material design and prediction studies based on computational simulations. Oxygenated silicene leads to a new monolayer piezoelectric material called silicatene. Finally, the monolayer structures of Group V elements nitrogen and antimony are also shown to be stable by phonon calculations and high temperature molecular dynamics simulations.

Keywords: Honeycomb structure, nanocapacitor, enery storage, material prediction, DFT, graphene, graphyne, silicene, germanene, phosphorene, nitrogrene.

ÖZET

ENERJİ DEPOLAMA VE NANO ÖLÇEKTE CİHAZ TASARIMI İÇİN YENİ BAL PETEĞİ NANO YAPILAR

Veli Ongun Özçelik
Malzeme Bilimi ve Nanoteknoloji, Doktora
Tez Danışmanı: Prof. Dr. Salim Çıracı
Haziran, 2015

Bu tez çalışması, çeşitli yeni iki boyutlu balpeteği yapıların elektronik, manyetik, mekanik ve optik özelliklerini ortaya koyarak bu yapıların nano ölçekte yeni cihaz tasarımı için kullanılabilirliklerinin yoğunluk fonksiyoneli teorisi ile incelenmesini kapsamaktadır. Ayrıca, kuantum mekaniksel moleküler dinamik simülasyonları ve fonon analizleri yardımıyla yeni iki boyutlu malzeme öngörüleri ve mevcut iki boyutlu malzemelerin muhtemel yeni kararlı fazları detaylı olarak incelenmiştir.

İlk olarak, yoğunluk fonksiyoneli teorisiyle geliştirilen hesaplama yöntemleriyle iki boyutlu grafen ve boron nitrat kompozit malzemeleri incelenerek, dikey ve yatay grafen / boron nitrat kompozitlerinin büyüme adımları gösterilmiştir. Daha sonra, bu kompozit malzemelere dışardan elektrik alan uygulanarak, bu sistemlerde depolanan enerji ve elektriksel yük değerleri hesaplanmıştır. Dolayısıyla, grafen / boron nitrat kompozit malzemelerin yüksek performaslı nanokapasitör olarak kullanılabiliecekleri gösterilmiştir. Bu nanokapasitörler, geniş boyutlarda klasik kapasitörler gibi davranmalarına karşın, boyutları nano ölçeğe indirilidiğinde kuantum mekaniksel davranışlar sergilemektedirler. Tezin daha sonraki bölümünde, düzlemsel olarak büyütülen grafen / boron nitrat kompozit malzemelerinin çeşitli özelliklerinin, kompozit içinde bulunan grafen veya boron nitrat miktarına göre nasıl değiştiği incelenmiştir. Farklı kombinasyonlar kullanılarak alaşımlar, çizgisel kompozitler ve ince katkılama tarzı malzemeler elde edilerek bunların atom inceliğinde devrelerde kullanım için özellikleri hesaplanmıştır.

Ayrıca, karbon / boron nitrat nano kompozitlerinin kısa atomik zinciler şeklinde büyümeleri incenerek, bu zincirlerin yüksek sıcaklıklarda bozulmadan kararlı olarak kalabildikleri gösterilmiştir. Zincirlerin elektronik ve manyetik özelliklerinin zincirdeki atom sayısına göre çift / tek disparitesi gösterdiği gözlemlenmiştir. Ayrıca, bu zincirlerin düzlemsel olarak birleştirilmesi sonucu elde edilen ve yeni bir iki boyutlu malzeme olan alfa-grafen yapısının kararlılığı

fonon analizleriyle ispatlanmıştır.

Tezin son iki bölümünde grafenin silikon, germanyum, azot ve antimon benzerleri incelenmiştir. İki boyutlu silikon ve germanyum yapılarında oluşan kafes tarzı yeni geometrik yapılar ortaya konularak, bu kafes yapısının tabakalı silikon ve germanyum elde edilmesinde temel unsur olduğu gösterilmiştir. Tezin son bölümünde, yeni malzeme tasarımı ve öngörüleri üzerinde durularak, iki boyutlu silika, iki boyutlu azot ve antimon bal peteği benzeri yapılarının kararlı geometrileri ve bu yapıların özellikleri açıklanmıştır.

Anahtar sözcükler: Bal peteği yapı, nanokapasitör, enerj depolama, malzeme öngörüsü, yoğunluk fonksiyoneli teorisi.

Acknowledgement

I would like to thank my supervisor Prof. Salim Çıracı; for his continuous support, encouragement and motivation throughout my graduate years at Bilkent. I am grateful to him not only for the preparation for this thesis but also for his guidance in my academic and intellectual life. I also acknowledge the professors of UNAM and Physics Department for their kind help and support during my PhD studies. I also thank my research group members Can Ataca, Mehmet Topsakal, Hasan Sahin and Seymur Cahangirov for their friendship and advices.

Contents

List of Figures

List of Tables

Chapter 1

Introduction

Investigating the fundamental physical effects at nanoscale underlying various electronic, magnetic, mechanical and optical observable macroscopic properties has always been one of the main goals of condensed matter physics. This has attracted interest of physicists not only because of the thought provoking behavior of physical laws at nanoscale which most of the time challenge one's common sense and expectations, but also for the possibility of making new technological discoveries based on these fundamental principles. With this regard, the purpose of theoretical and computational studies in materials science can be grouped into three main categories: (i) Describing the physics behind existing experimental data using first-principle laws, (ii) proposing ways of utilizing the existing materials data for new technologies and device designs, and (iii) using first-principles quantum mechanical computations to predict the existence of new materials that can be synthesized experimentally under specific conditions, but which do not exist in nature since they correspond to a local energy minimum on the Born-Oppenheimer surface. This thesis focuses on two dimensional honeycomb materials and their heterostructures for presenting novel results in all of these three categories. For this purpose, graphene / boron nitride heterostructures, the contenders of graphene like the mono-layers of Group-IV (silicene and germanium) and Group-V (nitrogen and antimony) atoms, their alloys, compounds and reconstructed structures have been the subject of this thesis.

Discovery of the two-dimensional allotrope of carbon, graphene, was a milestone in materials science. Graphene with its one-atom-thick stable structure in the honeycomb lattice, provides a plethora of exciting properties. It was a milestone not only because of its one-atom-thick structure, but also because it provided a medium where quantum effects at nanoscale can be tested and observed directly. Graphene is the thinnest, strongest and the most durable material with high electron hole mobility and high thermal conductivity. Its mechanical strength, chemical stability, unique electronic and magnetic properties have made graphene a material of interest in diverse fields ranging from biotechnology to electronics. Dirac cones provided by the linearly crossing π and π^* bands underlie various exceptional properties where electrons act as massless Dirac fermions on graphene like relativistic particles do in quantum electrodynamics. Under high magnetic fields and relatively low temperatures it is possible to observe quantum hall effect on graphene. Therefore, all of these rich and superior properties of graphene attract the attention of scientists from diverse fields and makes graphene the wonder material in an interdisciplinary platform [1, 2, 3].

Most of the superior electronic and mechanical properties of graphene originate from its honeycomb structure. The hexagonal honeycomb pattern seen in graphene often appears in nature in various places from the shells of turtles, to the capillary network of alveoli in human lung and of course in the wax cells built by bees. This is related to the fact that hexagonal honeycomb structure has the smallest perimeter to area ratio among all other two dimensional geometries that can completely fill the two dimensional surface without a gap, making it the most compact and stable two dimensional pattern. Thus the choice made by nature is the strongest and the most economical way of arranging atoms in two dimensional surface, as also stated by Darwin as "the comb of the bee, as far as we can see, is absolutely perfect in economizing labor and wax."[4] In addition, the honeycomb network made by planar sp^2 hybrid orbitals of carbon atoms acquire furher stability. Thus, if any other element is going to have a two-dimensional allotrope, the most probable geometry it is going to acquire is a honeycomb or slightly distorted honeycomb-like pattern. For this purpose, possible honeycomb-like patterns of other elements and their mixtures have been investigated after the synthesis of graphene. Among these, planar hexagonal boron nitride(BN) was revealed which has an ionic honeycomb structure consisting of alternatively bonded boron and nitrogen atoms[5, 6]. Despite the structural similarity, hexagonal BN differs from graphene with its wide band gap and dielectric properties[7]. Various

boron nitride structures like nanosheets[8], nanotubes[9] and nanowires[10] have already been synthesized. Also, recent studies show that hexagonal BN can be used to enhance the properties of graphene transistors by improving the mobility of electrons in graphene as compared to graphene films on silicon substrates[11]. These properties hold promise for novel technological applications of hexagonal BN structures.

Although graphene and hexagonal boron nitride has different electronic properties, they have similar honeycomb structures with only two percent lattice mismatch. This makes it possible to combine these two materials with minimum internal stress for obtaining different classes of materials with diverse properties that emerge when carbon atoms mix with boron nitride. Recently, hexagonal BN sheets were synthesized experimentally on Cu substrate by chemical vapor deposition method where ammonia borane ($NH_3 - BH_3$) and methane (CH_4) were used as precursors of boron nitride and carbon, respectively[12]. It was also shown that is possible to pattern boron nitride - carbon films lithographically for device fabrication, where atomic force microscopy and high resolution transmission electron microscopy images confirmed the formation of layered boron nitride - carbon films with high quality. Other groups have also succeeded to synthesize graphene on top of boron nitride using various experimental methods such as the mechanical transfer method[11, 13], direct growth using a bottom-up approach with chemical vapor deposition (CVD)[14] and plasma-enhanced CVD process with further improved quality. Additionally, direct growth of large are graphene on multilayered BN films are also reported[15]. Finally, a method for the production of lateral in-plane two dimensional heterostructures of graphene - BN mixtures was also reported by the Ajayan group in 2010 [12], where high resolution transition electron microscopy images confirmed the synthesized structures. Having succeeded this, the same group also proposed an experimental recipe for controlling the composition ratio of boron nitride - graphene heterostructures topologically, where certain regions of graphene sheets were converted into boron nitride in a controllable fashion using topological substitution reaction[16].

Thus, most of the experimental tools and methodology for creating various combinations of graphene - boron nitride allotropes in the desired geometry has been developed. Following this, in order to utilize these allotropes for new technologies, it becomes crucial to understand how the physical properties of the graphene / boron nitride system change depending on various geometries it can

have. Also, it is important to understand the experimentally observed growth mechanisms at the atomistic level. For this purpose, in the first part of this thesis, we investigate the growth mechanisms of epitaxial graphene on boron nitride at the atomistic level. This is followed by investigating the properties of various lateral heterostructures of planar graphene - boron nitride composite materials. We show how the electronic properties depend on geometry and ratio of carbon / boron nitride regions. After providing an understanding of these fundamental physical properties, we present how these lateral and vertical heterostructures can be utilized to construct nanoscale capacitors.

We showed that by applying electric field to graphene / BN heterostructures, it is possible to create a charge separation between the metallic graphene plates. The calculated stored charge, energy and potential difference between the metallic layers show that these nanocapacitor models have high gravimetric capacitances which are in the range of supercapacitors. We also show that as the size of the nanocapacitor model increases, it starts to act exactly like a classical capacitor. Thus, by an immediate application of density functional theory on our model, are able to observe quantum mechanical effects at nanoscale. Our results were further confirmed by following experimental studies [17] of other research groups. In chapters 7 and 8 we further investigate different graphene / boron nitride based nanostructures, namely atomic chains and graphyne constructed from chains, which is a newly proposed two dimensional contender of graphene.

In the following chapters of this thesis, we also investigate other two-dimensional materials which has gained increasing attention after the synthesis of graphene. Local reconstruction of silicene and germanene, which are silicon and germanium based analogues of graphene; oxygenation of silicene leading to a novel two dimensional piezoelectric auxetic material which we name as silicatene, and new phases of two dimensional silicene and germanene resulting from these reconstructions are investigated in chapters chapters 9 and 10. Silicatene, which forms upon the bonding of oxygen atoms between the silicon atoms in the honeycomb silicene structure exhibits interesting properties such as having a negative Poisson's ratio and having directional electronic properties. On the other hand, the dumbbell structure proposed here explains one of the interesting experimental result that lacked theoretical explanation: the formation of layered silicene on certain substrates, which is crucial for future silicon technology. The stability of layered silicene was explained by means of the dumbbell unit of silicon that

is revealed in this thesis. Furthermore, similar dumbbell structures are also proposed for germanium atoms, which might lead to layered germanene on suitable substrates.

Finally, we present the electronic, magnetic and mechanical properties newly proposed monolayers of Group V elements, nitrogen and antimony. Although not synthesized yet, our predictions prove the salabilities of these monolayers by means of first principles phonon calculations and molecular dynamics simulations at elevated temperatures. These 2D crystalline structure corresponds to local minima on the Born-Oppenheimer surface, since they have negative formation energies relative to N_2 molecule and bulk antimony. Therefore, we first carried out an extensive analysis and demonstrated that they are stable in a deep local minimum and maintain their structures above the room temperature as free standing, as well as on selected substrates. We characterized these novel materials and their nanoribbons by calculating their mechanical, electronic and magnetic properties. We also revealed bilayer and three dimensional (3D) layered structures.

Chapter 2

Method: Density Functional Theory

Along the with the rapid development in computational power, it became possible to solve fundamental equations of many body physics numerically with the help of modern architecture computers. However, the present computational power is not yet enough to solve these equations even for small systems containing only a few atoms. Therefore, valid approximations that give consistent results with experimental observations are implemented and tested continuously. Density functional theory (DFT), being the state of the art theory for investigating the atomistic mechanisms at nanoscale, approximated electrons as a single particle moving in an effective nonlocal potential. Thus, instead of solving the strongly interacting electron gas, this approach focuses on the density of electrons. In addition to this, it treats the nuclei adiabatically meaning that the nuclear and electronic coordinates are separated in the many-body wave function due to the large mass difference between the nucleus and the electrons which causes the electrons to respond to the same forces much faster than the nucleus. This approach, which is known as the Born-Oppenheimer approximation is the fundamental idea behind density functional theory method. In this chapter, we briefly summarize the fundamental aspects of density functional theory that are utilized in the following chapters on various systems.

2.1 Thomas-Fermi Method

Although it is not accurate enough for the electronic structure calculations of the current era, the initial density functional theory for quantum systems was proposed by Thomas and Fermi. In the Thomas-Fermi method, an explicit functional of density that is idealized as non-interacting electrons in a homogeneous gas with density equal to the local density at any given point is used to approximate the kinetic energy of a system. The exchange and correlations between electrons that is neglected in the Thomas-Fermi approach was later included by Dirac which leads to an energy functional for electrons as:

$$E[n] = C_1 \int d^3r n(\mathbf{r})^{5/3} + \int d^3r V_{ext}(\mathbf{r}) n(\mathbf{r}) + C_2 \int d^3r n(\mathbf{r}^{4/3}) + 0.5 \int d^3r d^3r' \frac{n(\mathbf{r}) n(\mathbf{r}')}{|\mathbf{r} - \mathbf{r}'|} \quad (2.1)$$

where $V_{ext}(\mathbf{r})$ is the external potential. Here, the first integral is the local approximation for the kinetic energy, the third integral is the local exchange and the last integral is the electrostatic Hartree energy where C_1 and C_2 are constants. After minimizing the energy functional for all possible values of $n(\mathbf{r})$ the ground state density and energy can be calculated. Here, the possible values of $n(\mathbf{r})$ should satisfy the condition:

$$\int d^3r n(\mathbf{r}) = N \quad (2.2)$$

Density functional theory is attractive because it provides remarkably simpler equation than the many-body Schrodinger equation which involves 3N degrees of freedom for N electrons. However, the simple Thomas-Fermi approach misses most of the essential physics since the approximations it uses are too immature. Although it can be used for system of electrons, it falls short for complete description of system of atoms.

2.2 Kohn-Sham Ansastz

A more accurate way to formulate the density functional theory was introduced by Hohenberg and Kohn using an exact theory of many-body system which can be applied to any group of interacting particles which are subjected to an external potential [18]. Hohenberg and Kohn proved two theorems which form the basis of the density functional theory. The first theorem states that for any system of interacting particles in an external potential, the potential is determined by the ground state particle density, except for a factor of constant. The second theorem follows this by stating that a universal functional for the energy in terms of density can be defined which is valid for any external potential. These theorems suggest that, all properties of the system can be completely derived from the ground state density and the energy functional itself is sufficient to determine the ground state density.

The idea of making clever approximations was further developed by the Kohn-Sham approach, which mainly replaces the difficult many-body Hamiltonian with a different system that can be solved numerically. The Kohn-Sham ansastz assumes that the ground state of the interacting system is equal to the density of the non-interacting system. As a result of this approximation, the system can be treated as a set of independent particles that can be solved exactly using computational numerical tools. For a set of doubly occupied electronic state, the Kohn-Sham Hamiltonian can be written as:

$$E[\psi_i] = 2\sum_i \int \frac{\hbar^2}{2m}\nabla^2\psi_i d^3r + \int V_{ion}(r)n(r)d^3r + \frac{e^2}{2}\int \frac{n(r)n(r')}{|r-r'|}d^3r d^3r' + E_{ex}[n(r)] + E_{ion}(R). \quad (2.3)$$

Here, E_{ion} is the Coloumb energy, V_{ion} is the total electron-ion potential, $n(r)$ is the electron density, E_{ex} is the exchange correlation functional and ψ_i is the wave function corresponding to the i^{th} electronic state such that

$$n(r) = 2\sum_i |\psi_i(r)|^2, \quad (2.4)$$

and

$$[\frac{\hbar^2}{2m}\nabla^2 + V_{ion}(r) + V_H(r) + V_{ex}(r)]\psi_i(r) = \epsilon_i\psi_i(r) \tag{2.5}$$

where $V_H(r)$ and $V_{ex}(r)$ are the Hartree and exchange correlation potentials respectively. These potentials can be mapped onto to each other using:

$$V_H(r) = e^2 \int \frac{n(r')}{|r - r'|} d^3r', \tag{2.6}$$

$$V_{ex}(r) = \frac{\delta E_{ex}[n(r)]}{\delta n(r)}. \tag{2.7}$$

Therefore, these equations must be solved self consistently. The initial guess of electronic states produces a density from which an electronic potential is calculated.

2.3 Exchange Correlation Energy

One of the methods for describing the exchange correlation energy of such a system is using the local density approximation (LDA). With this approximation, the exchange correlation energy functional depends only on the the value of the electronic density at each point in the space. Accordingly, the exchange correlation energy at a point in the electron cloud is assumed to be equal to the exchange correlation energy per electron in a homogeneous electron gas that has the same density at the same point. The inhomogeneities due to the neighboring interactions are ignored. Alternatively, these inhomogeneities can be taken into account by considering the gradient of the density at the same point, which results in the generalized gradient approximation (GGA). The choice of either of there approximations is valid depending on the purpose and the system of interest. In general, LDA mostly results in higher binding energies of atoms and activation energies in chemical reactions. On the other hand, GGA provides more accurate results for the prediction of molecular geometries and ground state energies. The

higher binding energies observed in LDA is corrected by GGA, but this correction sometimes may result in under-binding. GGA calculations give increased lattice constants and decreased bulk moduli, which is a result of the softening of bonds. These functionals can be further modified to include van der Waals interactions to give more accurate results of interlayer distances and long range interactions.

2.4 Choice of parameters

Although calculations are made simpler by means of using the discussed approximations, including all electrons of each atom into the unitcell is still very costly. Thus, pseudo-potentials that behave same with all electrons after a cut-off radius are implemented in practical calculations. In this theses, we implement mainly projected augmented wave (PAW) pseudo-potentials which use superposition of atomic orbital wave functions in the core regions. PAW potentials give specially accurate results for compound materials, magnetic states, alkali and alkali earth elements. In our calculations we mainly use the VASP software[19] for plane wave calculations where the PAW potentials are chosen accordingly. The PWSCF package[20] is also used in some cases to check accuracy using density functional perturbation theory, especially for vibrational analysis and phonon calculations. However, there are cases where the use of plane wave basis might give inaccurate results, for example in cases where we apply external electric field or charge the system externally.

Namely, the electronic potential under the applied electric field makes a dip in the vacuum spacing between repeating unitcells with a vacuum spacing between them when treated within the periodic boundary conditions. As the strength of the electric field increases, this dip is further lowered as if a quantum well and allows the plane wave basis set to have states confined to the well as the solution of the Hamiltonian. Once the energies of these confined states are lowered below the Fermi level they start to be occupied by electrons. As a result, the electrons are going to spill into the vacuum region under the external applied electric field. The spilling of the charge to the vacuum is clearly erroneous and unrealistic. These artifacts of plane wave basis set become even more critical for wide vacuum spacing. On the other hand narrow vacuum spacing is not desired since it gives rise to significant coupling between adjacent unitcells treated using

the supercell geometry. These artifacts can be eliminated by using basis set consisting of orbitals centered only at the atomic sites, which does not allow the states confined to the potential dip in the vacuum spacing. Thus, under such conditions, we carry out first-principles, spin-polarized calculations within density functional theory, where the eigen-states of Kohn-Sham Hamiltonian are expressed as linear combination of numerical atomic orbitals. In such cases, we use the SIESTA package[21] where local atomic orbital basis sets are implemented.

Once the choice of approximation (GGA or LDA), type of basis sets (local or plane-wave) and pseudo-potentials are made, we decide on the cut-off potential value and the number of **k**-points to be used. For both parameters, the convergence of the total energy of the system is tested by increasing the cut-off value and the number of **k**-points step by step. Once the number of **k**-points is determined for the primitive unitcell, it is scaled accordingly for larger unit-cells. Similarly, the choice of vacuum spacing of the unit-cells, the convergence for energy value, and the maximum forces acting on each atom for ionic relaxation are also tested for convergence. The corresponding values for these parameters depend on the system of choice, and indicated specifically in each of the following chapters separately. In addition, GW corrections and hybrid functionals are also implemented when necessary. In the GW approximation, the self-energy of the many-body system of electrons is calculated by expanding it in terms of single particle Green's function (abbreviated with G) and the screened Coulomb interaction (abbreviated with W. Here, the self energy is expanded in a Taylor series in powers of the screened interaction W.

Another crucial approximation that is made in the calculations is related to the van der Waals (vdW) interaction. Density functionals are unable to describe the vdW interactions accurately. On the other hand, a semi-empirical method is developed and shown to be successful at implementing the vdW interactions into the calculations. By considering the analytic solution of vdW interaction in solids, the Grimme method[22] implements this to DFT calculations as:

$$E_{DFT-D} = E_{DFT} + E_{disp}, \tag{2.8}$$

where

$$E_{disp} = -s_6 \sum_{i=1}^{N(at)-1} \sum_{j=i+1}^{N(at)} \frac{C_6^{ij}}{R_{ij}^6} f_{dmp}(R_{ij}) \tag{2.9}$$

Here, E_{DFT} is the usual self consistent DFT energy, E_{disp} is the emprical correction term, N(at) is the number of atoms in the unitcell, C_6^{ij} denotes the dispersion coefficient for atom pair and $C_6^{ij} = \sqrt{C^i C^j}$. C^i is the emprical constant that is different for every atom. s_6 is the global scaling factor that depends on the exchange correlation functional used in the calculation and R_{ij} is the interatomic distance. A damping function f_{dmp} is used in order to avoid near singularities for small distances.

Throughout this thesis, stabilty analysis was performed on several structures. The stability analysis was performed in three steps. The first step is finding the global energy minimum of a gven structure by simple DFT calculations where the lattice dimensions, atom positions and angles were changed untill achieving the lowest energy minimum. However, it is not always true that the lowest energy minimum leads to a stable configuration of atoms in the unitcell. Thus, as a second step, phonon calculations were performed. The phonon analysis were carried out using two different methods to check whether all vibrational frequincies are real or not. These methods are based on small displacement method[23] and density functional perturbation theory[24]. In the end of phonon calculations, if find that all of the vibrational frequincies are positive, it is a strong evidence for the stability of the material. However, this stabilty might me prone to disturbance at elavated temperatures. Therefore, as a third step, we perform ab-initio molecular dynamics simulations at elevated temperatures. We run these simulations for 5 to 10ps depending on the structure. Although this might look short, it is a long enough time scale for ab-initio calculations peformed at high temperatures like 1000K. The stability of the structures were tested at high temperatures by ab-initio, molecular dynamics calculations using two different approaches. In the first one, Nosé thermostat used and Newton's equations were integrated through Verlet algorithm with time step of 2 fs. In the second one, we scaled the velocities at each time step to keep the temperature constant.

Chapter 3

Epitaxial Growth of Graphene

3.1 Overview

The objective of this chapter is explaining the atomistic mechanisms taking place during the nucleation and epitaxial growth of graphene using ab-initio finite temperature molecular dynamics method. For this purpose, the growth of graphene is simulated with and without substrate. Various hypothetical growth scenarios are simulated and the effects of substrates on these scenarios are tested. Nucleation sites of growth are determined and their effects on the perfectness of graphene is investigated. For growth from the edge of a seed, external carbon monomers and dimers are sent to the seed and molecular dynamics simulations are performed at elevated temperatures. The defect concentration forming during growth, the healing patterns of these defects and energy barrier to heal these defects are explored on different substrates.

Synthesis of pristine epitaxial graphene has been the motivation of recent experimental and theoretical studies. The recent studies on graphene production processes can be grouped in two classes: one class includes the mechanically exfoliated graphene sheets where the graphene flakes are peeled from a bulk graphite substrate[1, 3, 25]. However, that method has the disadvantage of not being able to easily control the size and quality of the fabricated layer. The other class includes the direct growth of graphene flakes on substrates[26, 27]. It

was shown that epitaxial graphene is a suitable material for nanoscale electronic applications by growing ultra-thin graphite layer on silicon carbide by thermal decomposition[28].

3.2 Molecular Dynamics Simulation of Growth

We have performed atomic structure optimizations and ab-initio finite temperature molecular dynamics (MD) calculations within density functional theory (DFT) using VASP software.[19] The relaxed geometries of all structures were calculated by spin-polarized plane-wave calculations using projector augmented-wave (PAW) potentials[29] within generalized gradient approximation (GGA)[30] including van der Waals corrections.[22] The Brilliouin zone of the primitive unitcell of graphene was sampled by (17×17×1) k-points in Monkhorst-Pack scheme which was scaled according to the size of other unitcells.[31] The energy convergence value between two consecutive steps was chosen to be 10^{-5} eV. In ab-initio MD calculations the time step was taken 2.5 fs and the atomic velocities were renormalized to the temperature set at T=1300 K at every 40 time steps. The temperature of MD calculations is in compliance with the temperature used in chemical vapor deposition.

3.2.1 Growth without Template

In order to understand the effects of a template surface on graphene growth, we first consider a hypothetical situation and investigated the growth mechanism of graphene without any template (substrate). To bypass the initial nucleation process, a graphene flake was fixed in space and additional carbon atoms were sent to it in different scenarios, which mimic the growth. Simulations were done by letting the carbon atoms to move freely in a certain plane, while not allowing the out of plane motions. As shown in Fig. 3.1(a), we start with nanoribbons having armchair and zigzag edges. Initially, zigzag nanoribbon is composed of 24 atoms forming three zigzag chains in the periodic direction, two of which are kept fixed. Armchair nanoribbon starts with 20 atoms, 12 of which are kept fixed. Fixed atoms are delineated in Fig. 3.1(a). After running 1 ps of MD simulation

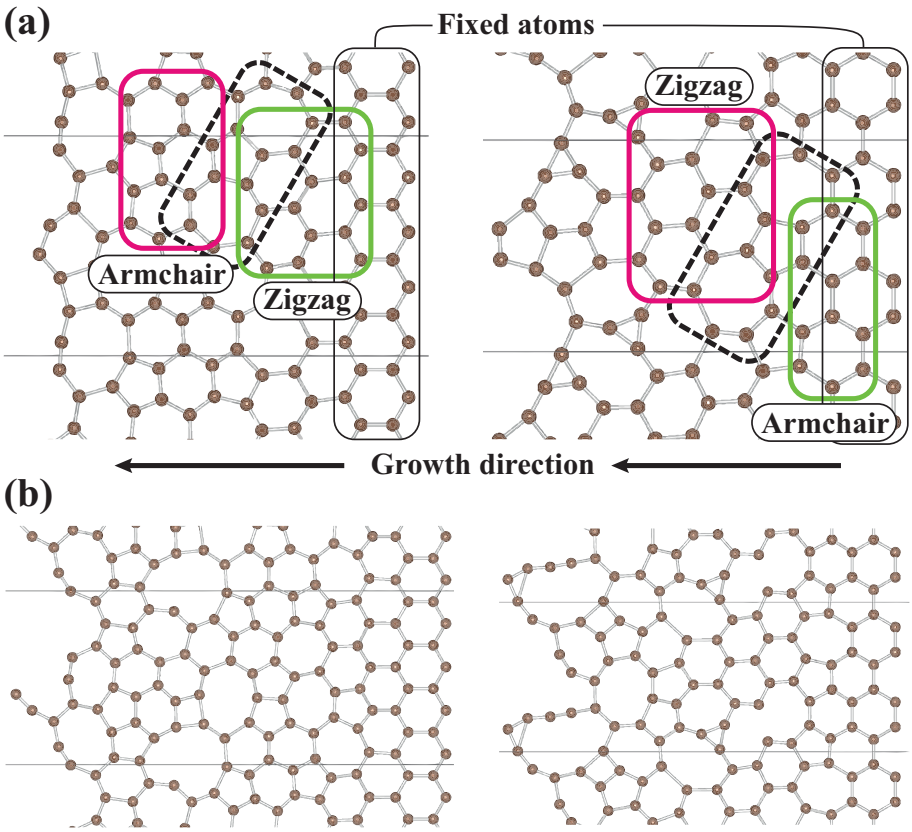

Figure 3.1: Snapshots from ab-initio MD simulations of planar graphene growth at T=1300 K without a template substrate. An initial flake was placed and in each 1 ps MD calculation two carbon atoms were sent from the left hand side to monitor the growth in the indicated direction. Each snapshot includes two periodic supercells. (a) Change of the armchair edge to zigzag edge and vice versa is shown. (b) Structures obtained when simulation of growth presented in (a) is proceeded. Formation of big rings and chains were observed, and the resulting structures were far away from being a perfect graphene layer. Note that defects formed in part (a) are still present in part (b).

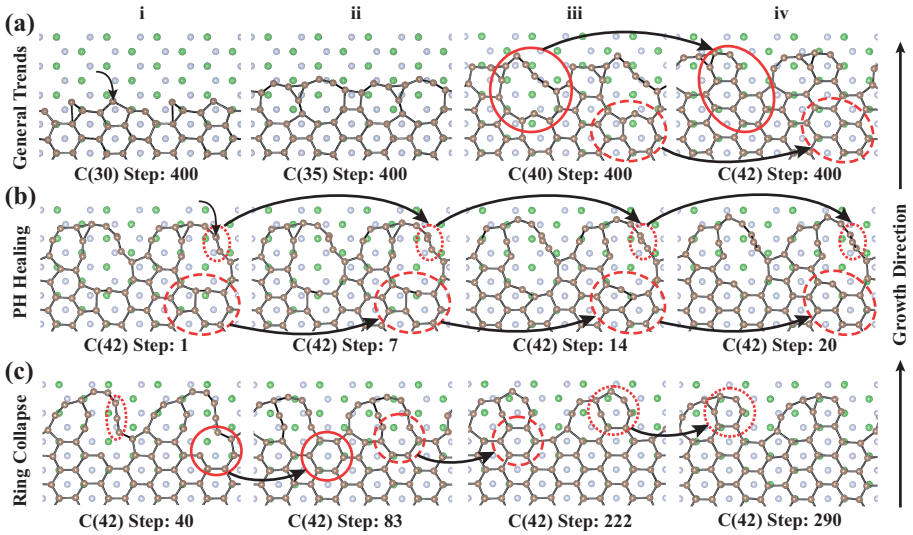

Figure 3.2: Snapshots from ab-initio MD simulation of epitaxial growth of graphene on a BN substrate. In the ball and stick model B, N and C atoms are represented by green, blue and brown balls while only bonds between carbon atoms having distance less than 2 Å are shown. Each snapshot includes two periodic supercells in the horizontal direction. (a) General trends are presented by including final configurations of MD calculations involving 30, 35, 40 and 42 carbon atoms. Some of the critical configurations in the evolution of ring collapse and defect healing mechanisms are highlighted by solid and dashed lines respectively. (b) Snapshots from the MD simulation of the structure having 42 carbon atoms taken after 1, 7, 14 and 20 MD steps. Carbon atom migration causing the growth of rings and defect healing can be traced in dotted and dashed circles, respectively. (c) Snapshots from the same MD simulation taken after 40, 83, 222 and 290 MD steps. Three subsequent hexagon formations are indicated by solid, dashed and dotted circles.

two more carbon atoms are introduced in both systems. These atoms are first positioned in the same plane to the left of the nanoribbons, where the edges are free to move in 2D. Then they are moved towards these edges until the distance between the newcoming atom and one of the edge atoms decreases to 1.3 Å. Then the new MD simulation is started and the process is repeated consecutively.

As seen in Fig. 3.1(a), during the growth simulation the orientation of the honeycomb parts are changed from zigzag to armchair (left panel) and vice versa (right panel). Interestingly, in both cases the transition is mediated by similar structures composed of two heptagons with one pentagon in the middle. One can attribute the defected growth to the absence of a substrate which would act as a stencil if the template had a structure similar to graphene. Carrying on the growth simulation of structures presented in Fig. 3.1(a) results in the massively defected network of carbon atoms as shown in Fig. 3.1(b). One can identify the big holes surrounded by carbon chains and patterns composed of pentagons and heptagons. It was observed that the defects that emerged at the beginning of the simulation are still present after about 40 ps of simulation. This implies that the process of growth induces defects mainly composed of pentagons and heptagons, which persist due to the absence of a healing mechanism. Several scenarios of growth simulation without a substrate were tested but none of them resulted in a reasonably ordered honeycomb structures. Especially, those simulations in which carbon atoms were allowed to move in all directions resulted in bulk-like structures and atomic chains. Although the observed chain structures are interesting, growth of regular honeycomb structure was not observed and we deduced the necessity of a template during the growth process to define a plane where the graphene like structure sits and where the newcoming carbon atoms are landed.

3.2.2 Graphene Growth on BN Substrate

3.2.2.1 Monomers

Hexagonal boron-nitride consists of single layers of BN in honeycomb structure, which is almost commensurate to graphene. Because of this reason we have chosen BN as a template on which we investigate the growth of graphene. Again,

to skip the initial nucleation process, a graphene flake was placed on BN substrate. Single carbon atoms were released from random positions on top of the graphene flake edges and molecular dynamics simulation were performed for 400 time steps before the next atom was sent. By sending the atoms one by one, events happening during the growth process were monitored at atomistic scale. The snapshots taken from this calculation are shown in Fig. 3.2. The bottom part of these structures normally comprises fixed graphene and BN substrate, which are not shown while growth proceeds upwards.

In Fig. 3.2(a) we present the general trends observed during growth. Each of the four snapshots in this row corresponds to the final structures obtained after the MD simulations of 30, 35, 40 and 42 carbon atoms on BN respectively. As seen in the first column of Fig. 3.2(a) first a single carbon atom indicated by a small arrow makes bonds with armchair edges and a pentagon structure is formed. This stretches the edges and prepares a medium for the formation of a neighboring heptagon. Then ring-like structures start to grow at the edges as seen in column two of Fig. 3.2(a). When the ring structure reaches a certain size, it collapses forming hexagonal structures at the graphene edges as shown in columns three and four.

The formation and healing of pentagon-heptagon defects, which is the second major mechanism affecting the growth process is presented in Fig. 3.2(b). The snapshots correspond to the 1^{st}, 7^{th}, 14^{th} and 20^{th} MD steps of the simulation with 42 carbon atoms. The healing of the PH defect is highlighted by dashed circles. As simulation proceeds to the 20^{th} step, the PH defect is totally relaxed into two hexagons. Note that, the healing of a PH defect at the edge is similar to the healing of a Stone-Wales (SW) defect, which involves rotation of the middle bond (which is common to two adjacent heptagons) by 90°. Here there is, however, a crucial difference in the path of healing as compared to that of SW healing, because one of the carbon atoms in the pentagon of the PH defect is bonded with two adjacent carbon atoms, whereas in the SW defect all carbons are bonded to three others. The absence of one of these bonds (or the presence of sp^2-type dangling bond) decreases the barrier of PH healing as compared to the SW case. This issue is revisited in forthcoming detailed discussions. We note the growing edge of grains is reminiscent of the grain boundary. The contact of an adjacent grain to the growing edge of graphene is expected to delay the healing of defects.

In Fig. 3.2(b), the dotted circle in the first column marks the inclusion of the newly added carbon atom which is added from a random position on top of the graphene layer. This newly added carbon atom is initially positioned on top of another carbon atom of the graphene structure. It then migrates to the bridge site and by replacing the bridge bond it increases the size of the carbon ring (column 2 to 4). As the ring expands with the inclusion of this new carbon atom, it reaches the critical size after which it collapses.

The process of ring collapse is shown in Fig. 3.2(c). The snapshots presented here correspond to the 40^{th}, 83^{rd}, 222^{th} and 290^{th} MD steps of the simulation with 42 atoms. Here the ring is composed of 14 carbon atoms before the collapse. This is just enough to form three hexagons highlighted by solid line in the fourth column of Fig. 3.2(a). As seen in Fig. 3.2(c), these three hexagons are consecutively formed during the collapse of the ring.

Calculations within GGA including van der Waals corrections and using PAW potentials predict the bridge site as the energetically most favorable site of adsorption with a binding energy of 1.7 eV. While the energy barrier for the migration of single, isolated carbon atom is only 0.37 eV, it is lowered and eventually collapsed when another carbon atom is located at close proximity. Both first-principles total energy and finite temperature MD calculations have shown that initially C_2 and eventually C_n carbon chains can form perpendicularly attached to graphene surface through inclusion of single carbon adatom one at a time. The gain of energy in the implementation of a single carbon adatom is $\sim$ 5 eV. However, the situation is dramatically different for a graphene sheet having armchair or zigzag edge: Single carbon atoms have shown to be attached favorably to the edge atoms with much larger binding energy (7.08 eV for armchair edge and 8.19 eV for zigzag edge). Further implementation of carbon adatoms to the edges gives rise to PH-like defect structures.

3.2.2.2 Dimers

Although single carbon adatoms are the smallest building blocks of graphene, the role of carbon dimers in graphene growth was also considered. The importance of carbon dimers is especially more apparent during the initial nucleation of graphene seeds due to their high mobility on certain transition metals. In our

model since we already have an initial graphene flake to which the adatoms can bind, we actually bypass the nucleation stage and directly study growth. Having studied the growth mechanisms triggered by carbon monomers, we next use carbon dimers as the building blocks. This time, we release carbon dimers from random positions on top of the graphene flake and perform molecular dynamics simulations as explained before. The snapshots taken from these simulations are presented in Fig. 3.3. In Fig. 3.3(a) we show the final structures obtained after 400 steps of MD simulation of 26, 30, 32 and 34 carbon atoms on BN respectively. It is seen that we have a less defected graphene growth in this case as compared to the defected structures presented in Fig. 3.2(a). However, as seen in columns (iii) and (iv) of Fig. 3.3(a), defects may still occur at the growing edge although less frequent as compared to growth with monomers. Just like the monomer case, we still have carbon rings forming and collapsing into PH defects as presented in Fig. 3.3(a).

Fig. 3.3(b) presents the migration of a carbon dimer on the graphene flake. Each of the four snapshots in this row corresponds to the 40^{th}, 180^{th}, 320^{th} and 400^{th} steps of the MD simulation with 34 carbon atoms. The dimer initially is bound to one of the carbon atoms on the defected graphene structure and forms a short segment of chain consisting of 3 carbon atoms. It then migrates towards the edge by bonding to another carbon atom of graphene each time and finally taking its horizontal position.

3.3 Healing Defects During Growth

Having noticed the role of PH defect healing in graphene growth, we move on by investigating the energetics and dynamics of SW and PH defect healing in free standing graphene, as well as graphene grown on BN and Ni(111) surfaces. Previous experimental studies have not shown any experimental evidence for the existence of SW defects in graphene. Although such defects can be observed by using tunneling electron microscopy(TEM), it was noted in previous studies that experimentally observed images of SW defects in graphene are results of electron beams which suggests that those defects are artifacts of the measurements.[32] In this section we calculate the energy barrier that needs to be overcame for the formation and healing of SW and PH defects. This barrier is significantly lower

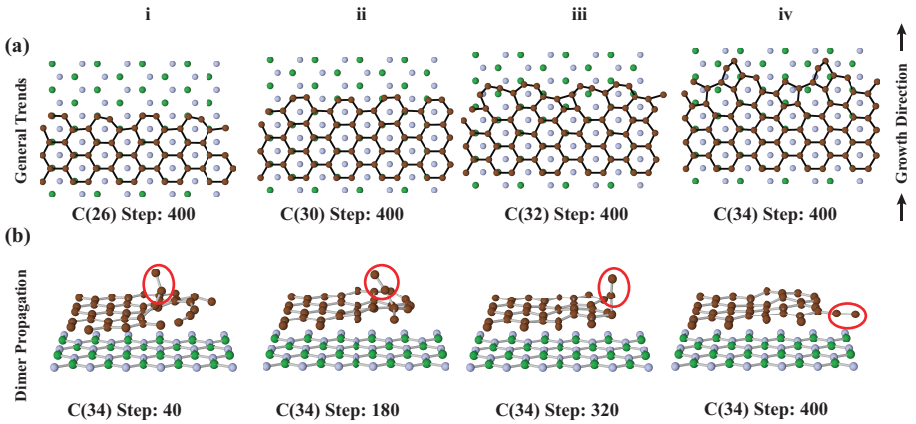

Figure 3.3: Snapshots from ab-initio MD simulation of epitaxial growth of graphene on BN when carbon dimers are used as building blocks. B, N and C atoms are represented by green, blue and brown balls. (a) The final configurations of MD simulations involving 26, 30, 32 and 34 carbon atoms. Graphene growth is less defected as compared to growth with monomers, but ring formation and PH defects still occur as seen in columns iii and iv. (b) Migration of a carbon dimer on graphene surface. The side view snapshots are from an MD simulation having 34 carbon atoms. The dimer moves to its final position each time by binding and detaching from a different carbon atom of graphene.

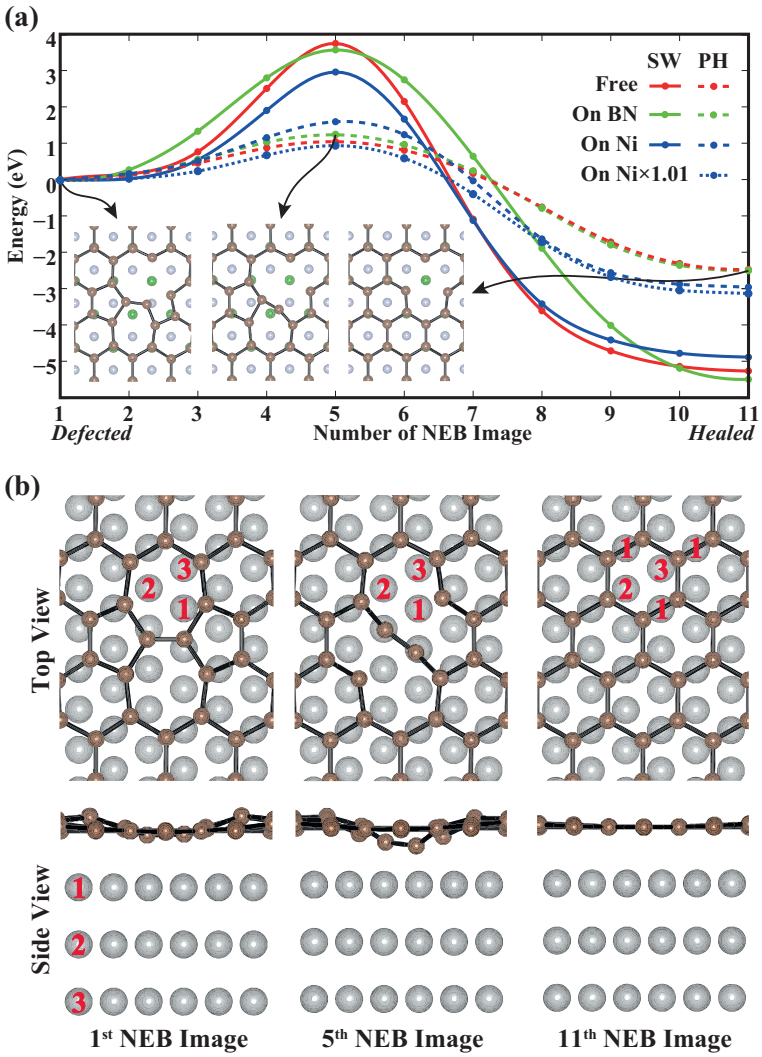

Figure 3.4: (a) Energetics of the healing path of SW and PH defects in graphene for three cases; namely without template, graphene on BN and graphene on Ni(111) substrates. The solid red, green and blue lines show the healing path of SW defect and associated energy barriers for graphene without template, graphene on BN and graphene on Ni(111) surfaces, respectively. (b) Top and side views of SW defect healing on Ni substrate. The Ni atoms forming the top, middle and bottom atomic layers of the substrate are indicated by numerals 1, 2, and 3, respectively. The lateral positions of atoms in these layers are indicated by sites 1, 2, and 3. The interaction between graphene and Ni(111) is manifested in the side view of the fifth NEB image, where carbon atoms forming the C-C bond between two heptagon are pulled down when they are passing over site-2 and site-3 of the Ni substrate.

at the growth edges where there are vacancies nearby. Therefore, the formation and healing of these defects take place on growing edges rather than at regions where graphene has already grown to its normal structure. Hence, this explains the defect free structure of graphene once it grows successfully.

Here, we calculate the energy barrier confronted during the healing process using the climbing image NEB method.[33] Structures involved in this calculations are composed of armchair graphene nanoribbons with fixed edges and defects in the middle. The height between graphene nanoribbon edges and substrate underneath is set to the optimized value found in the case of infinite graphene sheet on infinite substrate. Also the relative position is derived in similar way. The optimum configuration of graphene on BN substrate is achieved when carbon atoms of one graphene sublattice are placed on top of boron atoms of the underlying BN layer. In case of the Ni(111) substrate, graphene structure is oriented in such a way that nickel atoms at the top layer of the substrate are under the center of the bridge bonds of graphene. We first calculate the ground state configuration of completely defected and healed states. As an initial guess of a healing path, we choose a straight line connecting these defected and healed states via linear interpolation. We choose 11 NEB images where first (defected) and eleventh (healed) are not changed while other nine images are varied until the optimum healing path is found. The fifth image was chosen as the climbing image which converges to the saddle point. Results of these calculations are outlined in Fig. 3.4.

In Fig. 3.4(a), the calculated healing paths of SW defect in graphene and associated barriers are shown for three cases; namely for graphene without substrate, graphene on BN and on Ni(111) surfaces. Here the energy barriers along the healing paths of SW defects are found to be 3.74 eV, 3.57 eV and 2.96 eV for free-standing, BN and Ni substrate cases, respectively. The energy barrier is significantly lowered by the substrates. The effects of substrates are proportional to their interaction energy with graphene structure. In this respect, the binding energies of graphene on BN and Ni substrates are found to be 0.13 eV and 0.41 eV per two C atoms, respectively. How the substrate can lower the barrier energy is explained by the top and side views of atomic configuration of SW defected graphene on Ni(111) substrate in Fig. 3.4(b). Three layers of Ni(111) forming an A,B, and C stacking of the fcc structure are indicated by numerals 1, 2 and 3 starting from the top layer in the side view in Fig. 3.4 (b). Lateral positions of the atoms of these layers are indicated by sites 1, 2, and 3 in top view in

the same figure. Site-2 and site-3 are energetically favorable sites for graphene atoms above Ni(111), since the binding energies of a single carbon atom on site-2 and site-3 is more favorable compared to that of site-1 by 2.48 eV and 2.46 eV, respectively. Here during the healing process of SW defect the energy barrier is lowered because of two reasons. The first reason is that, the C atoms which form the defect are pulled by site-2 and site-3 of the Ni substrate as shown in side view in Fig. 3.4(b). This pulling is in the same direction with healing path. The second reason is that, by pulling the carbon atoms out of plane, Ni substrate increases the distance between these atoms and thereby decreases stress in the carbon-carbon bonds during the healing.

The healing paths and energy barriers of PH defect in graphene are also shown by the dotted curves in Fig. 3.4(a). The inset shows the atomic configuration of PH defected graphene on layered BN substrate. Unlike SW defect, here PH defect has one carbon atom with a sp^2-type dangling bond. The energy to be gained from the saturation of this dangling bond by forming a bond with a nearest C atom of the heptagon ring becomes the driving force for the healing. As a result, the energy barrier to heal the PH defect is lowered dramatically by ~ 2 eV as shown in Fig. 3.4(a). Our argument is justified by the fact that the barrier lowering occurs also for the healing of PH defect in free standing graphene. However, contrary to the effect of substrate in the healing of SW defect above, the barrier lowering effect of Ni(111) substrate is weaker than that of BN substrate. This is due to the interaction between the substrate and sp^2-type dangling bond; namely the stronger the interaction with substrate, the lower is the gain of energy upon saturation of the sp^2-type dangling bond of a two-fold coordinated carbon atom. As a result, highest barrier lowering takes place in the healing of PH defect in free standing graphene.

3.4 Summary

Here we showed that there are two main events happening during epitaxial graphene formation. The first one is the formation of large carbon rings at the edges of the growing structure. With the inclusion of new carbon atoms, these large rings further expand and eventually collapse into smaller structures when

some critical ring size is reached. The smaller structures formed after the collapse are composed of hexagonal and defected regions of graphene. The defected regions, which can form both before and after the collapse of rings, generally consist of pentagons and heptagons. The second major mechanism of the growth process is the healing of these defected regions formed at the edges of the growing structure. In this respect, we investigated the healing process of defects composed of neighboring pentagons and heptagons which are named as pentagon-heptagon defects. PH defect is similar to the well-known SW defect, but here some carbon atoms are two-fold coordinated with unsaturated sp^2-type bonds. The energy barrier for the healing of a PH defect is lower as compared to that of SW defect due to this deficiency. We also presented the analysis for the energetics of healing of SW and PH defects in free standing graphene, as well as graphene grown on BN and Ni(111) substrates using the climbing image nudged elastic band (NEB) method.[33] We found that the healing of PH defects is further facilitated when the lattice of graphene grown on Ni(111) substrate is expanded.

Chapter 4

Graphene / Boron Nitride Nanocapacitors

The vertical stacking of graphene / boron nitride layers examined in the previous chapter and the experimental evidences of such layered materials discussed in the introduction chapter suggests the modelling of a material where an insulator is stacked between two metallic plates. In this chapter, we consider a nanoscale capacitor model envisaged from these vertically stacked composite materials and study its capacitive behavior using *ab initio* calculations within the density functional theory with external potentials. We compare the capacitance values obtained from the present first-principles total energy calculations with those estimated within the classical Helmholtz model and reveal crucial quantum size effects at nanoscale. The nanoscale capacitor model that is composed of hexagonal h-BN layers, which are stacked between two metallic graphene sheets as described in Fig. 4.1 (a) and attains high gravimetric capacitance values which is characteristic of a supercapacitor. Series, parallel, mixed and 3D combinations of these structures can also be fabricated by repeated stacking of varying numbers of graphene and h-BN layers. Thus, by varying the separation distance in our capacitor model, we observe interesting quantum size effects at small separations which recede as the distance between the graphene plates increases.

4.1 Overview of Nanocapacitors

Developments in nanoscale physics have widened our perception of energy storage mechanisms in materials. In this respect, recyclable and efficient energy storage through light weight nanoscale capacitors have attracted interest. Recently, supercapacitors[34] have developed as one of the most promising energy storage mediums, whereby several orders of magnitude higher energy densities than those of the conventional dielectric capacitors have been realized[35]. Energy storage in supercapacitors occurs through charge separated between metal surfaces and the electric field generated thereof. So far several different materials such as mixed metal oxides,[36] polymers,[37] and carbon nanotubes[38, 39] have been used to fabricate supercapacitors. Recently, graphene with its 2D one-atom thick honeycomb structure showing a perfect electron-hole symmetry and its high chemical stability[3] has also been proposed as an ideal material for supercapacitors[40, 41, 42]. In previous studies, capacitance per unit area values of 80 μF/cm^2 and 394 μF/cm^2 have been achieved for ultrathin supercapacitors with electrodes comprised of pristine graphene and multilayer reduced graphene oxide[43]. Also, a maximum capacitance value of 205 F/gram was obtained using graphene materials prepared from graphene oxide sheets[44]. Ultra thin transparent graphene films prepared using a vacuum filtration method were also used in supercapacitor experiments[45] and a capacitance of 135 F/gram was obtained for a film of 25 nm thickness. In these experimental studies the supercapacitor models are derived from the concepts of classical capacitors, whereby the capacitance values are measured depending on the applied voltage.

Recently, nanoscale dielectric capacitors (NDC) have rapidly developed and achieved properties, which are superior to other systems of energy storage. An ideal NDC should be composed of metallic layers that can store and release charge and a dielectric material in between these layers for increasing the capacitance value without increasing the dimensions of the structure. Recent theoretical and experimental studies on graphene, carbon nanotubes and metallic nanowires have focused on understanding the dielectric properties of these structures and forming thin layers that can serve as ideal charge holding metallic plates[46, 47, 48, 49]. A theoretical method has been developed for calculating the dielectric response of periodic metal-insulator heterostructures and hence the microscopic properties of

thin-film capacitors modeled by Ag/MgO/Ag films[46]. In a recent study, nanostructured electrodes were used to fabricate transparent capacitors with polymer dielectrics and carbon nanotube electrodes[47] which are important in a range of applications from sensors to transparent circuits. Similarly structural, optical and electrical properties of transparent carbon nanotube based capacitors on glass substrates were also examined and shown to be highly efficient in photovoltaic and solar energy storage devices[48]. It was also experimentally demonstrated that Ag nanowires deposited on glass substrates can be used as electrodes[49] which can possibly be used in nanocapacitor fabrication.

Improving the permittivity of the dielectrics used have been also important for higher capacitance values of NDCs. With this regard, recent progress was made in increasing the permittivity and breakdown strength of nanocomposite materials by using fillers[50, 51] and high aspect ratio nanowires[52]. It was demonstrated that polyvinylidene fluoride and Ba-Ti-O nanowires can both increase the breakdown strength of nanocomposite dielectrics and increase their energy densities.[50] The dependence of the energy density on the volume fraction was also investigated and maximum energy density values were achieved at 50% nanoparticle volume fraction[51]. Furthermore, the existence of dielectric dead layer at nanoscales were investigated on $SrRuO_3/SrTiO_3$ dielectric capacitors and the reason behind the reduction in the capacitance values in experiments as compared to theoretical predictions were explained[46].

4.2 Calculation of Nanocapacitance with DFT

Since the principle objective of using a capacitor is to store energy by storing equal magnitude of electric charges of opposite sign in two disconnected conducting plates, a charged capacitor is in a static and non-equilibrium state. The energy stored this way is released when the plates are connected to a circuit, so that the discharged capacitor turns into an equilibrium state. At nanoscales, since the separation thickness of the devices can be as small as a nanometer, the stored energy has to be calculated from the first-principles. However, the available first-principles methods allow us to treat the distribution of only one kind of excess charge (positive or negative) in the same system at a time[53, 54, 55, 56]. Therefore, the main obstacle in studying nanocapacitors using DFT is separating

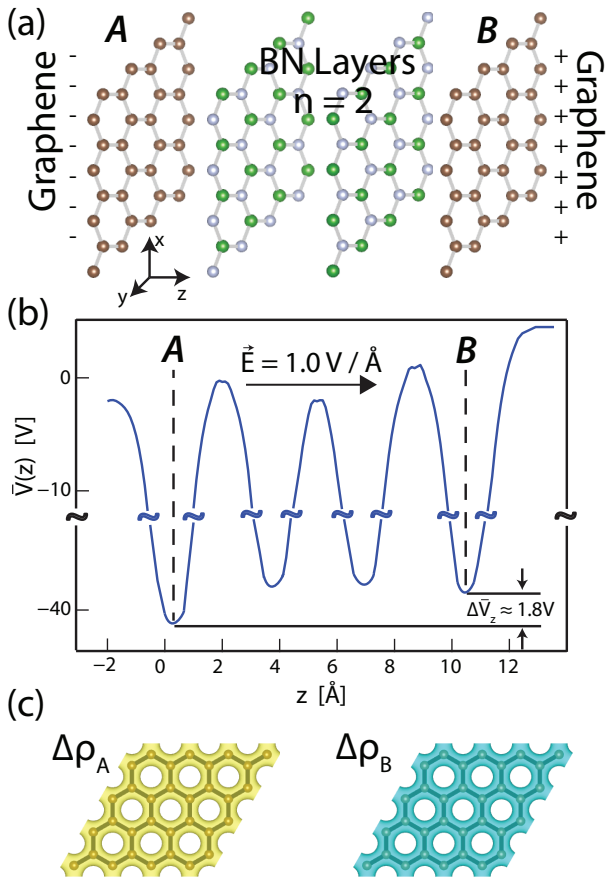

Figure 4.1: (a) A supercapacitor model with $n = 2$ h-BN layers serving as dielectrics are capped by two parallel graphene layers serving as metallic plates. The whole system is subjected to a uniform electric field along the z-axis so that graphene plates are charged by surface charge densities of $-\sigma$ and $+\sigma$, respectively. (b) Schematic description of the calculated (x, y)-plane averaged electronic potential, $\bar{V}(z)$. The difference of the potential energy between graphene layers A and B is $e\bar{V}_z$. (c) Isosurfaces of the self-consistent difference charge densities of the negatively charged (A) and positively charged (B) graphene layers are ρ_A and ρ_B, respectively. The isosurface values are taken as 0.01 electrons / Å^2. Yellow and blue isosurfaces indicate excess and depleted electrons, respectively. The computations are performed on a 2×2 supercell with a vacuum spacing of 20 Å.

positive and negative charges on the plates of a capacitor. In our model, the charge separation is achieved by applying an external electric field $\vec{E}$, perpendicular to the graphene layers, as schematically shown in Fig. 4.1 (a). This situation mimics the operation of a capacitor, whereby the surface charge of opposite sign initially stored on different metallic plates create a perpendicular electric field. The shorting of these two plates and hence the discharge of the capacitor are hindered by placing sufficient amount of vacuum space or dielectric h-BN layers between graphene plates.

On the other side, charge separation through applied electric field by itself brings along a serious problem as discussed in the method chapter. This artifact of PW methods can be circumvented by using a local basis set such as atomic orbitals (AO), since they fail to represent the states which can be bound to the quantum well in the middle of the vacuum spacing. In a recent paper[57] the treatment of charged systems has been extensively analyzed. Thus, we carried out first-principles spin-polarized and spin-unpolarized calculations within density functional theory(DFT) using atomic orbitals(AO) as local basis set. The exchange-correlation potential is approximated by the generalized gradient approximation (GGA) using Perdew, Burke and Ernzerhof(PBE) functional[58]. The eigenstates of the Kohn-Sham Hamiltonian are expressed as linear combinations of numerical atomic orbitals. A 200 Ryd mesh cut-off is chosen and the self-consistent field (SCF) calculations are performed with a mixing rate of 0.1. Core electrons are replaced by norm-conserving, nonlocal Troullier-Martins pseudopotentials[59]. The convergence criterion for the density matrix is taken as 10^{-4}. Atomic positions, lattice constants are optimized by using the conjugate gradient method, where the total energy and atomic forces are minimized. In particular, the minimum energy stacking sequence of the composite material consisting of n BN layers between two graphene is determined for each n. All numerical calculations are performed using the SIESTA code[21]. Dipole corrections[60] are applied in order to remove spurious dipole interactions between periodic images for the neutral calculations. Calculations are carried out on the (2×2) supercells in order to account possible reconstructions, but the relevant values are given per primitive cell.

Previous analysis[61] have shown that the interlayer spacing of graphite has been overestimated by GGA approximation using PW91 functional, but has improved to the 4% of the experimental value with the van der Waals (vdW)

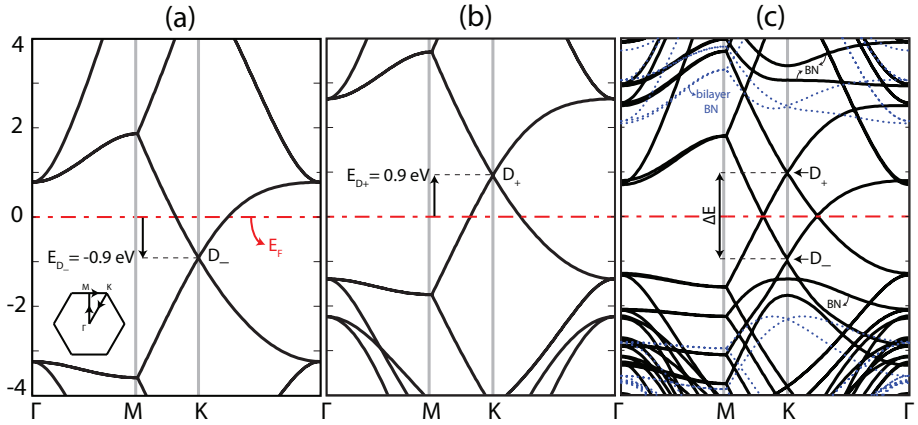

Figure 4.2: Electronic energy band structures calculated for (2×2) supercell. The zero of energy is set to the Fermi level E_F shown by the red dash-dotted lines. (a) Isolated, single layer graphene, which is negatively charged by $Q = -0.06e$ per primitive unitcell (or $\sigma = -0.18C/m^2$). (b) Positively charged single layer graphene with $Q = +0.06e$ per primitive unitcell (or $\sigma = +0.18C/m^2$). $E_{D_\pm} \simeq \pm$ 0.9 eV are the down and up shifts of the Dirac points (D_- and D_+) relative to the Fermi level for negative and positive charging, respectively. (c) The electronic band structure of the capacitor consisting of two h-BN layers capped by single layer graphenes, which is subjected to an electric field of $\vec{E} = 1.0$ V/Å. The band structure of the free h-BN bilayer is shown by the blue dotted lines. The energy difference between D_- and D_+ points is ΔE. The tunneling barrier is indicated by $\Delta\Phi$. The inset shows the 2D Brillouin zone with symmetry directions.

correction.[22] To reveal how well the spacing between graphene and single layer h-BN and the spacing between the graphene layers capping two h-BN layers in Fig. 4.1 (a), both optimized by PBE are predicted, we compared the same spacings with those calculated with PBE including vdW correction using VASP code.[19] While the spacing between graphene and h-BN is overestimated by 5.5% by PBE relative to that obtained by including vdW correction, the overestimation of the spacing in our capacitor model reduces to 1.5%. As for the lattice parameter of the hexagonal primitive unit cell predicted by PBE and PBE+vdW, the former method overestimates only 0.8%. In view of the fact that h-BN layers serve as dielectrics, the overestimation of the interlayer spacings by approximately 5.5% is acceptable.

Regarding the structure, free h-BN and free graphene have lattice constants calculated to be a= 2.53 and a=2.48,respectively, which lead to a lattice mismatch of ∼2%/. When grow on top of graphene, this lattice mismatch is accomodated by a supercell of 50x50 comprising 10.000 atoms. Therefore, the investigation of superlattice effects and miniband formation may not be investigated easily from first-principles calculations. However, the effects of small lattice mismatch is expected to be minute to affect the properties of dielectric h-BN spacer. Additionally, when optimized together in the single cell, h-BN having relatively smaller in-plane stiffness is compressed to the smaller unit cell.

4.3 Results and discussion

We first consider two isolated graphene layers each one is charged by $\pm Q$ = 0.06 electrons per primitive unitcell (or $\pm\sigma = 0.18C/m^2$). The electronic band structure of each graphene is shown in Fig. 4.2 (a)-(b): The Dirac point D_- dip below the Fermi level, when a single, isolated graphene is negatively charged by $\sigma = -0.18C/m^2$. In contrast, the Dirac point D_+ rises above the Fermi level when the single, isolated graphene layer is positively charged or hole doped by $\sigma = 0.18C/m^2$. The upward and downward shifts of the corresponding band structures in Fig. 4.2 (a)-(b) are equal and $|E_{D_-}| = E_{D_+} \simeq 0.9$ eV.

Next we examine our model of nanocapacitor described in Fig. 4.1 (a), which is actually one single system of a composite material consisting of two insulating

h-BN layers placed between two parallel semimetallic graphene layers. Initially, it has zero net charge in graphene layers. However, when exerted by a positive $\vec{E}$ along z-axis, self-consistent field calculations accommodate excess electrons on the left graphene while the same amount of electrons are depleted from the right graphene. Hence, the integral of the volume charge in the cell of the capacitor is still zero, $\int_{cell} QdV = 0$. The atomic structure, interlayer spacings, relative positions of the layers and the cell parameters, are optimized. The plane-averaged electronic potential, $\bar{V}(z)$, is shown in Fig. 4.1 (b) under an external electric field of $\vec{E} = 1.0$ V/Å. For this case, the potential energy difference between the two graphene layers is calculated to be $e\Delta\bar{V}_z \simeq 1.8$ eV, which leads to the accumulation of equal amount of surface charge of opposite sign, $\pm Q = 0.06$ electrons per primitive unitcell (or $\pm\sigma = 0.18 C/m^2$) on either graphene layers. The isosurface plots of the difference charge density of the negatively charged (A) and positively charged (B) graphene layers, namely the difference of charge densities between the charged and neutral graphene layers, $\delta\rho_{A,B} = \rho_{A,B} - \rho_0$ illustrate the charge separation.

The band structure of this optimized capacitor is presented in Fig. 4.2 (c) which, apart from minute changes, is practically combination of bands in Fig. 4.2 (a) and (b) and those of h-BN bilayer shown by dotted lines in Fig. 4.2 (c). We infer following features from Fig. 4.2, which are essential for the model: (i) The band gap of the free h-BN bilayer is conserved in the capacitor, except that they split due to the electric field. Accordingly, the potential barrier for electron to tunnel from left to right graphene is $\Delta\Phi$ =3eV as shown in Fig. 4.2 (c). In reality, the potential barrier can be higher than 3 eV, since DFT underestimates the band gap. As a matter of fact the band gap of h-BN calculted to be ∼4.6 eV[62], rises up to 6.8 eV after GW self-energy correction.[63]. On the other hand, the band gap of single layer MoS_2 has been overestimated through GW correction.[64] Experimentally, it is measured to be $\sim$ 5.5 eV.[7] We note that the band gap is an excite state property of the model capacitor and wide band gap hinders the tunnelling of carriers from one plate to other through the h-BN spacer. Nevertheless, the SCF electronic potential and the potential difference between plates are ground state propertied, which are properly predicted in our calculations. (ii) The integrals of the SCF charge on the graphene layers A and B in Fig. 4.2 (c) are equal to the excess charge values used in the calculation of Fig. 4.2 (a) and (b), namely $\int^{B,A} \sigma(x,y)dxdy = \pm Q = 0.06$ electrons per primitive cell (or $\pm\sigma = 0.18\ C/m^2$). (iii) The calculated energies of the Dirac points for

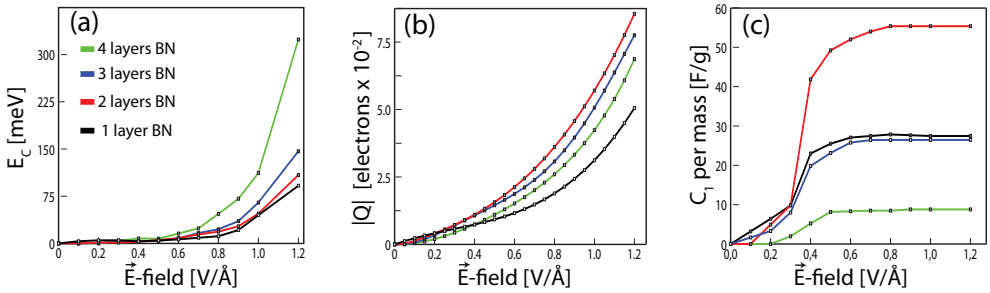

Figure 4.3: Variations of stored energy E_C, charge $|Q|$ and capacitance C as a function of external electric field $\vec{E}$ calculated for different n number of h-BN layers between two graphenes. Note that the capacitance values start to saturate after $\vec{E}$ >0.35 V/Å and reach their steady state values for $\vec{E} > 0.6$ V/Å.

the left graphene layer, (E_{D_-}) in Fig. 4.2 (a) and the right graphene layer, E_{D_+} in Fig. 4.2 (b) relative to the common Fermi level E_F are equal in magnitude because of the electron-hole symmetry near the Dirac points, i.e. $|E_{D_-}| = E_{D_+}$. In the electronic band structure of the capacitor in Fig. 4.2 (c), the energy difference between the Dirac points D_+ and D_- is ΔE. Interestingly, ΔE is equal the sum of the energy shifts in Fig. 4.2 (a) and (b), i.e. $\Delta E = |E_{D_-}| + E_{D_+}$. (iv) Even more interesting is that $\Delta E \simeq e\Delta\bar{V}_z$ in Fig. 4.1 (b). These features by themselves demonstrate that our model of capacitor is, in fact, appropriate and precise. Even if adjacent layers are coupled, the graphene layers A and B are isolated and electronically decoupled. It should be noted that the capacitive behavior attained above by applying perpendicular electric field is equivalent to the reversed situation, where $\pm Q$ charge is stored in different plates can induce the same $\vec{E}$.

Having tested our model of capacitor, we next investigate its capacitive behavior. To this end we calculate the stored energy as a function of the applied electric field for different numbers n of parallel h-BN . The energy difference between the total energies of the structures under external field and under zero field gives us the energy stored in the capacitor, $E_C(n, \vec{E}) = E_T(n, \vec{E}) - E_T(n, \vec{E} = 0)$. The total energies, E_T, are obtained by SCF energy calculations of optimized structures. In Fig. 4.3 (a) the variations of capacitor energy with applied $\vec{E}$ are plotted for n =1-4. The variation of E_C is not monotonic with n for the reason explained in the forthcoming part. In Fig. 4.3 (b), we present the variation of the

Table 4.1: Number of BN layers between the graphene plates, n; calculated and optimized values of the distance between graphene layers capping h-BN layers, d (in Å); total mass of the primitive unitcell, m (in $kg \times 10^{-22}$); calculated dielectric constants of the layered h-BN sheets, κ; magnitude of the excess charge on the graphene plates, $|Q|$ (in electrons); energy stored in the primitive unitcell, E_C (in eV); local potential difference between the graphene plates, $\Delta\bar{V}_z$ (in V); gravimetric capacitance in Farads per grams calculated using (i) the E_C and Q values obtained from DFT calculations, *i.e.* $C_1 = Q^2/2mE$; (ii) the $\Delta\bar{V}_z$ and Q values obtained from DFT calculations, *i.e.* $C_2 = Q/m\Delta\bar{V}_z$ and (iii) using the classical Helmoltz expression, *i.e.* $C_3 = \kappa\epsilon_0\frac{A}{md}$, where κ is the dielectric constant value for bulk BN, $\epsilon_0 = 8.85 \times 10^{-12}\ F/m$ is the permittivity of free space and $A = 5.25 \times 10^{-20}\ m^2$ is the area of the graphene plate in the primitive unitcell. The masses of the capacitor models are calculated by adding the atomic masses of B, C and N atoms in the primitive unitcell of the optimized composite systems.

n	d	m	κ	$\|Q\|$	E_C	$\bar{V}_z$	C_1	C_2	C_3
1	6.21	1.21	1.59	0.033	0.033	2.2	19.8	18.7	33.9
2	9.52	1.63	2.17	0.060	0.035	1.8	54.4	32.7	16.5
3	12.23	2.04	2.75	0.055	0.070	3.5	16.9	12.3	10.2
4	15.14	2.46	3.19	0.040	0.093	4.6	5.7	5.7	6.9

magnitude of the excess charge, $|Q|$ stored in either graphene layers as a function of the applied field for n =1-4. Here $|Q|$ is also obtained from first-principles calculations by integrating the net charge in either graphene layer. In Fig. 4.3 (c) we calculate the capacitance per mass C_1 from the expression $C_1 = Q^2/(2mE_C)$, where m is the total mass of B, N and C atoms in the model. We note that for $\vec{E}$ >0.35 V/Å, the calculated values of capacitance C_1 begin to saturate to different values depending on n and become independent of the applied field as one expects. Thus, our choice of $\vec{E}$ =1V/Å in Fig. 4.2 was reasonable, since it is within the saturated region for n =2. This very important result shows that even if the energy of the nanoscale capacitor is obtained from the first-principles calculations, the behavior of the calculated capacitance complies with its definition. The transient behavior of $\vec{E}$ in the range of 0< $\vec{E}$ <0.45 is due to the uncertainty in the calculation of optimized E_T. The gravimetric capacitance of n =2 is calculated to be C_1 = 54.4 F/gr, which is considered to be in the range of supercapacitors. The capacitance values can also be acquired from the definition, namely $C_2 = Q/m\Delta\bar{V}_z$ using the calculated charge values $|Q|$ in Fig. 4.3 (b) and $\Delta\bar{V}_z$ from the plane-averaged potential $\bar{V}(z)$ as described in Fig. 4.1. The capacitance values acquired this way are in the range of those calculated from $C_1 = Q^2/(2mE_T)$ in Fig. 4.3 (c). Nonetheless, in the rest of discussions we used the capacitance values C_1 obtained from the quantum mechanical calculations of energy and charge, since due to the plane averaging process of electronic potential, $\Delta\bar{V}_z$ does not provide the necessary precision compatible with that of the total energy calculations. In Table I, we list various parameters and calculated values relevant for the calculations of gravimetric capacitances per unit mass. We do not consider the graphene bilayer corresponding to $n = 0$, since the charge stored in the layers are shorted.

In Fig. 4.4 we compare capacitance values calculated using DFT and classical Helmholtz model as a function n. The capacitance value acquired from the DFT results is small for single h-BN layer; but passes through a maximum and then decreases with increasing numbers of h-BN layers. The latter behavior for large number of h-BN layers is reminiscent of that of classical capacitance, namely $C \propto 1/d$, since the distance d between the charged capacitor plates also increases as n increases. However, that the increase in the value of C_1 as n increases from 1 to 2 is surprising, since the effect of the insulating medium consisting of h-BN layers is indigenous to the DFT calculation of C_1 deduced from E_C. This situation is attributed to a quantum size effect as revealed from our analysis of

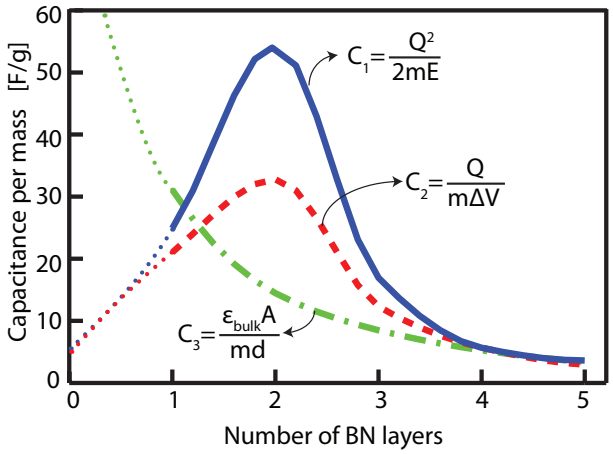

Figure 4.4: Comparison of the calculated capacitance values at $\vec{E}$ = 1.0 V/Å as a function of the number of insulating h-BN layers, n. Capacitance values calculated using the optimized total energy $E_T[n, \vec{E}]$ obtained from DFT, C_1; using the plane-averaged $\Delta\bar{V}_z$, C_2; and the purely classical Helmholtz formula, C_3; are shown by solid(blue), dashed(red) and dash-dotted(green) lines, respectively. The dotted lines show the hypothetical capacitance values for $n < 1$.

high frequency dielectric constant, $\kappa_{\nu=\infty}$, as well as low frequency (static) dielectric constant $\kappa_{\nu=0}$, of h-BN sheets calculated as a function of n. Because of the layered character, one distinguishes the in-plane ($\|$) and perpendicular ($\perp$) dielectric constants in BN spacer. The calculated $\kappa_{\nu=0,\|}$ and $\kappa_{\nu=0,\perp}$ of the layered bulk BN crystal are 5.25 and 3.80, respectively, which are in fair agreement with experiment.[65] Calculated values of $\kappa_{\nu=0,\|}$ ($\kappa_{\nu=0,\perp}$) are listed in Table I for n =1-4. Accordingly, κ increases with increasing n and hence displays a strong size effect. Rather small values of κ for n =1 and 2 cause that C_1 first increases with increasing h-BN layer for $n \leq$2, but it decreases with increasing n for $n >$2 as shown in Fig. 4.4. In other words, although a decrease in the capacitance value is expected as the layer-layer separation increases, the increase in the dielectric constant of h-BN layers counters this effect. Hence, as a result of the competition between the increased layer-layer distance and increasing dielectric constant values, the capacitance value passes from a maximum at an optimum spacing after which it starts to decrease again. In the same figure we also plotted the variation of capacitance obtained from the Helmholtz model $C_3 = \kappa\epsilon_0 A/md$, where d is the distance between graphene layers corresponding to a given n, and κ is the dielectric constant of bulk BN. This is a purely classical value. We see that

quantum effects dominate the capacitance for $n < 4$, while they decay quickly and the capacitor behaves as a classical capacitor for $n \geq 4$.

4.4 Summary

We investigated a nanoscale dielectric capacitor model consisting of two-dimensional, hexagonal h-BN layers placed between two commensurate and metallic graphene layers. The separation of equal amounts of electric charge of different sign in different graphene layers was achieved by applying electric field perpendicular to the layers. The stored charge, energy, and the electric potential difference generated between the metallic layers were calculated for the relaxed structures. Predicted high-capacitance values exhibit the characteristics of supercapacitors. The capacitive behavior of the present nanoscale model is compared with that of the classical Helmholtz model, which reveals crucial quantum size effects at small separations, which in turn recede as the separation between metallic planes increases.

Chapter 5

Laterally Repeating Graphene / Boron Nitride Composite Materials

In the previous two chapters, we investigated vertical growth of graphene / boron nitride layers using first principles and proposed a nanocapacitor model as an immediate application of this stacking. However, graphene / boron nitride composites are not limited to vertical stackings of these two, but also laterally repeating composites of these two materials can be realized. In fact, realization of two dimensional (2D) systems and their composites three decades ago, where electrons are propagating in 2D, but confined in the third dimension (3D) showed quantization that is different from 3D systems.

In this chapter, we consider one-atom-thick composite materials which are composed of laterally and periodically repeating, zigzag or armchair nanoribbons that are merged commensurately as stripes in a single layer honeycomb structure. The model is described in Fig. Fig. 5.1(a-b). While the model has translational periodicity of the honeycomb structure along the x-direction, the translational periodicity along y-direction depends on the widths of adjacent graphene and h-BN stripes in terms of the number of C and B+N atoms in the unit cell; p and q, respectively. We name these hybrid structures as graphene/BN composites

abbreviated as G(p)/BN(q). We distinguish diverse types of features and functionalities in different types of G(p)/BN(q) composites having zigzag or armchair geometry. As schematically described in Fig. 5.1(c), these are BN δ-doping in wide graphene stripes; electronically decoupled 1D composites in a 2D framework consisting of wide graphene and wide h-BN stripes; graphene δ-doping in wide h-BN stripe; and finally line compounds where each unit cell contains one graphene and one BN hexagon.

5.1 Overview

The formation of 2D patterned domains of one type of material embedded in another material has been previously proposed.[66, 67] Not only domains but also periodically repeating defects and adatom islands can be considered to construct mesh structures. Recent advances have made the mesh configuration a controllable parameter for monitoring physical properties of nanostructures.[68, 69, 70] Specifically, in-plane graphene/h-BN hybrid structures have attracted considerable interest because of their potential applications in flexible 2D opto-electronic devices.[71, 72, 73, 74, 75, 76] The realization of monolayer materials consisting of hybrid graphene/h-BN domains has motivated further research in the field.[12] Subsequently, graphene/h-BN in-plane heterostructures with controllable widths down to 100 nm have been fabricated using lithographic patterning and sequential CVD growth of graphene[77]. Anomalous insulator-metal transition has been observed in graphene/h-BN hybrid structures, such as BN nanoribbons or nano domains embedded in graphene[78]. Theoretically, half-metallicity has been predicted in hydrogen saturated hybrid graphene/h-BN nanoribbons.[79]

Here, we carried out a systematic analysis of electronic structure showing that the electronic and functional properties of these one-atom-thick composites can be tuned by altering the p/q ratio and boundary geometry of the constituents; they can be metal or semiconductor in the energy range of visible light. We find that: (i) when their widths are increased, the constituent stripes become electronically decoupled and in a 2D composite system a transition from 2D to 1D takes place, whereby electronic states become confined to 1D stripes. Such structures can form multiple quantum wells. (ii) However, when the widths of both stripes (p and q) are decreased, they start to couple and hence the composite

material behaves as a compound composed of lines of different materials and displays unique characteristics. The electronic structure acquires 2D dispersion; not only along the stripes, but also in the transversal direction. (iii) The properties of one constituent alone can be modified by the δ-doping of the other constituent. (iv) Remarkably, the ribbon of composite material, such as BN(q) capped by G(p) from both side allows charge separation of opposite polarity and makes energy storage possible under the external electric field along y-direction.[80] These ribbons also undergo metal insulator transition under applied electric field and can function as resonant tunneling double barrier.[81] (v) Stable, single-wall nanotubes can be constructed from G(p)/BN(q) zigzag and armchair nanoribbons. Briefly, a comprehensive analysis of dimensionality of electronic structure of a 2D monolayer, composite G(p)/BN(q) material is presented and novel features are revealed. Additionally, this study includes an extensive analysis of the energetics related with the hybrid graphene/BN structures.

5.2 Method

Our predictions are obtained from the state of the art first-principles pseudopotential calculations based on the spin-polarized Density Functional Theory within the generalized gradient approximation including van der Waals corrections.[22] We used projector-augmented wave potentials [29] and the exchange-correlation potential is approximated with Perdew-Burke-Ernzerhof functional.[58] The Brillouin zone was sampled in the Monkhorst-Pack scheme, where the convergence in energy as a function of the number of **k**-points was tested. The **k**-point sampling of (21×21×1) was found to be suitable for the BZ corresponding to the primitive unit cell of G(4)/BN(4) composite with zigzag edge. For wider stripes and hence larger unit cells this sampling has been scaled accordingly. The number of **k**-points were further increased to (48×48×1) in the projected density of states calculation. Atomic positions were optimized using the conjugate gradient method, where the total energy and atomic forces were minimized. The energy convergence value between two consecutive steps was chosen as 10^{-5} eV. A maximum force of 0.01 eV/Å was allowed on each atom. Numerical calculations were carried out using the VASP software.[19] To achieve charge separation of opposite polarity on composite nanoribbons under transversal external electric field, the

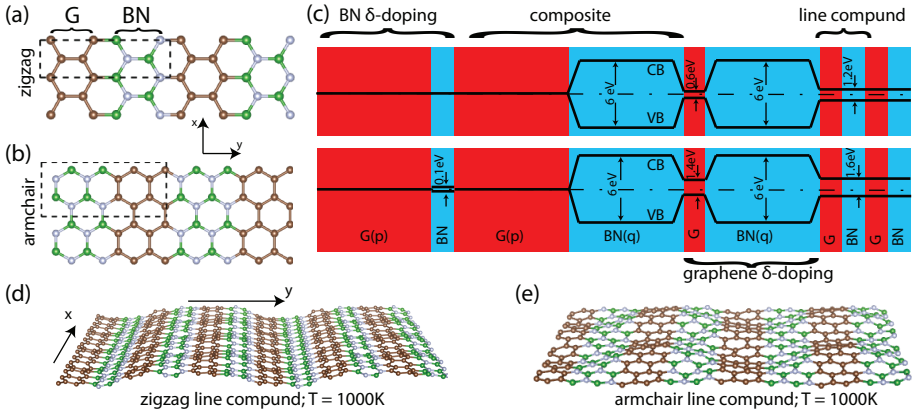

Figure 5.1: The composite materials, which consist of laterally repeating, commensurate graphene and h-BN nanoribbons merged in a single layer honeycomb structure and hence form stripes along the x-direction. (a) G(p)/BN(q) composite composed of zigzag graphene and h-BN nanoribbons, which are stripes periodically repeating along y-axis. The unit cell of the composite structure is delineated by dashed lines. Numbers of C and B+N atoms in the unit cell are p=4 and q=4, respectively. (b) Same for armchair graphene and h-BN nanoribbons with p=8 and q=8. (c) Schematic description of the band diagrams in the direct space with conduction band (CB) and valance band (VB) edges. The band gaps are shown in between. Four different combinations are schematically described: (i) BN δ-doping in graphene; (ii) A composite structure composed of 1D, wide graphene and h-BN stripes; (iii) graphene δ-doping in h-BN; (iv) the line compound. Band gaps depend on the values of p and q, as well as the geometries of the border between stripes. (d) An MD snapshot of the 4×3 supercell of zigzag line compound taken at T=1000 K after 5 picoseconds. (e) Same for 3×2 supercell of armchair line compound. In the ball and stick representations C, B, and N atoms are shown by brown, green and blue balls, respectively.

structure optimization and self-consistent field charge density calculations are performed using SIESTA software with numerical local basis set.[21] This way spurious divergences emerging from the use of plane wave basis set with periodic boundary conditions are eliminated[57, 82].

Since the band gaps are underestimated by standard DFT, we also carried out calculations using the HSE06 hybrid functional [83, 84], which is constructed by mixing 25% of the Fock exchange with 75% of the PBE exchange and 100% of the PBE correlation energy and range separation parameter is set to 0.2. The stability of composite structures are tested by ab initio molecular dynamics (MD) calculations carried out at finite temperatures. A Verlet algorithm is used to integrate Newton's equations of motion with time steps of 2 fs. Starting from 200 K we carried out MD calculations for 1 ps at temperatures 200, 400, 600, 800, and 1000 K, continuing and lasting for 5 ps in total for each system. To maintain the system in the desired constant temperature the velocities of atoms are rescaled in each time step.

5.3 Results and Discussion

Bare zigzag graphene nanoribbon ZGNR(p) and bare h-BN nanoribbon ZBNR(q) are metallic. When their edges are saturated by hydrogen atoms, the zigzag h-BN nanoribbon transforms into an insulator.[62] Also, when the same ZBNR joins graphene nanoribbons commensurately at both side, it becomes an insulator with a wide band gap. When carbon atoms at the edges of ZGNR(p) are saturated by B and N edge atoms of ZBNR(q) at alternating sides, ZGNR(p) changes into semiconductor, where the band gap diminish as p increases. On the other hand bare armchair graphene nanoribbon, AGNR(p) is a semiconductor with a band gap which generally decreases with increasing p. At the same time, the band gap shows family behavior according to $p = 3n + m$; namely the band gap is the largest for $m = 0$, and smallest for $m = 2$ and intermediate for $m = 1$ for a given integer n.[85] However, this situation is subject to change in G(p)/BN(q) composite structure with armchair borders.

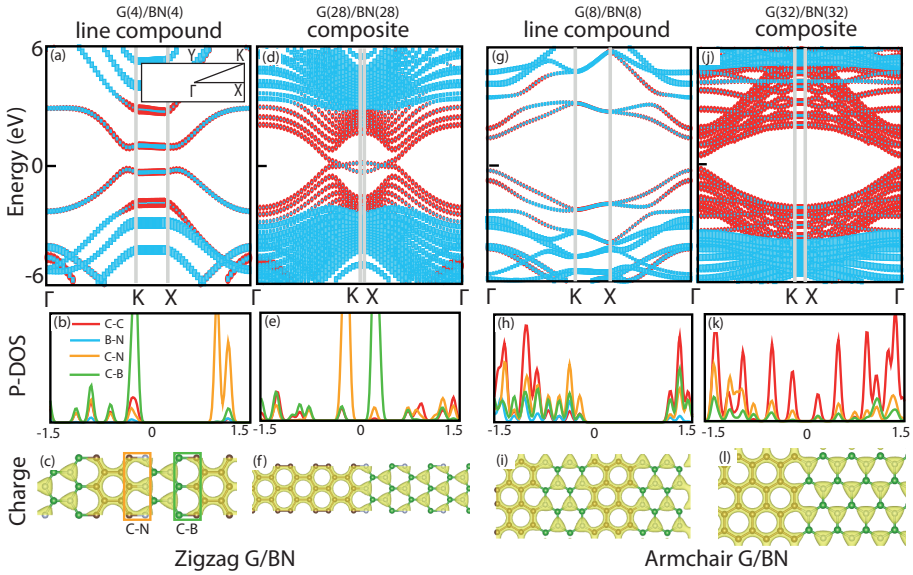

Figure 5.2: Electronic structure of various combinations of G(p)/BN(q) composite materials forming stripes along x-direction in a single layer honeycomb lattice. (a) Line compound G(4)/BN(4) with zigzag border. Contributions of graphene (red) and h-BN (turquoise) stripes to energy bands are mimicked by the size of small rectangles tracing the bands. The rectangular Brillouin zone and its relevant symmetry directions are shown by inset. (b)Projected density of states, P-DOS projected to C-N, C-B bonds at the borders of stripes, and C-C, B-N bonds within graphene and h-BN stripes. The border atoms are delineated in a rectangle. (c) Isosurfaces of the total electronic charge density, $\rho(\mathbf{r})$. (d) Energy bands of composite G(28)/BN(28) with zigzag borders. (e) P-DOS. (f) Isosurfaces of the total charge density. (g)-(i) Same for the line compound G(8)/BN(8) with armchair border. (j)-(l) Same for G(32)/BN(32) composite with armchair border.

5.3.1 Energetics and stiffness

The zigzag border of a G(p)/BN(q) comprises one type of bond only; one side C-B bond, and the other side C-N bond. In this respect, the energetics of the zigzag border between graphene and h-BN is crucial for the lateral epitaxial growth. Here we present an analysis of energetics, which may be critical for the growth of graphene/BN composite materials.

The substitution of both B and N in 5×5 graphene are endothermic and the substitution energies are calculated as -2.64 eV and -3.59 eV, respectively. Accordingly, the substitution of C atom in graphene is easier by B atom than by N atom. Next, we examine the adsorption of B and N atoms to the zigzag edges of bare graphene nanoribbons. We first consider the adsorption of isolated, single B or N to ZGNR(16). The calculated binding energy of the isolated, single B (N) atom to the carbon atom at the zigzag edge is 6.19 eV (6.86) eV. The binding energies is positive since the adsorption of B or N is an exothermic process. In compliance with the substitution energies discussed above, N atom forms relatively stronger bond. We also consider the situation where one edge of ZGNR(16) is fully covered either by B or by N atoms. Here the binding energies are given by including and also by excluding the adsorbate-adsorbate (namely B-B or N-N coupling). The binding energy of full B (N) coverage of one edge is found to be 4.79 eV (6.19 eV), if the adsorbate-adsorbate coupling is included. Conversely, the binding energy of B (N) is calculated to be 6.4 eV (6.08) eV, if the adsorbate-adsorbate coupling is excluded. Here the adsorption of N in two cases displays an opposite trend as compared to that of B atom, since its magnetic state is different when compared to isolated case.

Another critical energy to be addressed is associated with the commensurately grown, single ZGNR(p)+ZBNR(q) composite nanoribbon, which is treated within the supercell method using the prototype ZGNR(12)+ZBNR(12) ribbon. Here one distinguishes two cases: In the first one, ZBNR(12) is attached to ZGNR(12) through its B atoms located at one of the edges and thus forms C-B bonds at its border with graphene. In the second case, ZBNR(12) is attached to ZGNR(12) through its N atoms to form C-N bonds at the border. Through the difference of the total energies calculated for these two cases ($E_T[B-C]$=-210.06 eV and $E_T[C-N]$=-209.94 eV), we found that the formation of C-B bonds between two commensurately grown ZGNR(12) and ZBNR(12) nanoribbon is favored by

0.13 eV per bond relative to C-N bond. This conclusion agrees with the recent experimental data.[75] Two types of bonds, C-B and C-N coexist at either borders of armchair geometry.

The in-plane stiffness, which is commonly used to measure of strength for 2D materials can be expressed as $C = \frac{1}{A_o} \times \frac{\partial^2 E_s}{\partial \epsilon^2}$ where E_s is the strain energy, A_o is the equilibrium area and ϵ is the axial strain calculated by $\Delta a_{x,y}/a_{x,y}$, a being the lattice constant in the x or y direction. The calculated in-plane stiffness values of the composite materials approximately correspond to the average of the in-plane stiffness of pure constituents (graphene C_G=330 N/m^2, h-BN C_{BN}=255 N/m^2); namely $\bar{C} = (p \times C_G + q \times C_{BN})/(p+q)$. We also calculate $\bar{C}$=290 N/m^2 for p=4 q=4, which is rather high. In fact, it is higher than that of silicene (62 N/m^2) and MoS_2 (138 N/m^2)[63, 86]. The stability of a 2D prototype line compound of zigzag and armchair composite structure is tested by ab-initio MD calculations up to T=1000 K. Both composite structures remained stable except atomic planes became wavy as shown in Fig. 5.1 (d) and (e).

5.3.2 Line compound

In Fig. 5.2(a), line compound G(4)/BN(4) with zigzag border is a semiconductor with a band gap of 1.2 eV. The effective mass, $m^*_{x,y} = \hbar^2[d^2E_n(k_{x,y})/dk^2_{x,y}]^{-1}$, of electrons and holes is small for k_x, but large for k_y resulting in conductivity along x-direction much higher than that along y-direction; namely $\sigma_x >> \sigma_y$. As shown by the bands in Fig. 5.2(a), and by the density of states projected to C-B, C-N bonds at the border, and C-C, B-N bonds within the graphene and h-BN stripes in Fig. 5.2(b), states at the valence band originate mainly from C-B bond and C-C bonds, while the states at the edge of conduction band are constructed from C-N bonds. The gap between bands constructed from pure B-N bonds is $\sim$ 6 eV. Because of coupling between graphene and h-BN stripes, G(4)/BN(4) is a compound and is considered to be a unique material, whereby line like, narrow graphene and h-BN stripes extend along x-axis. As shown in Fig. 5.2(c) significant amount of charge is transferred from C to N and from B to C at the alternating borders of h-BN stripes. Similar behavior also occurs in armchair line compound, which is also a semiconductor with a direct band gap of $E_g = 1.7$ eV as shown in Fig. 5.2 (g)-(i). The states at the edges of the valence

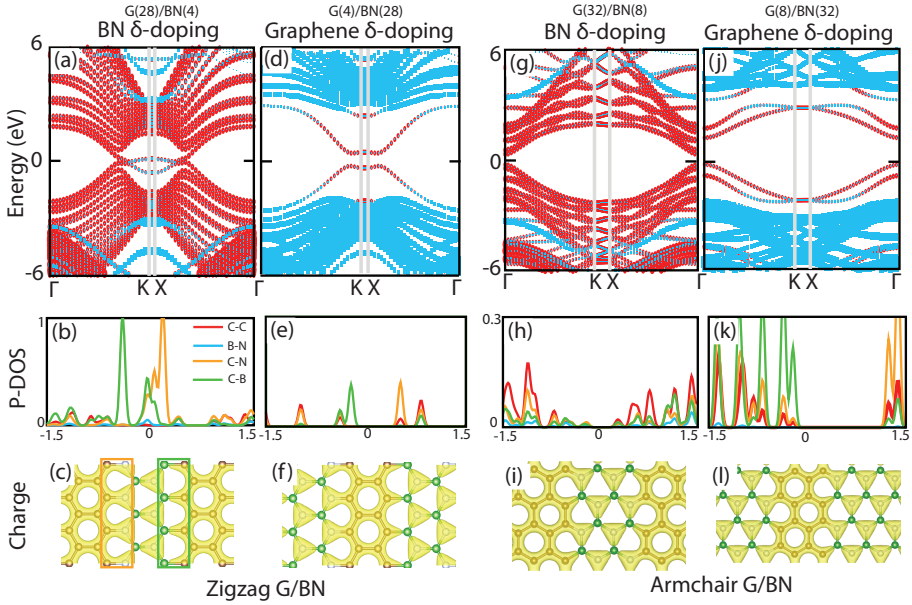

Figure 5.3: δ-doping of a wide graphene stripe by the narrow h-BN stripe with zigzag or armchair border and vice-versa. (a) Electronic band structure of the wide graphene stripe, which is δ-doped by the narrow BN stripe with zigzag border, i.e. G(28)/BN(4). (b) Density of states projected to C-B, C-N bonds at the borders highlighted by rectangles, and C-C, B-N bonds within graphene and h-BN stripes. (c) Isosurfaces of the total charge density. (d)-(f) Same for a wide BN stripe, which is δ-doped by the narrow graphene with zigzag border, i.e. G(4)/BN(28). (g)-(i) Same for a wide graphene stripe, which is δ-doped by the narrow BN stripe with armchair border, G(32)/BN(8). (j)-(l) Same for a wide BN stripe, which is δ-doped by the narrow graphene with armchair border, G(8)/BN(32).

and conduction band are constructed from C, B and N atomic orbitals. Clearly, armchair G(8)/BN(8) is a compound of graphene and h-BN with unique features.

5.3.3 Composite structures

In Fig. 5.2(d-f), zigzag G(28)/BN(28) composite displays rather different behavior; we see that graphene and h-BN states are separated in direct space. h-BN states form an insulator with a band gap of ~ 6 eV. A small gap occurs along $K - X$ and also $X - \Gamma$ direction between bands originating from the C-N and

C-B bonds. Even if these two bands appear to have very small gap of 0.04 eV at a specific **k**-point along Γ-X direction, they are physically separated in the direct space. However, if a small number of electrons could be accommodated at the minimum of the conduction band through tunneling or doping, a strictly 1D band originating from C-N bond states can be conducting along the stripes. This feature can be used as a switch operating under applied field along y-direction. A direct band gap of ∼1 eV occurs between the bands in graphene along Γ-K direction.

The situation with G(32)/BN(32) armchair composite in Fig. 5.2 (j)-(l) is different; graphene stripes behave as a 1D narrow band gap semiconductor near Γ-point, while h-BN is an insulator. Upon modulating the doping, namely donors in h-BN stripe, such a composite structure can be used to construct multichannel conductor between two electron reservoirs with quantized conductance. Alternatively, one can construct electron channels with hornlike entrances and exits at the ends of stripes, and can attain adiabatic evolution of channel states. Briefly, we believe that armchair composite structures can be utilized to realize diverse geometries yielding some fundamental quantum effects.

5.3.4 δ-doping of graphene and BN

The electronic structure of wide G(p) stripe, which is δ-doped by BN(4) is presented in Fig. 5.3(a-c) for zigzag border. h-BN bands with large band gap are separated from graphene states. h-BN stripe is too narrow and hence two bands corresponding to zigzag edge states originating from the C-N and C-B bonds cross each other along Γ-X at the Fermi level. This attributes a 1D metallic character to the graphene stripe, even if narrow BN stripe poses a thin potential barrier with its wide band gap. This situation is clearly seen by the high state density at the Fermi level as presented in Fig. 5.3(b). On the other hand, a wide stripe of h-BN(q) with zigzag border, which is δ-doped by G(4) is a narrow band gap semiconductor along y-direction with band gap of ∼0.7 eV as shown in Fig. 5.3(d-f). The gap occurs between the bands derived from C-N and C-B bonds. Since the potential barrier set by h-BN is high and wide, electron due to dopants (holes due to acceptors) confined to narrow quantum wells of the conduction (valence) bands of graphene stripe can exhibit strictly 1D character.

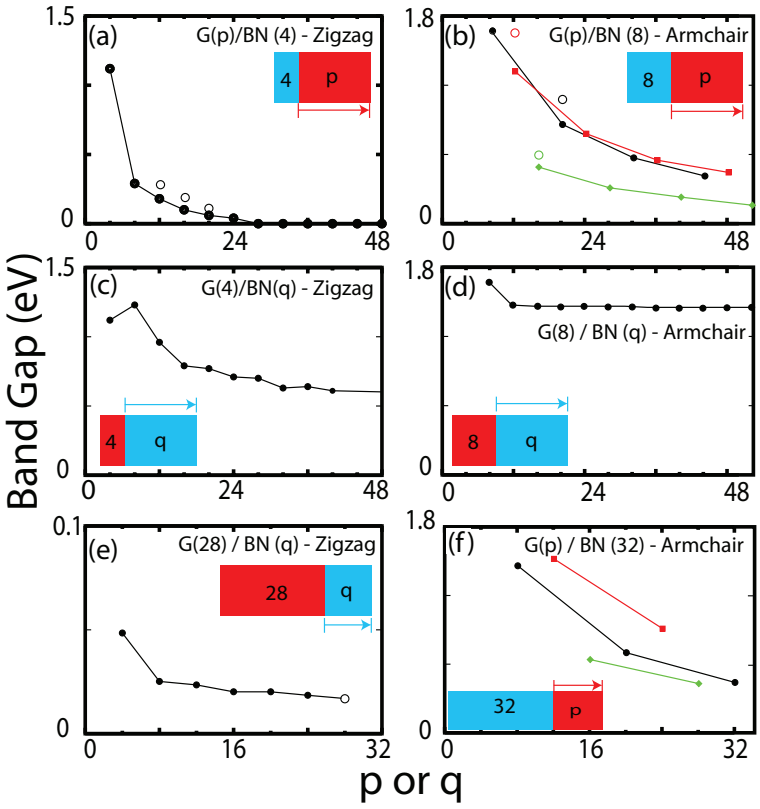

Figure 5.4: Variation of band gaps for different G(p)/BN(q) composites with zigzag or armchair borders. Band gaps calculated by HSE method are indicated by empty circles.

In Fig. 5.3(g-i), wide graphene stripe G(p), which is δ-doped by narrow BN(8) stripe with armchair edge is a narrow band gap semiconductor. The band gap is, however, large along the $K - X$ direction perpendicular to the stripes. The gap region is dominated by graphene bands, while bands associated with BN(8) occur $\sim$ 3.5 eV below and $\sim$ 3.5 eV above the Fermi level and pose a narrow but high barrier for tunneling between nearest graphene stripes. Conversely, wide BN(q), which is δ-doped by narrow G(8) with armchair border has BN bands separated by a wide band gap of $\sim$6 eV as shown in Fig. 5.3(j-l). In this band gap, the bands associated with G(8) have relatively smaller band gap at the center of the BZ and also have low density of states.

Variation of band gaps of different G(p)/BN(q) composite with zigzag or armchair border are summarized in Fig. Fig. 5.4. As shown in Fig. Fig. 5.4(a),

a wide graphene stripe, which is δ-doped by BN(4) with zigzag border, namely G(p)/BN(4) attains metallic behavior for p>24. This conclusion is confirmed also by HSE calculations. In Fig. Fig. 5.4(b), G(p)/BN(8) with armchair border remains semiconductor even for large p and has band gap E_g ranging from 1.7 eV to 0.1 eV as p increases. However, the calculated values of band gap trace always lowest value when p-4 is an integer multiple of 3 (4 being the number of C atoms at the armchair border). This is well known family behavior of graphene armchair nanoribbons, but is realized in the reverse order of the free armchair graphene nanoribbons. The band gap of the wide BN(q) stripe, which is δ-doped by G(4) stripe with zigzag border is large for small q, but decreases and eventually saturates at $\sim$0.5 eV as q increases in Fig. Fig. 5.4(c). In contrast, the band gap of BN(q) with armchair border, which is δ-doped by G(8) is not affected by the width of h-BN stripe and quickly saturates at a value E_g=1.45 eV as shown in Fig. 5.4 (d). In Fig. 5.4(e), G(p)/BN(q) composites with zigzag border, where graphene and h-BN states are physically separated and confined to their own region are always semiconductors with very small band gaps no matter what the values of p and q are. However, the band gaps of these composites with armchair border in Fig. 5.4(f) show family behavior in the energy range from 1.7 eV to 0.3 eV depending on the value of p. The largest gap values occur when p is an integer multiple of 3 and smallest values occur when p-4 is an integer multiple of 3. As noted earlier, the family behavior of band gaps, which is indigenous to armchair graphene nanoribbons occurs in reversed order in G/BN composite structure here. Band gap values of selected compounds calculated by HSE method are also shown in Fig. 5.4 by empty circles.

5.3.5 Graphene/BN composite nanoribbons

Finally, it should be noted that the properties of 2D composites outlined above can be multiplied through (hybrid) composite ribbons consisting of finite number of commensurately grown ZGNR(p) [AGNR(p)] and ZBNR(q) [ABNR(q)] nanoribbons with bare or hydrogen saturated edges. The edge geometry and ordering of nanoribbons, the edge saturation by foreign and host atoms, their size p and q, offer so many parameters to monitor their electronic and magnetic properties. These composite nanoribbons or in-plane heterostructures have been fabricated and their potential as field effect transistor and split closed loop resonator

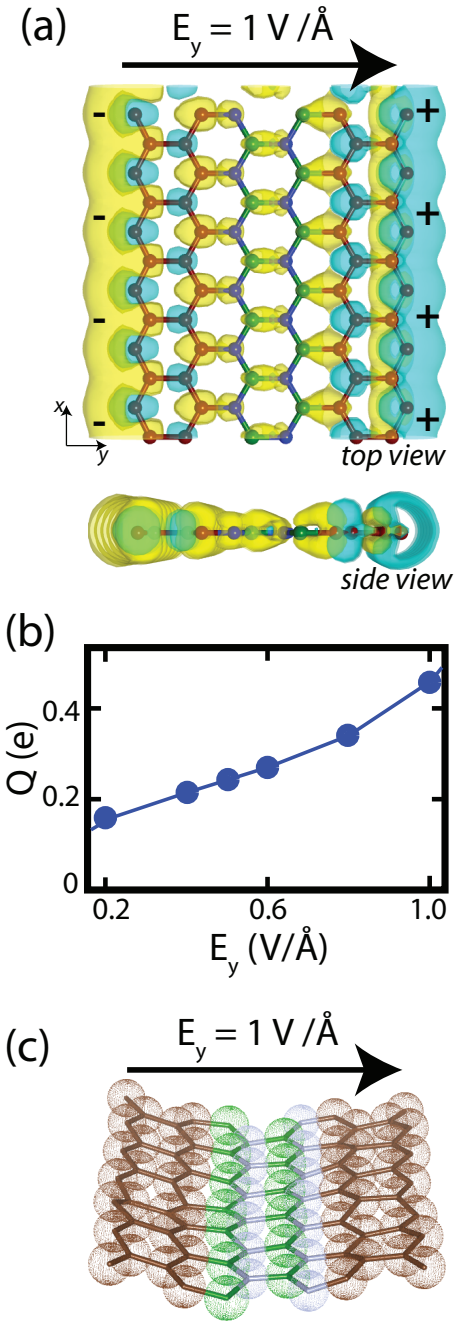

Figure 5.5: (a) Atomic configuration of ZGNR(p)+ZBNR(q)+ZGNR(p) composite ribbon with p=4, q=4. External electric field E_y is applied along y-direction in the plane of the composite ribbon extending along the x-direction. Top and side views of the isosurfaces of the difference charge density $\Delta\rho(\mathbf{r}, E_y)$ show that the left ZGNR(p) is negatively charged while the right graphene is positively charged. (b) Variation of excess charge accumulated in graphene nanoribbons at both side of BN, Q with the applied electric field E_y. (c) Snapshot taken from the MD simulation of the nanoribbon at 300K under external electric field.

have been explored.[74, 12, 77] Here we present an interesting features of composite nanoribbons, which may lead to various technological applications. For example, single layer ZGNR(p)+ZBNR(q)+ZGNR(p) composite and commensurate nanoribbon that is composed of one dielectric nanoribbon of BN placed between two metallic graphene nanoribbons with zigzag edge can allow charge separation of opposite polarity under an external electric field, E_y applied along y-direction and hence can lead to energy storage. The configuration of this device is described in Fig. 5.5(a). The atomic structure is optimized for a given external electric field E_y, and the excess charge in the left and right graphene stripes $\pm Q(E_y)$ is calculated from the difference charge density, $\Delta\rho(\mathbf{r}, E_y) = \rho(\mathbf{r}, E_y) - \rho(\mathbf{r}, E_y = 0)$. Here, $\rho(\mathbf{r}, E_y)$ is the self-consistent charge density of the device calculated for a given E_y. In Fig. 5.5(a) we also show the isosurfaces of difference charge density. The variation of $q(E_y)$ as a function of E_y is given in Fig. 5.5 (b). Once the charge separation of opposite polarity is attained under the external field E_y, it can be kept for a long time even if $E_y \to 0$ since the insulating ZBNR(q) hinders the tunneling of electrons from left to right. Alternatingly, one can also construct double well resonant tunneling structures, ZGNR(p)+ZBNR(q)+ZGNR(p) with interesting resonant tunneling effects and multiple quantum well structures, even Wannier ladders.

Here we address the questions of whether the application of the external electric field in the range of 1 V/Å might be unrealistically high or whether ZGNR(p)+ZBNR(q)+ZGNR(p) composite nanoribbon will breakdown/discociate even if such high fields are realized in an experiment. Previously, diffusion of H atom on graphene under an external field of 0.01a.u (=0.5V/Å) was studied and no instability in the graphene layer was reported.[87] Similarly, dissociative adsorption of hydrogen on nitrogen-doped graphene was studied under the electric field values ranging between 0 and 0.5V/Å .[88] Neither of these theoretical studies report breaking of the carbon-carbon bonds in graphene under electric field values in the range of 1 V/Å . Furthermore, in another theoretical study investigating the tuning of electronic and magnetic properties of H and F doped graphene even higher electric field values up to approximately equal to 10 V/Å were used on graphene without any instability.[89]. Similarly, in-plane electric field in the range of 0.15 V/Å was used for the alignment of graphene nanoribbons.[90] Experimental studies controlling the rippling or work function of graphene suggest that graphene can withstand electric fields in the order of 1 V/Å .[91, 92]

To test the stability of the composite ZGNR(p)+ZBNR(q)+ZGNR(p) nanoribbon, we performed ab-initio molecular dynamics calculations at 300 K under E_y=1 V/Åusing the Verlet algorithm. The nanoribbon remained stable after 2 ps as can be seen from the snapshot presented in Fig. 5.5(c) . To increase the degrees of freedom for possible reconstruction, we also repeated the same simulation in a larger (3×1) unit cell at 500 K. The nanoribbon continued to maintain its stability after 4 ps simulation. Additionally, we carried out ab-initio total energy calculations to estimate the weakening of bonds under the external electric field. The energy of the ribbon increased by 1.2 eV per cell (i.e. per 6 C atoms + 3 B + 3 N atoms amounting to 17 bonds) under E_y =1 V/Å . Since the cohesive energies of pristine graphene and h-BN are calculated to be 16.2 eV/cell (per 2 C atom) and 14.5 eV/cell (per B+N atoms), respectively, the average bond energy is 5.12 eV. Accordingly, the bonds are weakened by less than 2% under the applied E_y =1 V/Å . This is rather small and does not give rise to any instability.

5.3.6 Graphene/BN nanotubes

Not only ribbons, but also nanotubes can be realized with stripes of graphene and h-BN which are parallel (or perpendicular) to the axis of the tube. Prototype nanotubes are constructed by rolling G(32)/BN(32) zigzag and G(48)/BN(48) armchair nanoribbons at specific chiral angles as shown in Fig. 5.6(a-b). Following the (n,m) labeling notation for single-wall carbon nanotubes (SWNT), these nanotubes correspond to (8x0) zigzag and (6x6) armchair nanotubes where the integers n and m denote the number of unit vectors along two directions in the honeycomb crystal lattice. Upon relaxation both of the nanotubes remain stable. The strain energy (compared to planar structure) is calculated to be 1.56 eV/cell and 1.64 eV/cell for (8x0) and (6x6) nanotubes, respectively. When electronic properties are considered, SWNT can be a metal or semiconductor depending on (n,m) or chiral angle. Interestingly, unlike SWNT both (8x0) and (6x6) nanotubes are semiconductor with band gaps of E_g=0.98 eV and E_g=1.49 eV, respectively. Briefly, single-wall nanotubes of G(p)/BN(q) composite materials bring new options over the nanotubes of these constituents.

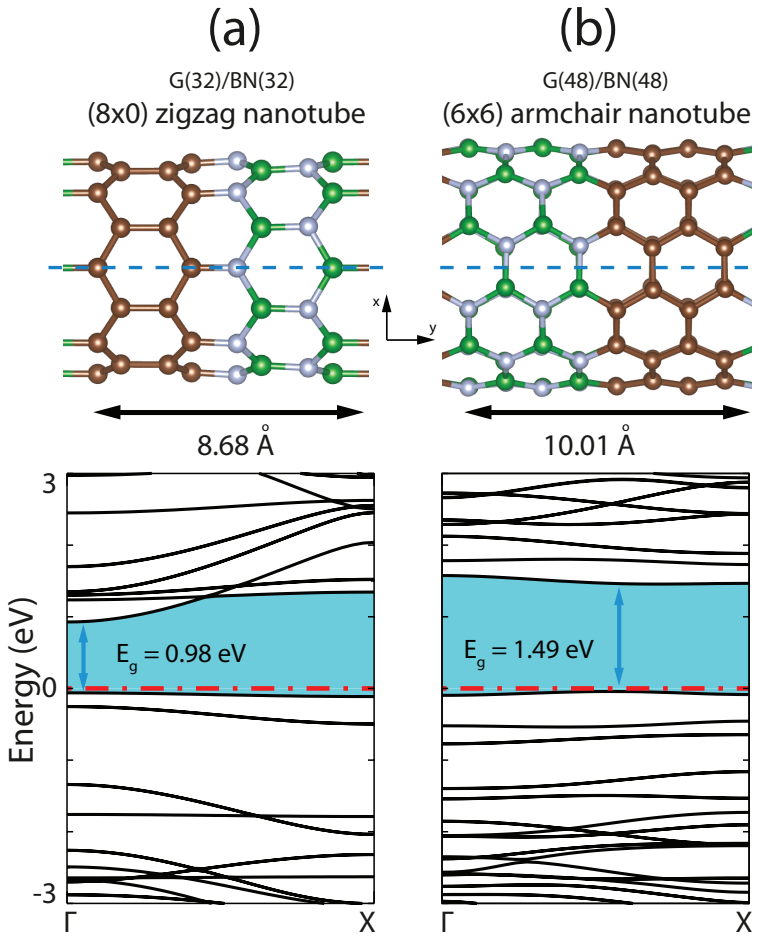

Figure 5.6: (a) Zigzag (8x0)-G(32)/BN(32) nanotube and its calculated energy band structure. (b) Armchair (6x6)-G(48)/BN(48) nanotube and its energy band structure. Band gaps are shaded. The zero of energy is set to the top of the valance band.

5.4 Summary

In spite of the fact that h-BN is a wide band gap insulator and graphene is a semimetal, G(p)/BN(q) composite can display diversity of electronic properties. Depending on the composition of p and q, as well as the edge geometry between stripes, they can be 1D metal, semiconductor with the band gap in the visible range, and semiconductor heterostructures showing periodic band gap modulation in direct space. For specific combination of p and q, phase separation is attained with interesting transition from 2D to 1D in a 2D system. By making special combination and sequences of p and q (and their graded sequences), one can achieve also graded band gap in direct space for novel optical properties. Specifically, the δ-doping of a wide stripe of graphene (BN) by the narrow BN (graphene) stripe results in unusual modifications in the electronic structure. Bi- or multilayers of composites with displaced or in-registry geometry, even with finite rotation angle between atomic planes give rise to unusual electronic properties. The novel and fundamental aspects of our results can be summarized as:

(i)While previous studies dealt with 1D aspects of lateral Graphene/BN heterostructures, present study reveals 1D, as well as interesting 2D aspects together with the transition between 1D to 2D dimensionality, which were unknown before. (ii) An extensive analysis of electronic structure for laterally repeating (periodic) graphene/BN heterostructures with varying widths is performed, which is essential for the understanding of these heterostructures and their applications. (iii) The concept of δ-doping and their dramatic effects to modify the electronic structures has been introduced to in-plane heterostructures. (iv) The charge separation in graphene/BN/graphene nanoribbons under the in-plane, external electric field leading to interesting applications. Based on ab-initio calculations, it has been shown that the nanoribbon can remain stable under the application of high electric fields.

It should be noted that similar in-plane heterostructures can be produced between lattice matched, single layer transition metal dichalcogenides[86] (such as MoS_2/WS_2), III-V compounds[63] (such as GaN(p)/AlN(q)), pseudomorphic silicene(p)/germanene(q)[93] or silicene(p)/phosphorene(q) yielding a manifold of electronic and magnetic properties. Consequently, composite structures with

their planar single and multilayers, composite nanoribbon and tubular forms keep the promise of developing a way of designing novel electronic and magnetic materials.

Chapter 6

Planar Nanoscale Dielectric Capacitors

6.1 Overview

The concept of planar graphene / boron nitride heterostructures discussed in the previous chapter and the charge separation achived in their nanoribbons by means of external electric field can be further extended to model planar nanocapacitors. Thus, in this chapter we show that *planar nanoscale dielectric capacitors* (PNDCs) can be realized as a one-atom-thick, single layer honeycomb structure consisting of a BN stripe as dielectric spacer between two metallic graphene stripes. These laterally stacked stripes are lattice matched. Furthermore, using these PNDCs, one can achieve high energy storage, as well as high gravimetric capacitance values, which are comparable to those of supercapacitors. As an alternative to NDCs consisting of vertically stacked dielectric layers capped by two metallic graphene discussed in Chapter 3, PNDCs achieve charge separation between two separated, parallel metallic stripes embedded in the same atomic plane.

It was shown experimentally [12, 76, 75] that monolayer metallic graphene and dielectric BN can be grown commensurately with desired periodicity and with sharp boundaries. Thus one can construct not only single planar capacitors

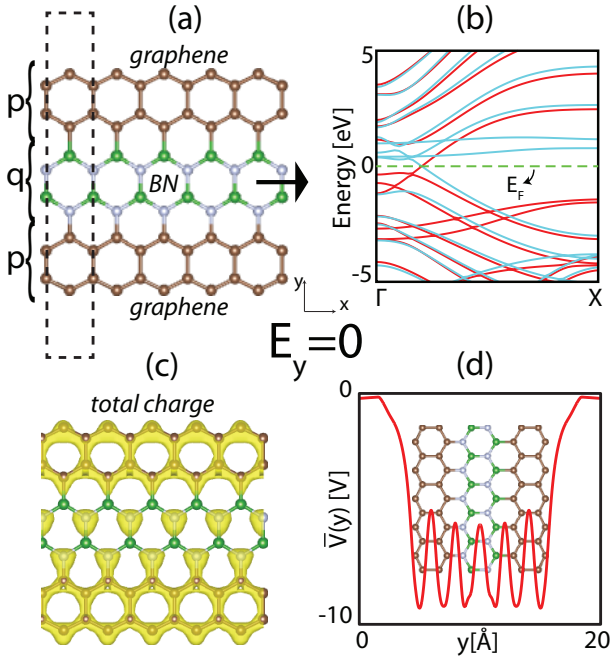

Figure 6.1: (a) PNDC formed by a zigzag BN stripe placed between metallic graphene stripes, which display 1D translational periodicity along x-direction. The unit cell is delineated by dashed lines. p and q are number of atoms in graphene and BN stripes in the unit cell. (b) Electronic band structure of PNDC under zero bias voltage (or E_y=0), where spin up and down states are shown with red(dark) and blue(light) lines, respectively. (c) Total charge density $\rho(\mathbf{r})$ isosurfaces of PNDC. (d) (xz)- plane averaged electronic potential, $\bar{V}(y)$.

but also various series and parallel combinations of the former to achieve higher potential difference or charge separation. Thus PNDCs predicted in the present study will make an important forward step towards the fabrication of atomically thin circuitry based on graphene/BN lateral heterostructures [78, 72] to allow microwave, as well as heat and pressure sensing applications.

6.2 Method

We carry out first-principles, spin-polarized calculations within density functional theory, where the eigenstates of Kohn-Sham Hamiltonian are expressed as linear combination of numerical atomic orbitals. The exchange-correlation potential

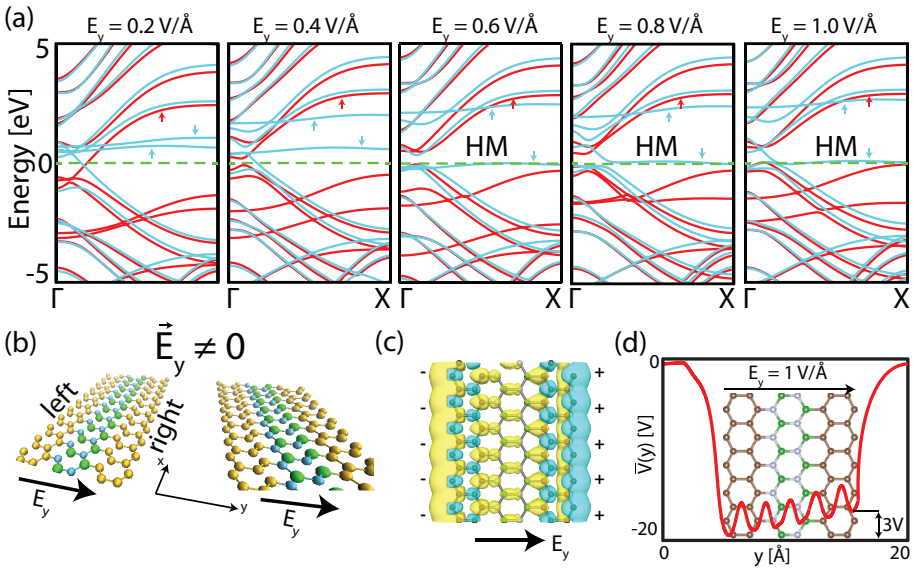

Figure 6.2: (a) Evolution of the energy bands of PNDC[4/4/4] under applied electric field $\vec{E}_y$. Shifts of relevant spin bands are indicated by arrows. For $E_y \geq 0.6$ V/Å, PNDC becomes a half-metal (HM). (b) A perspective view of the array of PNDC[4/4/4] periodically repeating along y-axis. (c) The isosurface of difference charge density, $\Delta(\rho)$, showing the charge separation, where the right graphene stripe is depleted from electrons, which are in turn deposited to left graphene stripe due to the shifts of bands under $\vec{E}_y$. (d) (xz)-plane averaged electronic potential $\bar{V}(y, \vec{E}_y)$ exhibiting a potential difference of $\Delta\bar{V}(y)$=3V under E_y=1 V/ Å.

was approximated by Perdew, Burke and Ernzerhof functional. [58] A 200 Ryd mesh cut-off was chosen. Core states were replaced by norm-conserving, non-local Trouiller-Martins pseudopotentials. [59] Atomic positions and lattice constants were optimized using the conjugate gradient method by minimizing the total energy and atomic forces for each configuration. Dipole corrections [60] were applied in order to remove spurious dipole interactions. All numerical calculations were performed using the SIESTA code.[21]

6.3 Results and Discussions

6.3.1 Model

Our model of PNDC described in Fig. 6.1(a) is composed of lateral stacking of two narrow, zigzag graphene nanoribbons (stripes), ZGNR(p) and a zigzag BN nanoribbon, ZBNR(q) in between. Here p and q indicate the number of C and B-N atoms in their unit cells, respectively. Bare ZGNR(p) and ZBNR(q) are metallic. When saturated by hydrogen atoms, ZBNR(q) nanoribbon transforms into an insulator[62]. Similarly, when joined to graphene nanoribbons commensurately at both sides, the same ZBNR(q) can function as a dielectric spacer, while the graphene nanoribbons continue to be metal. These stripes can be set to desired widths by changing p and q values. While these three lattice matched graphene/BN/graphene composite stripes preserve their translational periodicity along x-axis and acquire 1D character, the translational symmetry is broken along y-direction. This model is treated by using periodic boundary conditions, where 1D PNDCs are repeated periodically along y- and z-axis keeping 10 Å vacuum spacing between them. The electronic structure of PNDC[p/q/p] structure under zero bias ΔV=0 (or $\vec{E}_y$=0) is shown in Fig. 6.1(b). It has spin polarized ground state with magnetic moment μ= 2.3 μ_B. Graphene-like and BN-like bands are separated in the direct space and Fermi level is pinned at graphene sides while BN remains as an insulator. As seen in Fig. 6.1(c), owing to the different ionicities of C, N, and B; a minute charge is transferred across the zigzag interface even for $\vec{E}_y$=0. However, this does not lead to a capacitive behavior. In fact, the (xz)-plane averaged electronic potential $\bar{V}(y)$ in Fig. 6.1(d) indicates a vanishing potential difference, i.e. $\Delta\bar{V}(y)$=0 between graphene stripes.

6.3.2 Application of Electric Field

Normally, when connected to a real electric circuit, separation of charges of opposite polarity is attained between graphene stripes of PNDC under the applied external bias voltage ΔV, whereby the chemical potentials at metallic graphene stripes shift by eΔV. In this non-equilibrium state an electric field is generated across the BN stripe. Here for the reason explained above, we simulate this normal operation of PNDC by applying an electric field $\vec{E_y}$ along the y-direction with magnitude in the range of 0 V/Å to 1 V/Å. Notably, even if E_y=1 V/Å appears to be high, in earlier studies such high field values were attained [87]. For each value of applied $\vec{E_y}$, we first carried out calculations to optimize the atomic structure and lattice constants of PNDC by minimizing the total energy and atomic forces. Also, for each value of applied $\vec{E_y}$ we calculated the electronic energy bands of optimized structures as well as the net charge on the left graphene stripe, $-Q$ in e/cell. This is obtained from the integral

$$-Q = \int \Delta\rho(\mathbf{r}, \vec{E_y}) d\mathbf{r} \tag{6.1}$$

computed in the part of the PNDC unit cell corresponding to the left graphene stripe, where the boundary between the left (right) graphene and BN stripe bisects C-B (N-C) bonds. Here the difference charge density corresponding to a given applied field $\vec{E_y}$ is calculated as

$$\Delta\rho(\mathbf{r}, \vec{E_y}) = \rho(\mathbf{r}, \vec{E_y}) - \rho(\mathbf{r}, \vec{E_y} = 0) \tag{6.2}$$

where the total charge density of the PNDC under $\vec{E_y}$=0 is subtracted from the total charge density under the applied $\vec{E_y}$, and

$$\rho(\mathbf{r}, \vec{E_y}) = -e \sum_{n,k,\sigma}^{occ} \Psi^*_{n,k,\sigma}(\mathbf{r}, \vec{E_y}) \Psi_{n,k,\sigma}(\mathbf{r}, \vec{E_y}). \tag{6.3}$$

Here, $\Psi_{n,k,\sigma}$ indicates the spin polarized electronic state. The same analysis was also performed for the right graphene stripe which is charged positively. It should be noted that the total charge density, $\rho(\mathbf{r}, \vec{E_y})$ integrated over the entire unit cell has to be zero, which has been verified also for each value of applied $\vec{E_y}$.

According to the atomic model presented in Fig. 6.1 and Fig. 6.2, the states of two graphene stripes have small coupling and hence their bands are split in momentum space. The evolution of the energy bands with applied electric field $\vec{E_y}$ is presented for 0.2 V/Å$\leq E_y \leq$ 1.0V/Å in Fig. 6.2(a). Two unoccupied spin down bands (indicated with small arrows) shift in opposite directions, where the one associated with the left graphene stripe moves down and starts to become occupied. Concomitantly, a partially occupied spin up band associated with the right graphene stripe rises and hence becomes gradually depopulated. This situation explains how the charge and spin separations are achieved. Interestingly, for $E_y \sim 0.6$ V/Å the PNDC becomes a *half-metal* with μ=2.0 μ_B. Similar half-metallic behavior in charged graphene/BN composites were also reported before. [79, 94, 95] The shorting of graphene stripes and hence the shorting of PNDC is hindered by the dielectric BN spacer between graphenes.

In Fig. 6.2(c) we present the difference charge density, $\Delta\rho(\mathbf{r}, \vec{E_y})$ of the PNDC under the field of E_y=1 V/Å. The electron transfer from the right graphene stripe to the left stripe and the charge separation is clearly seen. In Fig. 6.2(d), we show (xz)-plane averaged electronic potential $\bar{V}(y)$. The potential at the left graphene stripe is lowered relative to the right graphene stripe, which is in compliance with the normal operation of PNDC. The electronic potential difference between two graphene stripes is calculated as $\Delta\bar{V} = 3$ V under E_y=1 V/Å.

In Fig. 6.3(a-b) we present the variation of calculated charge Q and stored energy E_s as a function of $\vec{E_y}$. The energy stored on PNDC as a function of $\vec{E_y}$, is obtained from the expression

$$E_s(\vec{E_y}) = E_T(\vec{E_y}) - E_T(\vec{E_y} = 0), \tag{6.4}$$

where $E_T(\vec{E_y})$ is the total energy calculated for a given applied field $\vec{E_y}$. Using the values of Q and E_s calculated for a given $\vec{E_y}$, the capacitance per unit mass C can be obtained from

$$C = Q^2/2mE_s, \tag{6.5}$$

where m is the mass of PNDC per unit cell. The variation of the capacitance as a function of $\vec{E_y}$ is shown in Fig. 6.3(c), which is high at small $\vec{E_y}$ (or bias voltage V) and gradually saturates to a constant value.

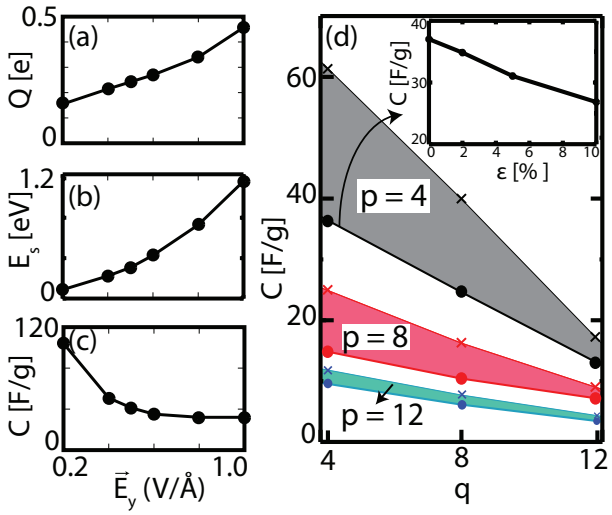

Figure 6.3: (a) Variation of excess charge Q (e/cell); (b) stored energy E_s (eV/cell) and (c) the corresponding gravimetric capacitance C (F/g) for PNDC[4/4/4]. (d) Capacitance C values in (F/g) of the planar nanoscale dielectric capacitor PNDC[p/q/p] are calculated for p=4-12 and q=4-12 for specific value of E_y for which C saturates. For each value of p, lower line connected by dots corresponds to capacitance values calculated through the expression, $C = Q^2/2mE_s$, while the upper line connected by crosses is computed from $C' = Q/m\Delta\bar{V}$. The calculated variation of C with tensile strain, ϵ is shown by inset.

6.3.3 Size Dependence of Capacitance

To explore the effect of size of PNDC[p/q/p] we repeated our analysis for different widths of graphene and BN stripes, namely for different p and q. Moreover, because of uncertainties involved in the effective widths of metallic and dielectric stripes (hence in the boundaries of the integral given in equation 6.1), which affect the calculated values of Q and C, here we present two alternative approaches in calculating C. In the first approach, C is calculated from the expression $C = Q^2/2mE_s$, where Q and E_s correspond to $\vec{E_y}$ leading to the saturated values of C as shown in Fig. 6.3(c). In the second approach, we followed the definition of the capacitance as $C' = Q/m\Delta\bar{V}$. Results obtained from these two alternative calculations are presented in Fig. 6.3(d), where the capacitances of PNDCs are plotted for different q values. For both approaches, C decreases as q increases. Also C decreases as the width of graphene stripe p, increases. However, the difference between the values of capacitance calculated by using two alternative approaches, namely $C' - C$ increases for small p and q, but decreases and eventually diminish as p and q get larger.

The capacitance values of PNDCs are found to depend strongly on the external conditions. For example, as shown by inset in Fig. 6.3(d), C[4/4/4] changes by $\sim 30\%$ under the tensile strain of ϵ=10%, which can be detected easily and may offer technological applications. Similarly, when deformed under normal force or pressure, a PNDC can be deformed, whereby geometric parameters such as the effective width of BN, w is modified. Also, the energy barrier, Φ for electrons tunneling from left graphene to right graphene between two graphene stripes can be modified with local forces. Consequently, the capacitance value of PNDC is modified by local force or pressure. Capacitance value can also vary with the ambient temperature, since charge separation and hence Q, can be modified by the Fermi-Dirac distribution at finite temperature. Consequently, PNDCs can function as pressure and temperature sensors, when embedded in a soft materials like peptides or artificial tissues. It is noted that graphene/BN/graphene junctions of PNDC with small w can work also as tunneling diodes or resonant tunneling device, where the tunneling current I_t can be monitored by mechanical deformation, bias voltage or by temperature. Accordingly, these junctions also attain critical functionalities. Notably, all these features discussed above can be realized in diverse geometries, in particular in tubular forms.

Next we consider a series combination of PNDC[p/q/p] which is composed of commensurate sequential stripes, graphene(p)/BN(q)/graphene(2p)/BN(q)/graphene(p) stacked laterally. Accordingly, the middle graphene stripe has the twice width of the graphene stripes at either side of series PNDC. Under the applied electric field the excess negative and positive charges were accumulated at the far left and right edges of the middle graphene(2p). The capacitance of this series combination was calculated as half of the capacitance of PNDC[p/q/p], namely C_{eq} = C[p/q/p] / 2. This demonstrates that to attain the desired Q or E_s or ΔV various combinations PNDC can be achieved on a single honeycomb structure by arranging metallic interconnects between parallel graphene stripes (which are graphene nanoribbons by themselves).

6.4 Summary

In this chapter, we proposed and characterized a model for planar nanoscale dielectric capacitor consisting of a single layer, insulating hexagonal boron nitride (BN) stripe placed between two metallic graphene stripes, all forming commensurately a single atomic plane. Our first-principles density functional calculations on these nanoscale capacitors for different levels of charging and different widths of graphene - BN stripes mark high gravimetric capacitance values, which are comparable to those of supercapacitors made from other carbon based materials. Present nanocapacitor model allows the fabrication of series, parallel and mixed combinations which offer potential applications in 2D flexible nanoelectronics, energy storage and heat-pressure sensing systems.

Chapter 7

Carbon and Boron Nitride Chains

So far, we discussed carbon and boron nitride composite nanostructures in their planar honeycomb geometries. However, the composites of these elements are not restricted to monolayer structures. Single atomic chains are interesting entities which can be used to functionalize substrates for diverse electronic and magnetic applications. With this regard, carbon atomic chains, containing n C atoms, indicated as CAC(n) hereafter has recently drawn attention due to its linear geometry, high strength, size-dependent quantum ballistic conductance and interesting electronic properties. These properties of CACs were both theoretically[96, 97, 98] and experimentally[99, 100, 101] investigated. Concomitantly, carbon atomic chains are synthesized, which have also been justified by the images obtained earlier using high resolution TEM.[102]

In this chapter, we describe the adsorption of carbon adatoms on h-BN and their dynamics and address the question of whether short CACs can be grown on monolayer boron nitride. We first examine the adsorption of single carbon atom on boron nitride by calculating its energy landscape and diffusion barrier. This is followed by the investigation of the nucleation and growth processes of CACs on h-BN. We perform both conjugate gradient calculations and molecular dynamics simulations in order to determine the stabilities and bonding properties of these CACs and show how they can grow on the plane of BN as new carbon

atoms are introduced by one atom at a time at the close proximity of a CAC. Next, we investigate the binding sites, binding energies and binding geometries of these chains. We present the electronic energy band structure for various lengths of chains to see their variations with the number of chains. In addition, we investigate CACs creating active bonding sites of h-BN for certain adatoms and molecules. We finally show that CACs can be formed between two parallel single layer h-BN flakes as if pillars.

7.1 Adsorption of Carbon Atom on Boron Nitride

Before going into detailed studies of carbon chains, we first investigate the adsorption and migration of single carbon adatom, which is the starting point of CAC growth on boron nitride substrate. We use a (4×4) supercell of h-BN that consists of 16 boron and 16 nitrogen atoms. Spin polarization tests showed that there is an energy difference of $\sim 0.2eV$ between the spin polarized and spin unpolarized energy values in favor of the spin polarized state, indicating that the system has a magnetic ground state. Therefore all of the calculations mentioned hereafter are performed using the spin polarized conditions.

The most favorable binding site of single carbon atom was determined by placing the adatom initially to various adsorption sites at a height of ~ 2Å from the BN plane and running fully self-consistent geometry optimization calculations by keeping the adatom fixed in $x-$ and $y-$ directions and letting the vertical $z-$coordinate of the adatom, which is its height from the plane, free. Meanwhile, the atoms in the BN supercell are relaxed in all directions except for one corner atom of the supercell, which is fixed in all directions to prevent BN from sliding.

In Fig. 7.1(a) nitrogen and boron atoms of optimized h-BN structure are separated from each other by 1.45Å. The most favorable bonding site of single carbon ad-atom, which turns out to be near the top site of nitrogen atom, is marked with a red star. The energy landscape calculated over the whole BN hexagon also shows that the energy barrier to the diffusion further increases as the carbon

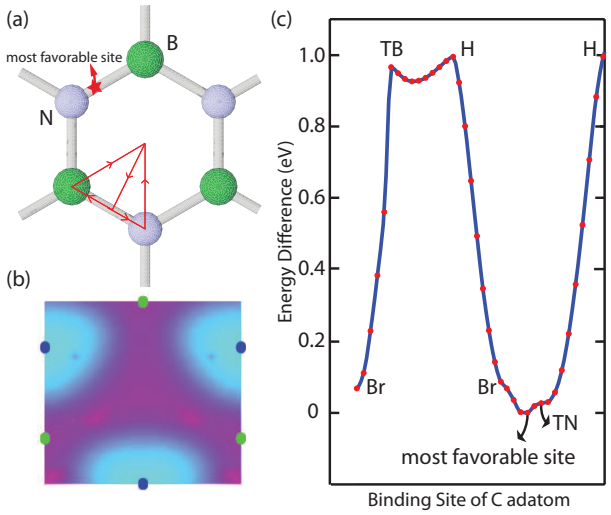

Figure 7.1: Energy variation of single carbon atom adsorbed on various sites of single layer, 2D hexagonal BN structure (h-BN) calculated in (4×4) supercell. (a) Boron nitride honeycomb structure on which the adsorption energies are calculated. Nitrogen and boron atoms are represented by blue and green balls, respectively. The most favorable binding site of C adatom is marked by the red star in the figure. (b) Complete energy landscape of C adatom on h-BN structure. Light blue regions show favorable sites and the energy barrier further increases as the color goes to dark blue and purple. The potential barrier for the carbon atom is $\sim 0.65eV$ (c) Energy variation of C ad-atom is shown along the path indicated by red arrows in (a). The energy difference between the most favorable site (indicated by red star) and the bridge(Br), top boron(B), hollow(H), top nitrogen(TN) sites are calculated as $0.07eV$, $0.95eV$, $1.00eV$ and $0.03eV$, respectively.

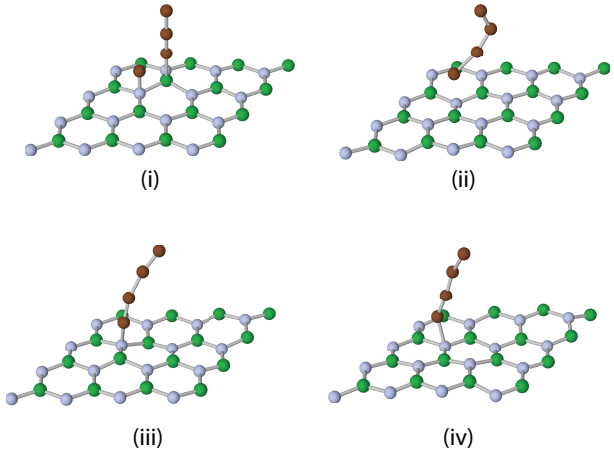

Figure 7.2: Snapshots of the molecular dynamics simulation showing the formation of a short chain comprising four carbon atoms. The snapshots correspond to the initial, 20th, 40th and 120th steps of the molecular dynamics simulation done at 500K. Note that the formation of CAC(4) takes place as the CAC(3)leaves its initial bonding position and attaches to a single carbon ad-atom. Similar growth mechanism is also seen during the formation of CACs of length $n \leq 8$.

atom moves away from the nitrogen atom as shown in Fig. 7.1(b). Energy variation diagram, calculated along the 2D path shown in Fig. 7.1(a) is presented in Fig. 7.1(c). As indicated in the figure, the most favorable site for the carbon atom is near the top nitrogen site, although not exactly on top of nitrogen. The energy barrier between the most favorable site and the top bridge(BR), top boron(TB), hollow(H) and top nitrogen(TN) sites were calculated as $0.07eV$, $0.95eV$, $1.00eV$ and $0.03eV$ respectively.

In addition to the diffusion path analysis of a single carbon ad-atom, we next study the interaction between two carbon atoms on BN surface. When the distance between the two ad-atoms becomes less than a threshold distance of ~ 2Å, these two carbon atoms attract each other and form a CAC(2) of two atoms, which is indeed the nucleation of longer CACs. The energy barrier for the diffusion of single C ad-atom on BN is calculated as $0.68eV$. The most favorable binding site CAC(2), is again near the top site of nitrogen. A complete site analysis was also performed to confirm this result, by placing a CAC(2) on various adsorption sites and comparing the total energy values.

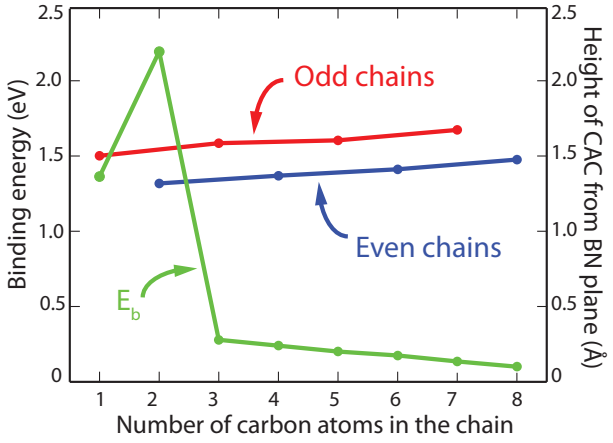

Figure 7.3: Binding energies (E_b), and the heights(h) of odd and even numbered CACs from the atomic plane of BN are shown in green, red and blue lines, respectively. The h values exhibit an even/odd family behavior depending on the number of carbon atoms in the chain. The sudden peak in the binding energy arises from the change of the magnetic state of CAC(2) from magnetic to non-magnetic when it binds to hexagonal BN.

7.2 Carbon Chains

7.2.1 Chain growth and even/odd disparity

Growth of the CAC further continues when a third carbon adatom is introduced at the close proximity of CAC(2). However, this time a complete site analysis of CAC(3) shows that the most favorable bonding site is near the top boron site instead of the nitrogen site. The formation of CAC(3) happens as follow: CAC(2) leaves its initial bonding position, moves higher from the BN plane and in the mean time it gets closer to the single adatom until they are bound to each other near the new energetic site, which is the top boron site. Similar chain growth behavior is also seen during formation of CACs at different lengths. This process is further investigated with molecular dynamics simulations at 500K and the snapshots taken from the growth of CAC(4) is presented in Fig. 7.2. We initiate the MD simulation by placing a carbon adatom and a CAC(3) to their bonding sites as shown in Fig. 7.2(i). The simulation was run for 2000 time steps and snapshots taken from the initial, 20^{th}, 40^{th}, and 120^{th} time steps are shown. As

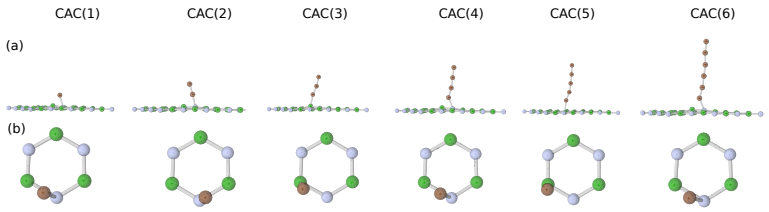

Figure 7.4: Side and top views of the most favorable binding configurations of CAC(n) on hexagonal BN are shown in (a) and (b). N, B, and C atoms are represented by blue, green and brown balls, respectively. CAC(n)'s having an even number of carbon atoms (even n) bind to BN near the top of nitrogen atom, whereas CAC(n)'s with odd number of carbon atoms (odd n) prefer top boron site, with the exception of single carbon adatom. The geometries are calculated for a (4×4) supercell and their stabilities are tested with MD simulations at $T = 500K$ for $10ps$. In (b), only the carbon atom that is closest to the BN plane is shown.

the simulation proceeds to the 2000^{th} step, the chain stays in its position shown Fig. 7.2(iv), which is an indication of its stability at that bonding site.

We further continue our analysis with fourth, fifth, sixth and seventh carbon adatoms. With the inclusion of each new carbon atom, we observe that each time a new adatom is introduced to the system, the previous CAC(n-1) chain leaves its binding site and is bound to the new carbon adatom in their new most favorable binding site. Namely, this binding site keeps changing between the near top nitrogen site and the near top boron site. With the exception of the single carbon adatom, we observe an even/odd disparity of the binding site depending on the number of atoms in the CAC, that is even numbered CACs bind to h-BN substrate near the top nitrogen site, and the odd numbered CACs bind near the top boron site. A complete list of the binding energies and binding geometries of these CACs are presented in Table I.

It is also seen that, with the exceptional case of CAC(2) which is further discussed in the following section, the binding energies of the CACs tend to decrease as the length of the chains increase. Similarly, due to the decrease in the binding energy the height(h), namely the distance between the BN plane and the first carbon atom of the CAC, also increases. However, the h values also show an even/odd disparity. In other words, there is an increasing trend in the h values

Table 7.1: Most favorable binding sites, binding energies(E_b), magnetic moments(μ), heights(h) of CAC(n) from the BN plane, and the distances of the lowest carbon atom of the chain from the nitrogen(d_{C-N}) and the boron(d_{C-B}) atom in the BN plane for different n's of carbon chains. The bonding sites and magnetic properties of CACs on BN exhibit an even/odd disparity. With the exception of the single carbon ad-atom, even numbered CACs bind to BN near the top of nitrogen(TN) atom and the odd numbered CACs bind near the top of boron(TB) atom. Additionally, the even and odd numbered chains grown on BN have magnetic and nonmagnetic(NM) ground states, respectively, with the exception of CAC(1) and CAC(2) cases.

Structure	Site	$E_b(eV)$	$\mu(\mu_B)$	h(Å)	d_{C-N}(Å)	d_{C-B}(Å)
BN+C	∼TN	1.36	2.00	1.50	1.59	1.73
BN+CAC(2)	∼TN	2.19	NM	1.32	1.46	1.83
BN+CAC(3)	∼TB	0.28	NM	1.59	2.16	1.62
BN+CAC(4)	∼TN	0.24	2.00	1.37	1.50	1.63
BN+CAC(5)	∼TB	0.20	NM	1.60	2.28	1.62
BN+CAC(6)	∼TN	0.18	1.97	1.41	1.52	1.58
BN+CAC(7)	∼TB	0.14	NM	1.67	2.41	1.64
BN+CAC(8)	∼TN	0.08	1.96	1.48	1.56	1.59

when the CACs are grouped as even and odd numbered chains, but the height of CAC(2n) is always less than CAC(2n-1), as shown in Fig. 7.3. This situation can be explained by the fact thats the C-N bond length is shorter than the C-B bond length, and CAC(2n) is a more stable structure since it has a more symmetrical charge distribution as compared to CAC(2n-1). These decrease h distances of the even numbered CACs that are bound to the nitrogen atom.

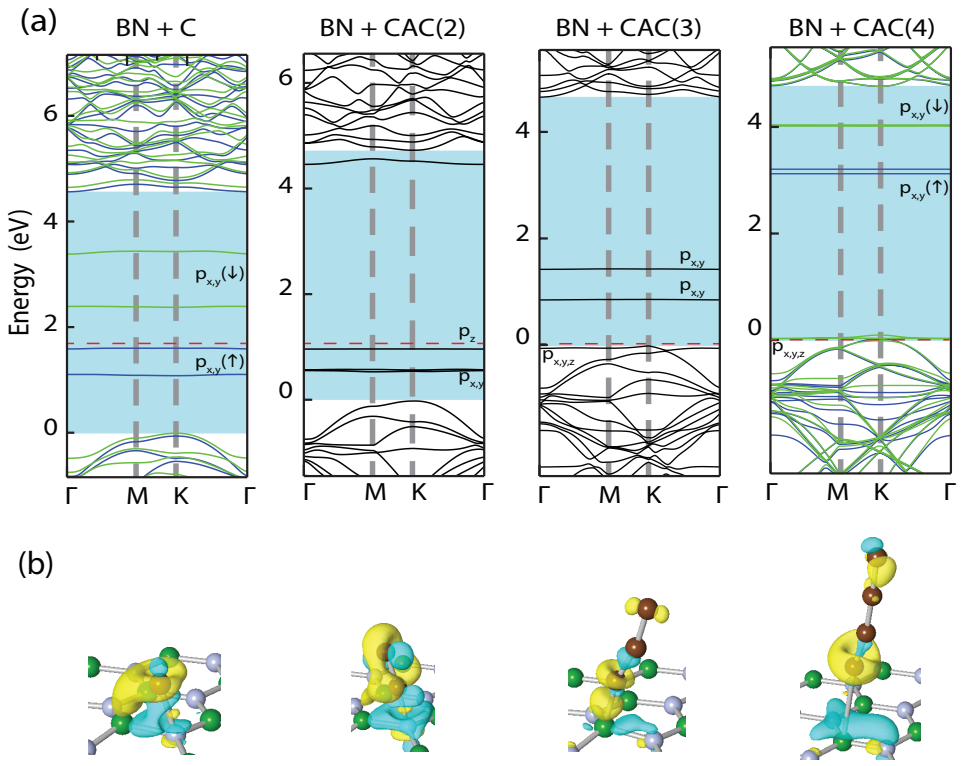

Figure 7.5: (a) Electronic energy band structures of CACs grown on h-BN calculated for n= 1, 2, 3 and 4. In the magnetic cases, spin up and spin down bands are represented by blue and green lines, respectively. The localized impurity states arise from the p bands of the carbon atoms that are at the edges of chains. (b) Isosurfaces of the difference charge densities of chains where yellow and green regions designate charge accumulation and charge depletion, respectively. The isosurface values are taken as 0.01 electron/Å^3 for C, C_2, C_3 and as 0.005 electron/Å^3 for C_4.

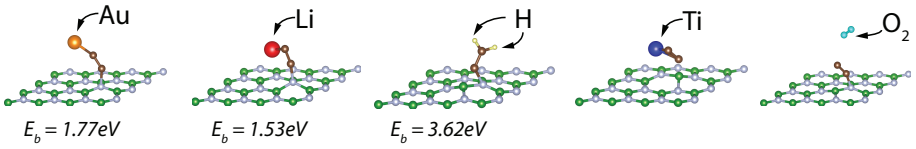

Figure 7.6: Functionalization of BN sheets through adsorption of carbon chains. For examle, a CAC(2), which is strongly bound to h-BN, creates chemically active sites for Au, Li and H atoms. H_2 molecule approaching to CAC(2) from sides dissociated to form two C-H bonds, whereas O_2 remains totally inactive. Ti atom takes the carbon atoms with itself and forms TiH_2.

We finally test the stability of these BN+CAC structures at various temperatures with molecular dynamics simulations. The ab-initio MD calculations were carried out for $10ps$ at $T = 500K$. The final stable bonding configurations of various CACs are shown in Fig. 7.4. These CACs on BN are stable and they don't detach from the BN plane, but they slightly pull the bonding B and N atoms upwards from the plane, as seen from the side views given in Fig. 7.4(a). Also, the chains are not perfectly perpendicular to the BN plane, but are slightly tilted at different angles. Fig. 7.4(b) shows the top views of the CACs, where only the carbon atoms closest to the BN planes are shown. As noted above, the even/odd disparity in the bonding sites of the chains with the exception of single carbon atom can be seen.

7.2.2 Electronic and magnetic properties

Having found the geometrical properties of CACs on BN, we next focus on the variation of magnetic and electronic properties of BN with various lengths of CACs attached. First, we perform both spin polarized and spin unpolarized energy minimization calculations for CACs of various lengths without attaching them to h-BN and compare the minimum energies of magnetic and non-magnetic cases. In a similar manner with the optimized structures of CACs attached to h-BN, it turns out the magnetization of bare(pure) CACs also depends on the number n of carbon atoms. Namely that a bare chain has magnetic ground state if it has even number of carbon atoms, and a non-magnetic ground state if it has odd number of carbon atoms with the exception of single carbon atom in

vacuum. Hence, when these chains are adsorbed to h-BN sheet, the overall magnetic moments of the BN+CAC(n) structures don't change with the exception of CAC(2). While all other CACs preserve their magnetic ground states when bonded to BN, CAC(2) flips from the magnetic ground state to the non-magnetic ground state. This change in the magnetic moment of CAC(2) increases its bond strength with h-BN and causes a higher binding energy. This is the reason for the sudden jump in Fig. 7.3.

An individual CAC(n) attached to h-BN can modify the electronic band structure of h-BN. If an adsorbed CAC(n) is sufficiently far from others, it gives rise to localized states in the band gaps and resonance states in the band continua of h-BN. In this study we consider a single CAC(n) adsorbed to h-BN using a model where one CAC(n) is attached to each repeating (4×4) supercell with the condition that interactions between adjacent CACs are negligible. This model recovers approximately the (4×4) folded bands of bare h-BN, except that the energy difference between the top of the valance bands and the bottom of the conduction bands gradually increases from $4.5eV$ to $4.8eV$. Additionally, flat bands due to CAC(n) occurs in the band gap. These flat bands actually corresponds to the impurity states due to CAC(n). In Fig. 7.5(a) we present the electronic energy structure of CAC(n)+h-BN calculated for n=1,2,3 and 4 using supercell geometry explained above. The energy positions of the filled and empty flat bands in the gap are closely related with the energy levels of the corresponding CAC(n). For magnetic n=1 case, spin-up states (i.e. flat bands) originating mainly from C-p_{xy} orbitals occur above the top of valence band. Empty spin-down states of the same orbital character occur near mid gap. In the non-magnetic case of n=2 spin-degenerate C-p_{xy} and C-p_z states are filled and occur near the top of the valence band. While a filled C-p_{xyz} state touches the top of valence band both for non-magnetic n=3 case and magnetic n=4 case, the positions of empty C-p_{xy} states in the band gap strongly depend on n. For all n's the resonance states occur in the valence band gap within the energy of 2 eV from the top.

In Fig. 7.5(b) the isosurfaces of difference charge density indicate that important changes from the corresponding bare CAC is found where CAC is bound to h-BN. The difference charge density is calculated by subtracting the charge densities of bare h-BN and bare CAC(n) from that CAC(n)+h-BN system by keeping the atomic configuration of adsorbed and bare CAC unaltered.

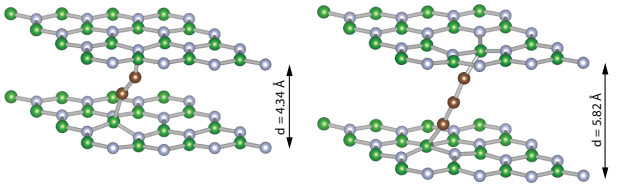

Figure 7.7: CAC(2) and CAC(3) grown between two BN flakes. The optimized spacing between the flakes increase from 3.1Å to 4.34Å and 5.82Å upon the formation of chains.

7.2.3 Functionalization of BN through CAC(2)

BN is in general not a chemically active material, however with the inclusion of certain adatoms its chemical activity can be improved. In the previous sections, we showed that CAC(2) binds to h-BN with a very high binding energy as compared to other CACs. Besides binding strongly to h-BN, it also creates a chemically active site for the absorbtion of other adatoms. Here we test the adsorbtion of Au, Li, Ti, H_2 and O_2 on CAC(2) and show that the chemical activity of BN can be enhanced through CAC(2) attached to it. Adatoms were placed in the vicinity of CAC(2) on h-BN and fully self consistent calculations were performed. Before introducing the adatoms, the CAC(2) was placed freely in its most favorable position calculated in the previous section. It was seen that Au and Li atoms move towards the chain and bind to the chemically active site of CAC(2) with binding energies of 1.77 and $1.53eV$, respectively. These are significantly higher than the binding energies of Au and Li on BN, which are calculated as 0.01 and $0.12eV$, respectively. A hydrogen molecule approaching to CAC(2) from the sides moves high and dissociates to form two C-H bonds. The binding energy for H atoms is calculated as $3.62eV$. However, when O_2 is introduced to the system instead of H_2, it stays completely inactive and stay away from CAC(2). Finally, we test Ti adatom. Ti binds to bare h-BN with an energy of $0.80eV$. However, when h-BN is functionalized with CAC(2), although Ti adatom initially binds to the carbon atoms, it doesn't stay there but takes away these CAC(s) from the BN layer and forms a TiC_2 structure which moves away from BN. This final configuration is energetically more favorable than Ti binding to h-BN by $5.9eV$. The final relaxed geometries of all these structures are presented in Fig. 7.6. These enhancement of the chemical activity of BN sheets

may be especially useful for the connection of electrodes to h-BN.

CACs can also be grown between two BN flakes as shown in Fig. 7.7. We have demonstrated this situation by calculating optimized bonding configurations and the spacing between two BN flakes when CAC(2) and CAC(3) is grown between them. CAC(2) binds to the nitrogen atom from one side and to the boron atom on the other side as shown in Fig. 7.4. On the other hand, CAC(3) binds to both of the flakes from the top boron sites. Once CAC(2) and CAC(3) are grown, the spacing between the flakes increases from 3.1Å to 4.34Å and 5.82Å, respectively. The formation energies, calculated by subtracting the energy of two BN planes and the energy of CAC from the energy of the final structure, are found as 2.0 and $0.32eV$ for CAC(2) and CAC(3), respectively.

7.3 Summary

Here we presented the nucleation and growth mechanisms of short chains of carbon atoms on single-layer, hexagonal boron nitride (h-BN), and short BN chains on graphene. Our analysis starting with the adsorption of a single carbon adatom and examined its migrations. Once a C_2 nucleated on h-BN, the insertion of each additional carbon at its close proximity caused a short segment of carbon atomic chain to grow by one atom at at a time in a quaint way: The existing chain leaved its initial position and subsequently is attached from its bottom end to the top of the carbon ad-atom. We showed that the electronic, magnetic and structural properties of these chains vertically adsorbed to h-BN depends on the number of carbon atoms in the chain, such that they exhibit an even-odd disparity. An individual carbon chain was also shown to modify the electronic structure with localized states in the wide band gap of h-BN. As a reverse situation we examined the growth of short BN atomic chains on graphene, which attribute diverse properties depending on whether B or N is the atom bound to the substrate. These results together with ab-initio molecular dynamics simulations of the growth process reveal the interesting self-assembly behavior of the grown chains. Furthermore, we find that these atomic chains enhance the chemical activity of h-BN and graphene sheets by creating active sites for the bonding of various ad-atoms and can act as pillars between two and multiple sheets of these honeycomb structures leaving wider spacing between them to achieve high

capacity storage of specific molecules.

Chapter 8

Constructing Graphyne from Carbon Chains and BN Analogue

The perpendicular atomic chains of carbon and boron nitride atoms discussed in the previous chapter are precursors for a new class of nanomaterials, called graphyne. Graphynes are two dimensional structures similar to graphene with the inclusion of double and triple bonded carbon atoms between the corner atoms of the honeycomb structure. In a sense, they can be seen as combinations of short atomic carbon chains on the same atomic plane. Much earlier than the synthesis of single layer graphene, Baughman *et al.*[103] predicted various molecules of carbon atoms in the graphyne family as layered phases containing sp^2 and sp bonds using semi-empirical and empirical atom-atom potential calculations. Based on first-principles plane wave calculation, Tongay *et al.*[98] predicted various stable 1D, 2D and 3D periodic structures containing carbon atomic chains. Among these structures, graphene-like electronic structure of 2D periodic α-graphynes is revealed. Very recently, band structures of the graphyne/graphdyne family with similar behaviors to that of single layer graphene were also calculated,[104] showing that neither the existence of hexagonal symmetry nor all atoms being chemically equivalent are prerequisites for the existence of Dirac point in the electronic structures.

Different types of the graphyne family are seen as new type of 2D materials in the future era of carbon allotropes.[105] Finite building blocks of these

graphyne structures have been synthesized which is an initial step towards extended materials.[106, 107, 108, 109] Although periodic 2D structures of graphyne have not yet been synthesized, the synthesized finite blocks hold promise for future applications. Additionally, theoretical studies and simulations have revealed that different members of the graphyne family are promising materials in electronic applications, can be used to construct graphyne-based nanotubes, and it is possible to obtain semiconducting boron nitride(BN) analogues of certain types of graphyne, which are called as BNyne throughout this manuscript. [104, 110, 111, 112, 113]

In this chapter, we investigate stability of 2D periodic α-graphyne structure and its boron nitride(BN) analogue by using first principle calculations within density functional theory. An α-graphyne structure of size n can be obtained by placing n number of carbon atoms between the corner atoms of the hexagonal graphene structure. We investigate the electronic and mechanical properties, and stabilities of different sized α-graphynes, calculate phonon modes and perform molecular dynamics(MD) simulations to test the stabilities of these structures. We find that the stability and the existence of Dirac points on the Fermi level depend on the size of the graphyne, such that n=even cases lead to stable structures with graphene like electronic structures, whereas n=odd cases lead to instabilities. In addition, the mechanical strengths of α-graphynes of various sizes were explored and compared with that of other structures. We also do similar analysis for the BN analogues of graphynes. We finally investigate the binding energies and electronic properties of bilayer structures of these materials.

8.1 α-Graphyne and α-BNyne

8.1.1 Structure

We begin our analysis by investigating the structural and geometrical properties of α-graphynes at different sizes. An α-graphyne(n) structure is obtained by placing n carbon atoms between every adjacent carbon atom of the hexagonal graphene structure. As shown in Fig. 8.1(a) this structure has a similar unitcell with graphene, but consists of $3n + 2$ carbon atoms instead of 2. In other words,

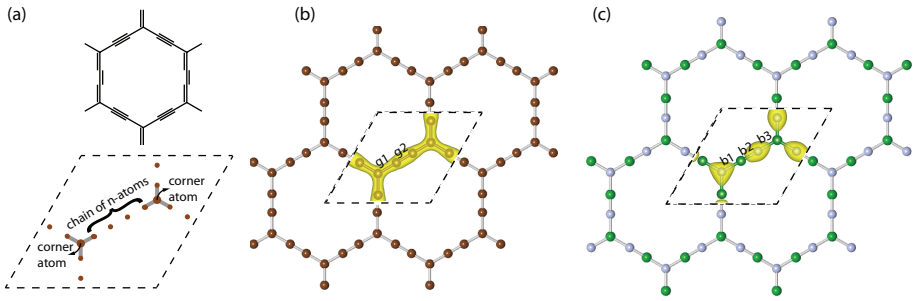

Figure 8.1: α-Graphyne and α-BNyne. (a) Schematic diagram of α-graphyne(2) and the unit cell used to generate α-graphyne(n). Two corner atoms of the hexagon have a chain of n atoms between them, such that the unit cell contains $3n + 2$ atoms. (b) Atomic structure of single layer, $2D$ α-graphyne(2). The dashed lines delineate the primitive unit cell. The optimized bond lengths are $g1 = 1.39$Å and $g2 = 1.23$Å. The total charge density is shown within the unit cell. (c) Atomic structure of single layer, $2D$ α-BNyne with blue and green balls representing N and B atoms, respectively. The optimized bond lengths are $b1 = 1.42$Å, $b2 = 1.25$Å and $b3 = 1.44$Å. In the charge density plots, the isosurface value is taken as 0.2 electron/Å^3.

we have the normal graphene structure with carbon atomic chains of length n between the corner atoms of the hexagon on each side. Contrary to graphene, all of the C-C bonds are not equivalent to each other in these structures, but there exists bonds with different lengths and charge densities as shown in Fig. 8.1(b). Therefore, the carbon atoms are no longer chemically equivalent to each other as they were in the case of graphene.

The BN analogue of this structure, namely α-BNyne, can be easily obtained by replacing the carbon atoms with B and N consecutively. The charge is transferred from B to adjacent N in the ionic bonds of α-BNyne. Here, there are three different types of bonds; two at the corners of the hexagon, one at the center of edges. For B-N bonds at the corners, one is the case when N is a part of the hexagon and B in the edge as denoted by $b1$ in Fig. 8.1(c), and the other is the opposite of this and denoted by $b3$. Note that, if we want to preserve the 2D-BN hexagonal structure such that the corner atoms of the hexagons are consecutively B and N, we must have even number of atoms between the corner atoms. That is, we can only have $n = even$ scenarios for the α-BNyne(n) cases. Odd n values would either lead to same type of atoms on the corners of the hexagons

or two identical atoms(B-B or N-N) next to each other. For this reason, we restrict ourselves with even n values for BN analogue of α-graphyne(n). The periodic geometry of these structures, and the unit cells used to generate them are shown in Fig. 8.1(b) and Fig. 8.1(c) for α-graphyne(2) and α-BNyne(2) cases, respectively.

8.1.2 Stability

Although graphyne allotropes have been widely studied in previous works, their stabilities have been an open question. Up to now, finite graphyne building blocks have been synthesized which is an indication of their stabilities. Here, the main issue is whether 2D single layer, periodic structures of the graphyne family are stable or not. Having found the optimized atomic structures, in this section we present a state-of the art analysis of phonon frequencies and MD simulations of α-graphynes and α-BNynes corresponding to any **k**-point in the BZ. When the calculated frequencies of all the modes are positive, the structure is identified to be stable. In Fig. 8.2 all calculated frequencies of α-graphyne(2) and α-BNyne(2)are positive. Moreover, due to the atomic C and B-N chains in α-graphyne(2) and α-BNyne(2) both structures have phonon modes with frequencies higher than those of single layer graphene and hexagonal BN. The situation is different for α-graphyne(4) and α-BNyne(4), since some of lowest acoustic modes have imaginary frequencies. These modes shaded out in Fig. 8.2(b) and (d) correspond to imaginary frequencies and may indicate instabilities. The imaginary frequencies may arise also as an artifact of numerical calculations; to obtain real frequencies one needs to perform calculations with very high numerical accuracies. In some cases, specific planar structures can be unstable and those structures undergo structural transformations to attain stability. In fact, ab-initio MD simulations presented below indicate the possibility of buckling of α-graphyne(4) and α-BNyne(4) in vertical planes in order to remain stable.

Hence, in order to further investigate the issue of stability, we performed MD simulations at $T = 1000K$ for $5ps$. The atomic structures obtained after the MD calculations are presented in Fig. 8.3. It turns out that α-graphyne(n) and α-BNyne(n), n=2 and n=4 remained stable after $5ps$ of MD simulation at high temperature. Even though $5ps$ is a short time interval, it is long enough for

ab-initio calculations at high temperature to provide evidence for stability. The analysis of atomic structures also suggest that α-graphyne(4) and α-BNyne(4) prefer to buckle in the vertical direction in order to gain stability. α-Graphyne(1) is totally unstable and is dissociated into carbon atomic strings. α-Graphyne(3) undergoes a structural transformation and acquires stability by changing the number of C atoms to $n = 2$ and $n = 4$ in the adjacent edges of hexagon. This transformation is derived to maintain the proper bond order of finite size carbon atoms constituting the edges of hexagon.[114] While the carbon atoms at the corners are always forming single bonds with the adjacent carbon atoms, the second atom from the corner by itself has to make a triple bond with the adjacent carbon atom, which is at the other side in the edge of the hexagon. At the end, the correct bond order of carbon atoms are preserved. However, this structural transformation modifies the geometric structure and symmetry.

8.1.3 Mechanical properties

Having found the stable α-graphyne and α-BNyne structures, we next calculate their mechanical strengths. A common way of expressing the mechanical properties of two dimensional materials is to calculate their in-plane stiffness, Poisson's ratio and Young's modulus values. For this purpose, we used a rectangular unit cell in the xy plane and applied tension in both x and y directions, as shown in Fig. 8.4(a). We varied the lattice constants, a_x and a_y, between $\pm 0.03\%$ of the optimized values and calculated the energy value for each grid point obtained. In the end, we have obtained energy values for 225 grid points, which are plotted in Fig. 8.4(b). The strain energy E_s, at each point is calculated by subtracting the total energy at that point from the equilibrium total energy. It has been shown that this method of calculating the strain energy gives accurate results for graphene, and 6-6-12 graphyne.[115, 116, 117] The in-plane stiffness, which is commonly used measure of strength for 2D materials can be expressed as

$$C = \frac{1}{A_o} \times \frac{\partial^2 E_s}{\partial \epsilon^2} \tag{8.1}$$

where E_s is the strain energy, A_o is the equilibrium area and ϵ is the axial strain calculated by $\Delta a_{x,y}/a_{x,y}$, a being the lattice constant in the x or y direction.

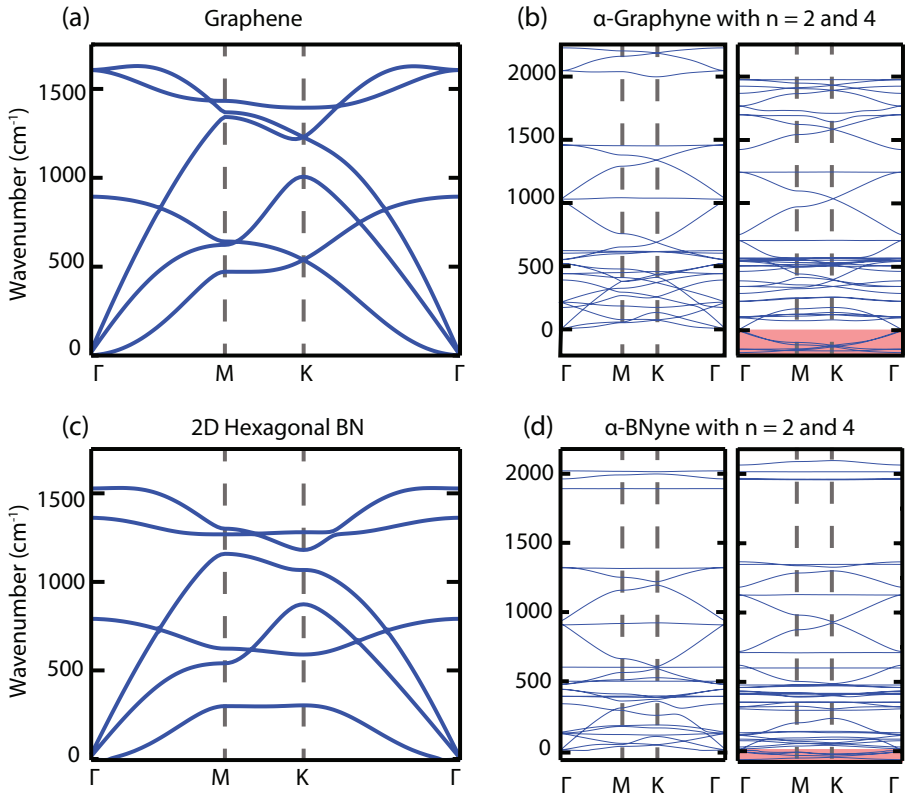

Figure 8.2: Calculated phonon bands. (a) Graphene. (b) α-Graphyne with $n = 2$ and 4. (c) Hexagonal BN. (d) α-BNyne with $n = 2$ and 4. The dispersion curves for n=2 have totally positive phonon modes which is an indication of their stability. On the other hand, n=4 cases have slightly negative modes, which are marked with the shaded regions and will be discussed in the text. Phonon bands of unstable structures, such as $n = 1$ and $n = 3$ are not shown.

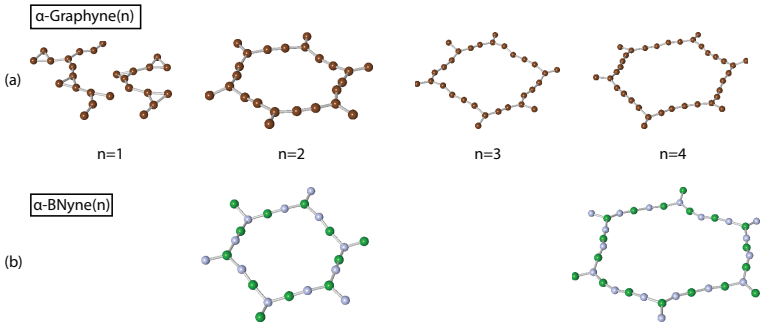

Figure 8.3: Snapshots of the MD simulations performed for $5ps$ at $T = 1000K$. (a) α-Graphyne(n). The structures are stable for $n = 2$ and $n = 4$, although buckled in the vertical plane. On the other hand, $n = 1$ case breaks into carbon atomic strings, and hence are totally unstable. α-Graphyne(3) undergos a structural transformation, whereby it acquires stability by changing the number of C atoms to $n = 2$ and $n = 4$ in the adjacent edges of hexagon. (b) α-BNyne(n). Both $n = 2$ and $n = 4$ cases remain stable during MD simulations. $n = 1$ and $n = 3$ cases are missed, since α-BNyne(n) cannot be formed with odd n.

The in-plane stiffness values of α-graphyne(2) and α-BNyne(2) were calculated as $21N/m$ and $19N/m$, respectively. These values are much lower than the in-plane stiffness of graphene, which is $\sim 340N/m$.[115, 49] As seen from these results, the implementation of new atoms between atoms at the corners of hexagons decreases the mechanical strength of graphene dramatically. The Poisson's ratio, which is defined as the ratio of the transverse strain to the axial strain, $\nu = -\epsilon_{trans}/\epsilon_{axial}$, was calculated as 0.88 and 0.89 for α-graphyne(2) and α-BNyne(2). By assuming an equivalent thickness with graphene, the Young's modulus values were calculated as $61GPa$ and $52GPa$ for these structures.

8.2 Electronic Structure

Earlier, Tongay *et al.*[98] showed that the electronic structure of α-graphyne(2) with two bands crossing the Fermi level at K-points of the BZ is similar to that of graphene. The presence of Dirac cones in the band structure α-graphynes, as well as $\beta-$graphyne and 6-6-12 graphyne have also been recently reported.[104] This showed that the existence of Dirac points and cones is not a unique property

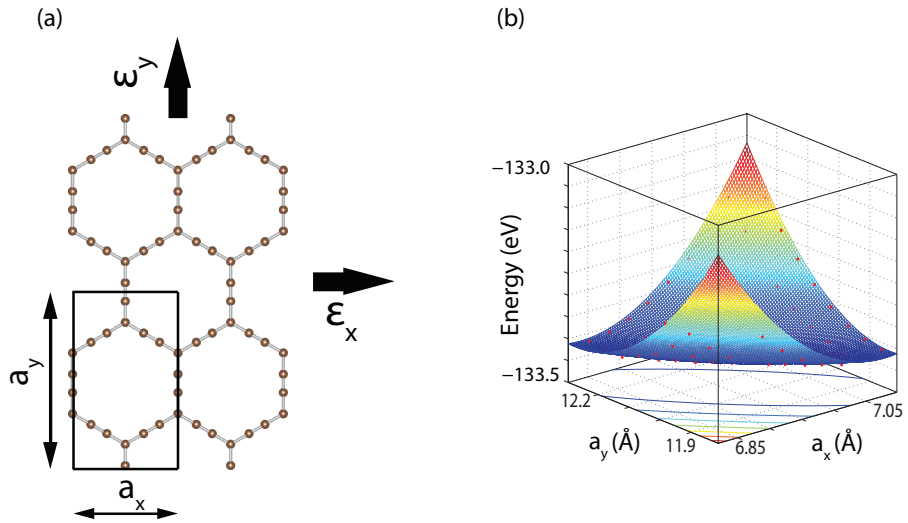

Figure 8.4: (a)$\alpha-$Graphyne(2) structure in rectangular unit cell with its lattice constants a_x and a_y. ϵ_x and ϵ_y are the strains in x and y directions, respectively. (b) 3D plot of the energy values corresponding to different a_x and a_y values.

of graphene. Earlier, the crossing of bands at the Fermi level and the formation of Dirac cones were also investigated for other structures.[118] It was pointed out that bare structures, large defects and adatoms on graphene can have Dirac cones if their periodic patterns comply with a specific symmetry. Here, we present the electronic energy band structure of $\alpha-$grapyhe(n) for $n = 1, 2, 3$ and 4 in Fig. 8.5. The existence of Dirac points is also seen here for all of these graphynes. Note that, the Dirac point lies on the Fermi level for the stable $n = 2$ and $n = 4$ structures, whereas it is shifted above from the Fermi level for the unstable $n = 1$ and $n = 3$. We note that high electron density at the Fermi level of $\alpha-$grapyhe(n) for n=1 and 3 can be attributed to their instability. On the other hand, reminiscent of the electronic structure of 2D single layer hexagonal BN, the band structures of α-BNyne(2) and α-BNyne(4) have wide band gaps as shown in Fig. 8.6. It can be seen that the band gap decreases with increasing values of n.

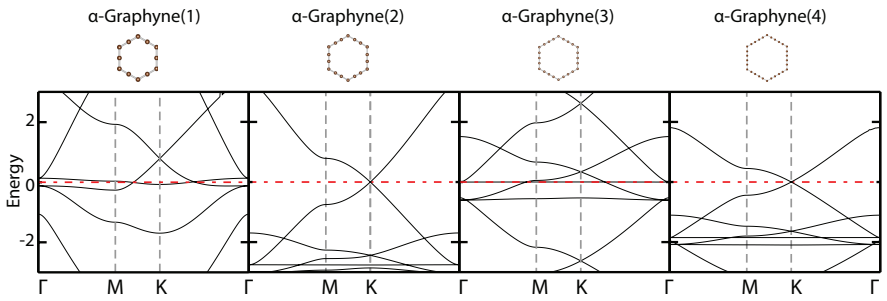

Figure 8.5: Electronic band structures of α-graphyne(n) for $n = 1, 2, 3$ and 4. All of the band structures contain Dirac points, while they are shifted above the Fermi level for $n = 1$ and 3. $n = 1$ and 3 cases also have Dirac points away from the high symmetry $K-$point. The zero of energy is set to the Fermi level.

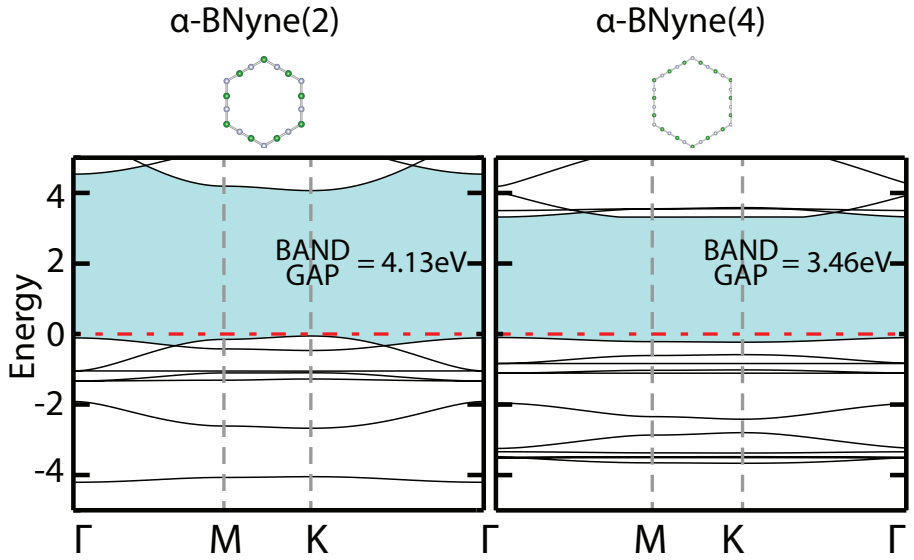

Figure 8.6: Electronic band structures of α-BNyne(n) for $n = 2$ and 4. Note that as n increases, the band gap decreases. The maximum energy of the valence band is set to zero.

8.3 Bilayer Structures

Here we address the question of whether α-graphyne and α-BNyne can form layered structures similar to graphite and hexagonal BN, or not. We place their bilayers as shown in figure Fig. 8.7 and explore equilibrium geometries, binding energies and electronic structures. We begin the analysis by placing two single layers of α-graphyne(2) sheets on top of each other at AA (*i.e.* hexagons in both layers face each other) and AB (*i.e.* first layer is shifted laterally to the centers of hexagons in the second layer) stacking geometries. We alter the interlayer distances until we achieve the energy minima. The calculated minimum energy geometries indicate that AB type of stacking is more favorable than AA type by $46meV$. This is a behavior similar to bilayer graphene structure or graphite. The optimized interlayer distance is calculated as 3.12Å, which is less than the interlayer distance of graphite, 3.35Å. This is mainly related to the less dense arrangement of carbon atoms on the graphyne surface as compared to the graphene, which results in lower surface energy and hence closer equilibrium distance. Similar results were also found in a previous interlayer distance studies made on different graphyne allotropes.[116]

A convenient procedure for calculating the interlayer binding energy for layered structures is subtracting the minimum energy of the layered structure from the sum of energies of separated layers.[119] Applying this method, we calculate the binding energy of bilayer α-graphyne(2) as $220meV$. We repeat the same analysis for bilayer α-BNyne(2), which also has an AB type double layer geometry as shown in the second column of Fig. 8.7(a). For this case, the energy difference between AB stacking and the AA stacking is in favor of AB by $70meV$, the interlayer distance is 2.9Å and the binding energy is $128meV$. The variations of total energies around the minimum energy values as a function of the interlayer distances are shown in Fig. 8.7(b).

We finally calculate the electronic structures of these double layered structures. The band structure of bilayer α-graphyne(2) is shown in Fig. 8.7(c). Note that, the bands are split due to the couplings between layers and the numbers of energy bands are doubled as compared to the single α-graphyne(2) sheet. Notably, the bands are no longer linear around the $K-$point, but parabolic. This kind of structure is reminiscent of the electronic structure of bilayer graphene or

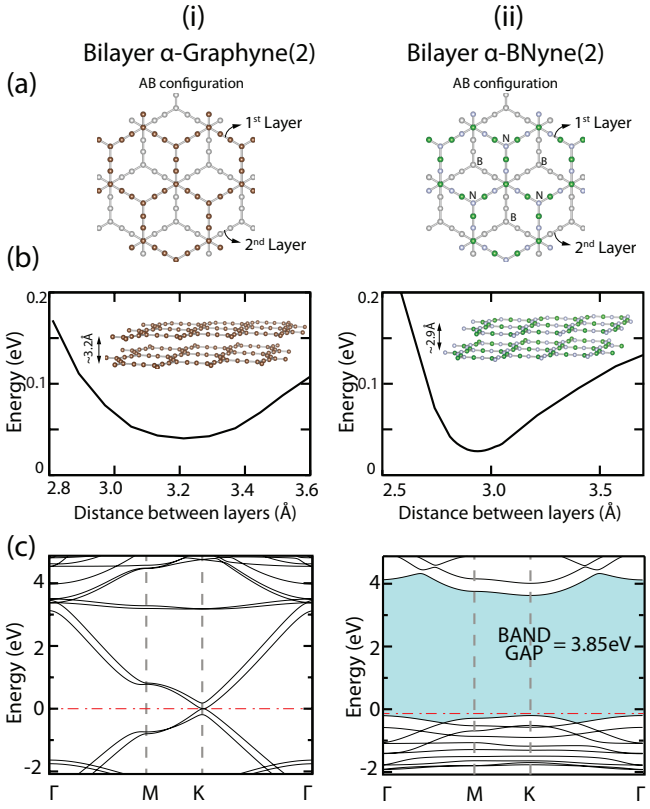

Figure 8.7: Bilayer α-graphyne(2) and its BN analogue bilayer α-BNyne(2) are shown in columns i and ii, respectively. (a) Top view of the optimized two layer structures. Both bilayer α-graphyne and α-BNyne have AB type of stacking geometry, which is more favorable than the AA stacking. In the ball and stick model B and N atoms are represented by green and blue balls and the all of the atoms in the bottom layer are shown in gray. (b) Variation of energy as a function of the layer-layer distance. (c) Electronic band structures of α-graphyne(2) and α-BNyne(2).

graphite.[120] As opposed to single layer, the bands no longer touch at the K point but there is a small band gap of $10meV$. The electronic structure for the bilayer α-BNyne(2) is also presented in Fig. 8.7(c). Similar to the single layer, the double layered structure also has a wide band gap.

8.4 Summary

In this chapter we introduce a new two dimensional allotrope of carbon atoms which forms when short carbon atomic chains are joined on the same plane. Here we show stabilities of α-graphynes and their boron nitride analogues(α-BNyne), which are considered as competitors of graphene and two-dimensional hexagonal BN. Based on first-principles plane wave method, we investigated the stability and structural transformations of these materials at different sizes using phonon dispersion calculations and ab-initio finite temperature, molecular dynamics simulations. Depending on the number of additional atoms in the edges between the corner atoms of the hexagons, n, both α-graphyne(n) and α-BNyne(n) are stable for even n, but unstable for odd n. α-graphyne(3) undergoes a structural transformation, where the symmetry of hexagons is broken. We present the structure optimized cohesive energies, electronic, magnetic and mechanical properties of stable structures. Our calculations reveal the existence of Dirac cones in the electronic structures of α-graphynes of all sizes. We expect that these layered materials can function as frameworks in various chemical and electronic applications.

Chapter 9

Dumbbell Reconstruction in Silicene and Germanene

Although graphene and boron nitride based monolayer structures were the initial two dimensional materials, efforts were later devoted to finding new forms of monolayer structures similar to graphene. In this chapter, we focus on the modifications of new monolayer structures based on Group IV elements, their properties, and new phases emerging from their reconstructions from first principle studies.

Silicene and germanene are the two monolayer structures based on Group IV elements silicon and germanium, respectively. Free standing silicene and germanene, have been recently shown to be stable and presently they have been an active field of research with several challenges[93, 121, 122, 123, 124, 125, 126, 127, 128, 129, 130] They share several of the exceptional properties of graphene, such as the linearly crossing of π- and π^*-bands at the Fermi level,[131] the ambipolar effect and the family behavior observed in nanoribbons. Although the strong $\pi - \pi$ coupling ensures planar geometry of graphene, this coupling weakens in silicene. However, the endangered stability is regained by the rehybridization of $3s$ and $3p$ valence orbitals to four-fold sp^3-like bonds through the dehybridization of three-fold planar sp^2 bonds. This leads to the buckling of the planar honeycomb structure. Accordingly, single atomic plane of graphene is replaced by two atomic planes, which are split by a buckling and the alternating atoms

at the corners of the hexagons are located in different atomic planes. Advances in growth techniques have enabled the synthesis of some of these predicted single layer structures, in particular the growth of single and multilayer silicene on Ag(111) substrates[128, 129, 130] and the growth of germanene on Pt and Au substrates[132] were recently succeeded.

9.1 Silicene Dumbbell

A Si adatom, which is initially bonded to the T site, pushes down the Si atom underneath to form a dumbbell D structure.[133] This configuration occurs without any barrier and has the binding energy of E_b=3.96 eV for a single Si adatom forming a D-structure in each 4×4 supercell. Therefore, a single D structure is not a predetermined configuration; it can occur while Si adatom migrates on silicene. In Fig. 9.1 the atomic configuration of D structure is presented. Two Si atoms positioned at two ends of the dumbbell are specified as D_1 and D_2. The distance between the dumbbell atoms D_1 or D_2 and nearest silicene atoms (A, E and F), which are located in a horizontal plane is 2.41 Å. This is larger than the nearest Si-Si distance 2.28 Å in pristine silicene. The distance between D_1 and D_2 is relatively large and is 2.69 Å. We note that in our earlier work, it was found that carbon atom migrating on graphene can form also similar dumbbell structure, even if it is slightly less energetic relative to its B-site binding.[134]

The Mulliken analysis indicates that the depletion of electronic charge from each of D_1 and D_2 atoms is +0.22 electrons, which is transferred to nearest three Si atoms of silicene. This situation suggests that strong bonds with mixed covalent-ionic character[135] form between nearest silicene atoms (A, E and F) and each of the dumbbell atoms, D_1 or D_2. On the other hand the D_1 - D_2 bond is relatively weak. These arguments can be depicted from isosurfaces of the total charge density and the charge density contour plots presented in Fig. 9.1. Accordingly, each of A, E and F atoms are four-fold coordinated, and hence they mimic the bulk Si crystal by making four bonds with their nearest neighbors. Whereas D_1 and D_2 atoms are 3+1 coordinated, each of them makes three strong bonds with A, E and F, but are weakly bonded to each other. We note that having positively charged two Si atoms located above and below the Si planes of buckled silicene may attribute interesting functionalities, which may be monitored by the electric

field applied perpendicular to silicene. For example, positively charged surface of D+silicene is attracted by negatively charged surfaces or vice versa for positively charged surfaces. Additionally, the work function (or photoelectric threshold) of silicene increases upon its decoration with D.

It should be noted that the formation energies of both the pristine silicene and D+silicene are negative with respect to bulk Si in diamond structure. In spite of that, one free Si adatom at the close proximity of a D structure does not form any bond with D_1 or D_2 to nucleate a cluster or an atomic chain as carbon adatom does on graphene or boron nitride[136, 137] It rather moves to the third nearest neighbor and form another D structure. It appears that the D structure display a self-organizing character. The D structure occurs at the T sites of silicene; H-sites are unfavorable since Si adatom cannot form sixfold long bonds with Si atoms at the corners of the hexagon. The calculated energy landscape of the Si adatom is shown in Fig. 9.1. The minimum energy barrier for the migration of Si adatom is estimated to be 0.92 eV. Although this barrier is significant to hinder diffusion at room temperature, at high temperatures the D structure may display interesting dynamics in the course of the growth of silicene.

The fact that the binding energy of the D structure (E_b=3.96 eV) is slightly higher than the cohesive energy of a Si atom forming a pristine silicene (E_C=3.94 eV) brings about the question whether the D+silicene with diverse decoration of D can be energetically more favorable than bare silicene and may constitute its complex derivatives. To this end, we compare the cohesive energies of Si atoms in the D+silicene structures with diverse coverage values with that in the pristine silicene. The cohesive energy per Si atom in an $n \times n$ supercell comprising one single D structure is obtained from the energy difference between the energy of free Si atom $E_T[Si]$ and the total energy of the structure of one D per supercell divided by $2n^2$+1, namely $E_C[D] = E_T[Si] - E_T[D + silicene]/(2n^2+1)$. Similarly, the cohesive energy of Si atom in a $n \times n$ silicene supercell is $E_C^o = E_T[Si] - E_T[silicene]/2n^2$. Then, the positive values of the energy difference, $\Delta E_C = E_C - E_C^o$ indicates that D+silicene structure is more favorable. For the sake of comparison, the cohesive energy of single Si atom in bulk silicon is calculated with the same parameters to be 4.71 eV. The cohesive energy and relevant properties of D+silicene are calculated as a function of coverage and presented in Table 10.1.

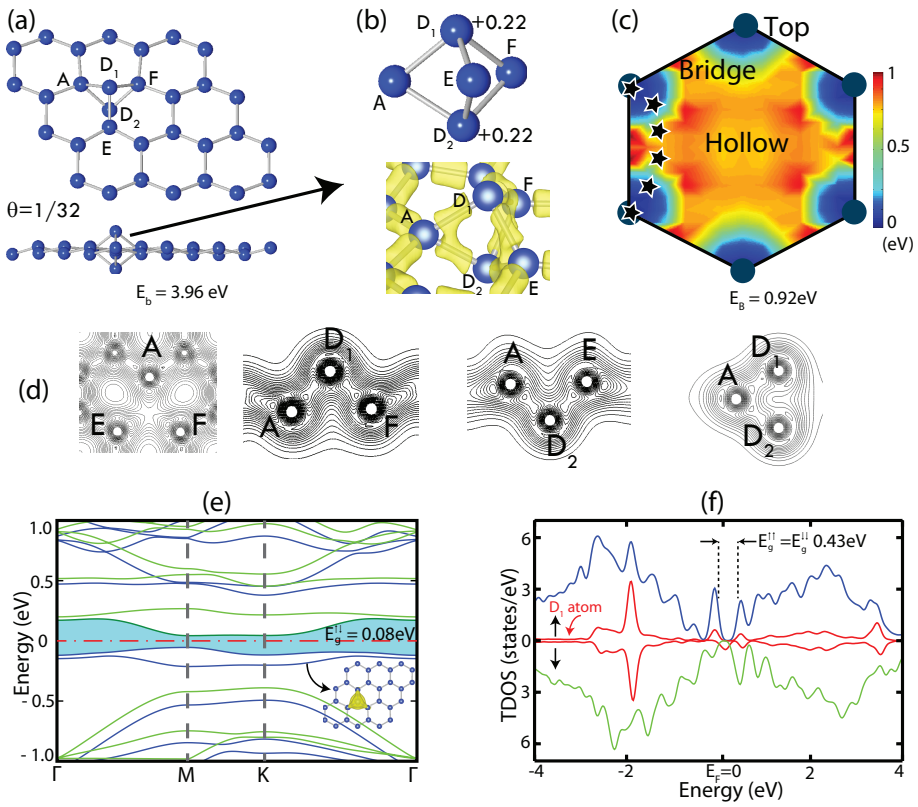

Figure 9.1: One Si adatom adsorbed to each (4x4) supercell of silicene, which corresponds to the uniform coverage of Θ=1/32. (a) Top and side views of the atomic configuration of the dumbbell (D) structure. Blue balls represent Si atoms. (b) Magnified view of the D structure together with the isosurface charge density. D_1 and D_2 denote Si atoms at both ends of the dumbbell; and A, E and F are silicene atoms nearest to D_1 and D_2. Excess charges on the Si atoms of the dumbbell structure are shown by numerals. (c) Energy landscape for the Si adatom on silicene calculated on a hexagon. The migration path of the Si adatom with minimum energy barrier E_B is indicated by stars. (d) Contour plot of the total charge density $\rho_T(\mathbf{r})$, on the horizontal plane passing through A, E and F atoms, and on the planes passing through A-D_1, A-D_2 and D_1 -D_2 bonds. (e) Energy band structure of the D+silicene structure with the dash-dotted line indicating the Fermi level. Blue(dark) and green(light) lines represent spin up and spin down states, respectively. The inset shows that the isosurface charge density of spin up states making the flat band just below the Fermi level is localized mainly at the D-structure. (f) Spin projected total density of states TDOS. Up-arrow and down-arrow stand for spin up and spin down states, respectively. The density of states DOS projected to D_1 is augmented four times and plotted in panel (f).

9.2 Coverage of Dumbbells on Silicene

The cohesive energy E_C of the D+silicene structure decreases with decreasing coverage. It is larger than the cohesive energy of Si atom in silicene and hence is slightly more favorable energetically than pristine silicene. For n=1 (Θ=1/2), the D+silicene structure has nonmagnetic ground state; it is metal and has high cohesive energy. Similarly, for a single D adsorbed to $\sqrt{3} \times \sqrt{3}$ supercell, which is predicted to be a nonmagnetic metal, ΔE_C=65 meV per Si atom is significant. Present results confirm the recent study,[138] which found that $\sqrt{3} \times \sqrt{3}$ coverage stable and has cohesive energy 48 meV per atom higher than that of pristine silicene. We believe that the difference between the calculated cohesive energies occurs from the van der Waals correction taken into account in the present study. For n=2 and n=3, ΔE_C decreases and continues to be nonmagnetic metal. However, for n=4, 5 and 7, D+silicene attains spin polarized ground state and achieve $\sim$2 μ_B magnetic moment per supercell. Hence, three of them are spin polarized semiconductor with a band gap $E_g^{\uparrow\downarrow} \sim$ 80 meV. For the case of n=4, the flat bands at the edges of valence and conduction bands in Fig. 9.1 (e) are derived from orbital states, which are localized at the D structure with also minor contributions from other Si atoms. Similar flat bands due to D structure also occur at -2 eV in the valence band as shown in the spin polarized DOS projected to D atoms presented in Fig. 9.1 (f).

For $\Theta \leq 1/32$ the spins are polarized and metallic states change into semiconductors. Also, ΔE_C is reduced and becomes smaller than the accuracy limits of present calculations. Apparently, various structures of D+silicene can be considered as the allotropes of the pristine silicene and display variations in the physical properties as a function of the coverage. The D structures forming uniform (1x1), ($\sqrt{3}$x$\sqrt{3}$), (2x2), (4x4), (5x5) and (7x7) supercells form centered hexagons of different sizes on silicene. On the other hand, two D structures contained in the ($\sqrt{3}$x$\sqrt{3}$) and (nxn) supercells with n=3,6,9,.. can form regular honeycomb structure and yield linearly crossing bands.

Finally, the question of whether the dumbbell Si atoms are active sites of silicene or not is investigated through the adsorption of Ti and H_2O to the dumbbell Si atoms. We found that similar to bare silicene H_2O did not form bonds with D_1 adatom. The increase of the binding energy relative to that on bare silicene

was only 130 meV. The binding energy of Ti atom to D_1 was almost half of the binding energy of Ti atom to bare silicene. We therefore arrive at the conclusion that the D structure of Si adatom gives rise to interesting electronic and magnetic properties, but it does not involve in active chemical reactions that are significantly different from bare silicene.

9.3 Germanene Dumbbell

A single Ge adatom adsorbed to germanene also constructs a dumbbell structure. Even more remarkable is that new phases can be constructed by the periodic coverage of germanene with DBs. Depending on the coverage of dumbbells, these stable phases can be metal or narrow band gap semiconductor in magnetic or nonmagnetic states and hence they attribute diverse functionalities to germanene.

In 9.2(a), we present various stages of conjugate gradient calculations taking place in the course of the adsorption of single Ge adatom. In the presence of an external and free Ge adatom, the formation of dumbbell structure on germanene is spontaneous. The external Ge adatom eventually moves closer to the germanene surface and makes a bridge bond with two underlying Ge atoms of germanene. It then starts to push the Ge atom underneath further down until the final dumbbell forms as shown in 9.2 (a). As a concerted process, two Ge atoms above and below the germanene surface, named as D_1 and D_2, donate significant electronic charge to the three nearest Ge atoms of germanene and hence each forms three strong Ge-Ge bonds with a length of 2.58 Å. With these additional bonds with DB, these three Ge atoms of germanene become fourfold coordinated. D_1 and D_2 by themselves engage in a 3+1 coordination, since each has three nearest neighbor Ge atoms at a distance of 2.58 Å. Whereas the D_1 - D_2 distance of 2.80 Å is slightly larger. At the end, the resulting DB corresponds to a local minimum on the Born-Oppenheimer surface and remains stable. As for the DB decorated germanene, it is a structure between the fourfold coordinated cdGe and the three fold coordinated single layer, buckled germanene. Since moving a dumbbell from one place to another by breaking three Ge-Ge bonds involves an energy barrier, any pattern of DBs on germanene is expected to remain stable.

Since the construction of a single dumbbell is an exothermic process and hence

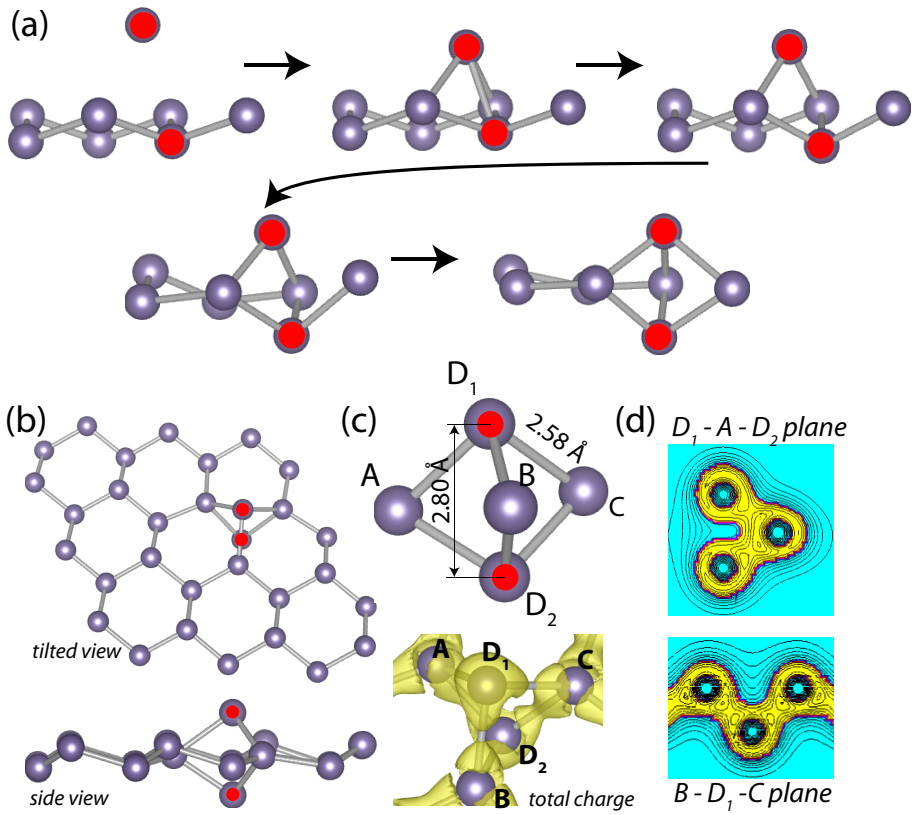

Figure 9.2: (a) Snapshots of conjugate gradient steps in the course of the formation of a dumbbell structure. The external Ge adatom first approaches to the germanene layer from the top site, and eventually constructs the dumbbell structure by pushing the host Ge atom down. (b) Top and side views of DB formed on (4×4) germanene. Two Ge atoms of dumbbell are highlighted by red. (c) The dumbbell zoomed in along with the total charge density isosurfaces. (d) Contour plots of the total charge density on planes passing through $D_1 - A - D_2$ and $B - D_2 - C$ atoms. Note that although the DB atoms make bonds with nearest germanene atoms, there is no bonding between the DB atoms, D_1 and D_2.

does not involve any energy barrier, the formation of DB structure is unavoidable as long as a free Ge adatom is present at the close proximity of the surface. We define the associated binding energy as $E_b = E_T[germanene] + E_T[Ge] - E_T[germanene + DB]$; in terms of the total energies of germanene+DB, pristine germanene and free Ge adatom. The binding energies are calculated for a single dumbbell in the $(n \times n)$ hexagonal supercells with varying values of n. Accordingly, E_b is the energy gained from the construction of a single dumbbell through the adsorption of a single Ge adatom to germanene and $E_b > 0$ indicates an exothermic process. For an isolated dumbbell calculated in a large supercell with n=8, $E_b \sim 3.4$ eV; but it increases with decreasing n or decreasing DB-DB distance due to the attractive interaction among DBs as discussed in the next paragraph. In 9.2 (b) and (c), the atomic configurations of a single dumbbell and its relevant structural parameters together with isosurfaces of charge density of Ge-Ge bonds around dumbbell are shown. The charge density counter plots calculated on various planes are presented in 9.2(d). The bonding of the dumbbell atoms (D_1 and D_2) with the nearest Ge atoms of germanene are clearly seen. Notably, there is no bonding between D_1 and D_2.

The D-B interaction on the surface of germanene is crucial for the growth of germanene phases. While an attractive interaction between two Ds can lead to the domain structure, a repulsive interaction at small D-D distance d is expected to favor phases with uniform coverage of dumbbell. Therefore, we next investigate what happens if a Ge adatom is introduced in addition to an existing dumbbell. Our calculations show that rather than bonding to D_1 or D_2 dumbbell atoms and forming a short Ge-Ge chain on top of them, Ge adatom migrates on germanene substrate and forms another D. Hence, each Ge adatom introduced to the surface of germanene favors the construction of a new dumbbell, as long as a proper position is available. The D-D coupling is calculated by placing two dumbbells in an (8×8) supercell; one at a fixed corner, and the second one placed at different sites on the supercell as described in 9.3. For each lateral position of the second dumbbell, the coordinates of rest of the atoms including the height of the second dumbbell are fully optimized. Apparently, an attractive interaction is set even for the large D-D distance. The dumbbells tend to be close to each other and hence to form domains. However, as long as germanene continues to be fed by Ge adatoms, domains join to form full coverage. Here one distinguishes two classes of sites for the second dumbbell: One class of sites is the high buckled sites of germanene, the other class is the low buckled sites. It should be noted

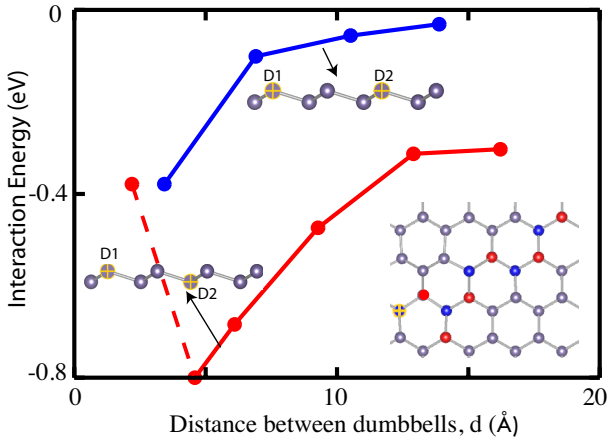

Figure 9.3: The interaction energy versus the distance between two DBs, d on the (8×8) supercell of germanene. The blue and red curves represent the variation of interaction energies for DBs formed on sites with the same and opposite bucklings, respectively. The interaction energy between two DBs situated at the same buckling is set to zero for large d. Negative energy indicates attractive interaction. One DB is permanently present on the yellow site and the second DB is placed on various positions shown by the blue and red marks in the inset. The attractive interaction energy falls suddenly when the second DB following the red path is situated at the nearest neighbor distance to the first DB.

that low and high buckled sites are equivalent if there is only one dumbbell due to the upside and downside symmetry. The site-specific variation of the total energy is shown in 9.3, where the interaction energy versus d curve follow different paths. Accordingly, the formation of two dumbbells on sites with opposite bucklings appears to be more favorable energetically, by ∼0.2-0.3 eV, since the gain of energy through the buckling of bare germanene is preserved. However, this difference of energy diminish as $d \to \infty$. Notably, it is not possible to create two DBs on the nearest neighbor sites of the lattice. This situation results in the constrained structure optimization in 9.3 (shown by the dashed line) as a sudden fall of the attractive interaction energy when the Ge adatom is placed at the first nearest neighbor of the existing dumbbells. The second dumbbell tends to move to the second nearest neighbor position when the constraints are lifted. If the second dumbbell is situated at the second nearest neighbor distance from the first dumbbell (where both dumbbells are situated on the sites of same buckling), Ge atoms of germanene at the first nearest neighbor distance to these two dumbbells become five fold coordinated.

Table 9.1: Calculated values for the various phases of germanene+DB, where DBs form periodically repeating supercells on germanene with 2D hexagonal or rectangular lattice. 2D Lattice: H hexagonal or R rectangular; Mesh: $(m \times n)$ cell in terms of the primitive hexagonal or rectangular unit cell of germanene; N: Number of Ge atoms (including DB) in each supercell; d: shortest distance between two DBs; A: the area of the supercell; μ: magnetic moment per supercell; ES: Electronic structure specified as metal M, or semiconductor with the band gap between valance and conduction bands calculated by GGA and HSE (for the spin polarized cases the gap between spin up - spin up and spin up - spin down bands are shown); E_b: Binding energy per Ge adatom relative to germanene or average binding energy if there is two DB in each cell; E_C: Cohesive energy (per atom) of Ge atom in Germanene+DB phase; E_C^s: Cohesive energy per area; ΔE_C: difference between the cohesive energies of a Ge atom in Germanene+DB and in pristine germanene, where positive values indicates that germanene+DB phase is favorable. For bare germanene E_C =3.39 eV/atom. TDP, HDP, RDP and DHP are described in the text.

Lattice	Mesh	N	d(Å)	A(Å^2)	$\mu(\mu_B)$	ES_{GGA} (eV)	ES_{HSE} (eV)	E_b (eV)	E_C (eV)	E_C^s	ΔE_C (eV)
H/FDP	1×1	3	3.77	12.34	0	M	M	4.00	3.60	0.873	0.204
R/RDP	1×1	5	3.39	24.21	0	M	M	3.73	3.46	0.715	0.069
H/TDP	$\sqrt{3} \times \sqrt{3}$	7	6.84	40.57	0	M	M	3.75	3.44	0.595	0.052
H/HDP	$\sqrt{3} \times \sqrt{3}$	8	3.85	38.60	0	0.53	0.73	4.03	3.55	0.736	0.160
H	2×2	9	7.79	52.54	0	0.16	0.32	3.72	3.43	0.585	0.037
H/DHP	2×2	10	4.50	52.54	0	M	0.46	4.39	3.59	0.680	0.198
H	3×3	19	11.68	118.22	0	0.29	0.63	3.54	3.40	0.551	0.008
H	4×4	33	16.06	223.36	2	0.42 / 0.06	0.77/0.44	3.44	3.39	0.495	0.002
R	2×1	9	6.95	48.43	0	M	M	3.85	3.48	0.189	0.189
H	5×5	51	19.87	342.05	2	0.33 / 0.03	0.61/0.36	3.40	3.39	0.510	0.000

9.4 New Phases of Germanene

In the case of uniform and periodic coverage, DBs form a mesh or periodically repeating supercells on germanene. The properties of the resulting germanene+DB phases depend on the size and geometry of supercells constructed from $(n \times n)$ hexagonal primitive unit cells or $(m \times n)$ rectangular unit cells of germanene, as well as the number of DBs in each supercell or the DB-DB distance, d. In 10.1, the energetics and the relevant data of the selected phases having 2D hexagonal or rectangular lattice structures are presented. The cohesive energy ($E_C = E_T[Ge] - E_T[germanene + D]/N$, which is the difference between the energy of one free Ge atom and the energy of germanene+DB phase per atom or simply the energy gained per atom by constructing a particular germanene+DB phase), and cohesive energy per unit area (i.e. $E_C^s = NE_C/A$) are relevant measures for energetics of the phases. In particular, E_C^s is a prime criterion which decides the phase that will grow on bare germanene. Here N is the total number of Ge atoms in the supercell of a given phase and A is the area of the supercell. Since each DB constructed on germanene lowers the energy, FDP (Full Dumbbell Phase) which corresponds to full coverage, attains the highest E_C, E_C^s and ΔE_C among other phases listed in Table 9.1. However, one Ge atom in each cell of FDP is forced to be six fold coordinated, and hence FDP is prone to structural instability. In fact, our ab-initio phonon calculations of this phase have branches with imaginary frequencies. Another structure, RDP (Rectangular Dumbbell Phase) in 10.1 is also found to be unstable based on ab-initio phonon calculations. DHP (Double Hexagonal Phase), where the hexagons of germanene are nested by large DB hexagons has the highest E_b and E_C among the other stable phases listed in 10.1. Additionally, two other phases, TDP (Trigonal Dumbbell Phase) and HDP (Hexagonal Dumbbell Phase) which have $(\sqrt{3} \times \sqrt{3})$ unitcells are of particular interest, since silicene grown on Ag(111) substrate also showed a $(\sqrt{3} \times \sqrt{3})$ pattern.[129] HDP has two DBs per cell, such that DBs are situated at the corners of hexagons to form a honeycomb pattern. It appears that HDP having the maximum cohesive energy per area, $E_C^s = 0.735$ eV/Å^2 among the other stable phases listed in 10.1 is energetically the most favorable structure to grow on bare germanene.

The germanene+DB phases acquire permanent magnetic moments when $d >\sim$ 15 Å, where the DB-DB coupling recedes and the DB behaves as a local defect

on the germanene substrate with a total magnetic moment of $2\mu_B$ per cell. We performed additional tests to understand the magnetic order of the system. To this extend, four DB structures were created on an (8×8) supercell and the ferromagnetic, antiferromagnetic and paramagnetic states were investigated. For the ferromagnetic case, all DB atoms were given an initial spin in the same direction; for the anti-ferromagnetic case opposite spins were assigned to the adjacent dumbbells. Our results showed that the ferromagnetic ordering has the lowest total energy indicating that it is the most favorable configuration.

The energy difference between the ferromagnetic state and the antiferromagnetic state is 0.63 eV per supercell. Notably, upon the relaxation of magnetic states, the final magnetic state of the structure is found to be always ferromagnetic no matter what the initial direction of spins were. The energetics of various germanene+DB phases display interesting trends: In general, the cohesive energy increases with increasing DB coverage, which confirms the situation in 9.3. The binding energies, E_b, also show the same trend except for DHP. The energy values presented in 10.1 imply that the higher the DB coverage of a phase is, the higher its total energy gets.

Dumbbells also modify the physical properties of germanene. In particular, the electronic and magnetic properties of pristine germanene show dramatic changes depending on the coverage (see also 10.1). Firstly, the spin-orbit coupling gives rise to significant splitting in the bands of germanene-DB phases. For example, the degenerate bands at the top of the valance band of (4×4) mesh split by 12 meV. Normally, germamene+DB phases maintain their metallic state at high coverage, but they transform into semiconductor as the size of their cell(n) or the DB-DB distance(d) increases; with the exception of HDP. In 9.4 we present the energy band structures of four different germanene+DB phases having hexagonal lattice. These are (i) TDP; (ii) HDP; (iii) DHP and (iv) triangular structure, where DBs form (4×4) mesh on germanene. It should be noted that the band gaps of the semiconductor phases are almost doubled after the HSE corrections. The dramatic effects of DB coverage is clearly seen in these band structures. While TDP is a nonmagnetic metal, HDP is a nonmagnetic semiconductor with an indirect band gap of 0.53 eV. DHP, which is a metal according to GGA, becomes a narrow band gap semiconductor after HSE06 correction. The (4×4) mesh of DBs is a magnetic, narrow band gap semiconductor. DB gives rise to localized states at $\sim$ -2 eV and -7 eV below the Fermi level.

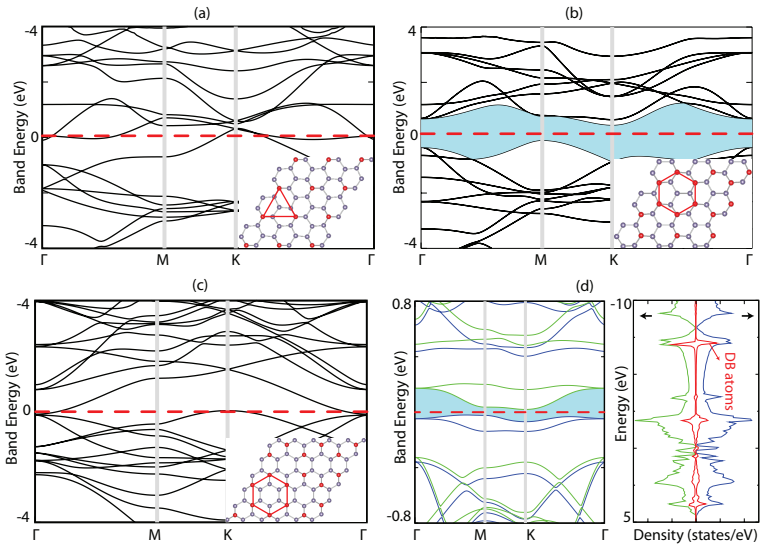

Figure 9.4: Electronic band structures of different phases of germanene. (a) TDP. (b) HDP. (c) DHP. (d) The triangular structure with DBs forming hexagonal (4×4) supercells, where the total density of states are also shown. The spin up and spin down bands are shown in blue and green lines, respectively. The density of states projected to the DB atoms shown in red and are augmented three times for a better view.

Incidentally, further to Ge DB on germanene, Si adatoms on germanene can also construct asymmetric DB structures, as such that D_1 = Si, but D_2 = Ge. The formation of this asymmetric DB is also exothermic and occurs spontaneously as long as a Si adatom on germanene is available. These asymmetric DB, as well as their periodic structures on germanene exhibit properties different from host DBs and multiply the functionality of DB based new phases of germanene. For example, the Si-Ge asymmetric dumbbell structure having hexagonal lattice over the (4×4) supercell of germanene is a nonmagnetic metal with a binding energy, E_b=3.86 eV per DB. In contrast, the symmetric germanene-DB having the same lattice is a magnetic semiconductor, and E_b=3.44 eV as shown in 10.1. We note that like the Si-Ge asymmetric dimer on germanene, also Ge-Si asymmetric dimer can be constructed on silicene spontaneously.

Chapter 10

New Material Predictions: Silicatene, Nitrogene and Antimonene

Trends in materials science have aimed at the discovery of single layer structures and their multilayer composites by using advanced fabrication techniques and/or quantum mechanical calculation. In this endeavor, single layer honeycomb like structures with novel functionalities have been predicted using Group-IV elements as discussed in the previous chapter. In this chapter, we discuss the formation of another two dimensional material which is based on the oxygenation of silicene. The new structure, which we name as silicatene, has a honeycomb-like two dimensional structure but its bonds and angles reorient to gain stability as discussed in the following sections.

In addition to Group IV elements, recently the fabrication of field effect transistor using micrometer sized flakes consisting of two-three layers of black phosphorus [139] and theoretical analysis [140, 141] revealing the stability of its single layer allotropes also brought Group V elements into the focus. Thus the idea of whether Group V elements can form single layer structures became a critical question to be answered. In the final two sections of this chapter we present the results of our analysis for two dimensional allotropes of nitrogen and antimony. The conclusion of our analysis has been positive and revealed that nitrogen and

antimony can also form 2D crystalline structures like silicene or phosphorene.

10.1 Silicatene

Silicene surface is rather reactive; oxygen molecule can be dissociated on silicene surface, whereby constituent oxygen atoms are bonded to the bridge sites with a strong binding energy of 6.17 eV. Incidentally, this bridge bonded O adatom can forcibly switch between two bistable equilibrium position at either sides as shown in Fig. 10.1 (a), if an energy barrier of 0.28 eV is overcame. At the transition state, the Si-Si bond is stretched to accommodate one O atom near its center and hence to form a Si-O-Si bond. Then, one may contemplate whether an exothermic process can take place, in which one O atom is inserted to each Si-Si bond concomitantly to grow a single layer honeycomb like network in 2D with the formula unit of Si_2O_3. Actually, similar process is realized in 3D through the oxidation of silicon surfaces to generate amorphous SiO_2. In various fourfold coordinated allotropes of SiO_2, such as cristobalite, quartz, tridymite etc, which are commonly named as silica, each Si atom has four nearest neighbor oxygen atoms, while each O atom being bonded to two Si atoms at both end is twofold coordinated. It is characteristics of several allotropes that Si-O-Si bond is bent around O atom. Notably, β-cristobalite, well-known insulating, high temperature phase of silica has straight bonds and it can be viewed as if an expanded diamond crystal of silicon, where tetrahedrally bonded Si-Si bonds have changed to straight Si-O-Si bonds by inserting O atoms at their centers. However, none of those allotropes of silica has a graphite like structure.

If a single layer honeycomb like network of silica were formed in 2D, there remain three important questions to be addressed for this ideational situation: (i) Is the single layer silica structure stable in 2D? (ii) What are the physical and chemical properties of this structure? (iii) Can honeycomb like silica structure be synthesized? Here rigorous answers are provided for the first two questions based on predictions obtained from first-principles calculations. Our results will possibly guide future efforts for the synthesis of single layer silica. Notably, theoretical predictions obtained from first-principles calculations have offered valuable input for the design of modern materials.

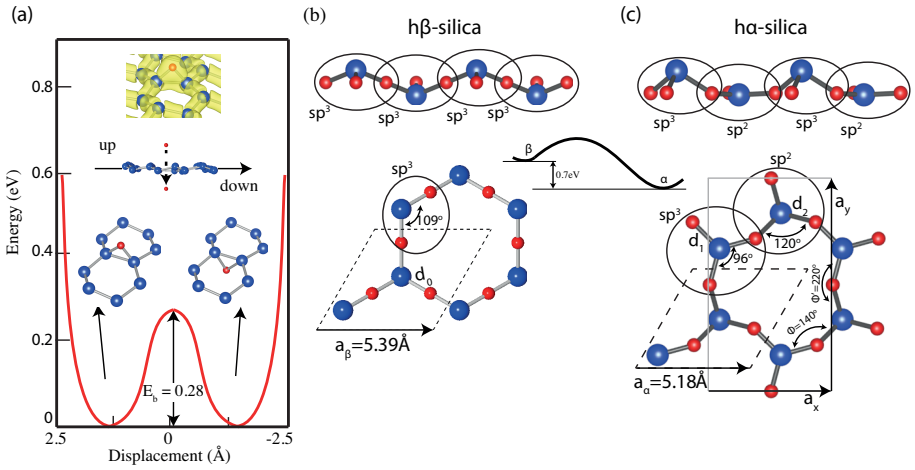

Figure 10.1: Monolayer silica (a) As shown by inset, equilibrium charge density isosurfaces of oxygen adatom adsorbed to the bridge site of silicene indicates a significant amount of effective charge. Variation of total energy of oxygen and silicene system as the oxygen adatom is passing from the top to the bottom side through the minimum energy path. The energy barrier involved in this excursion is only 0.28 eV. Large-blue and small-red balls stand for Si and O atoms, respectively. (b) Side and top view of hβ-silica, the precursor of the single layer silica, has straight Si-O-Si bonds as if one O atom is inserted at the center of each Si-Si bond of silicene. While Si atoms are alternatingly buckled to different planes, oxygen atoms lie in the same plane in between. (c) The structure of stable, single layer hα-silica, which has 0.7 eV lower energy as described schematically. Two dimensional hexagonal primitive and rectangular unit cells are delineated by black (dashed) and gray (continuous) lines. The corresponding lattice constants are a_β and a_α, respectively. Two types of Si atoms, i.e. those up-buckled and forming the sp^3-bonding with 96^o O-Si-O bond angle and those lying in the same plane of oxygen atoms and forming the planar sp^2-bonding with 120^o O-Si-O bond angle, are ordered alternatingly at the corners of a hexagon.

A hexagonal unitcell including two Si and three O atoms forms a regular honeycomb network, as shown in Fig. 10.1 (b). This structure, which is named as hβ-silica (h denoting the single layer hexagonal lattice) in analogy to β-cristobalite in 3D, corresponds to a shallow local minimum. When perturbed from perfect symmetry and subsequently relaxed by conjugate gradient method using stringent convergence criteria, the structure eventually transforms to the new structure, hα-silica, as described in Fig. 10.1 (c). At the end, the energy is lowered by 0.7 eV and the regular hexagons are distorted keeping the honeycomb like network in the top view, where Si atoms are placed at the corners of hexagons, but they are buckled like silicene. These rearrangements starting from regular hβ-silica are reminiscent of the transition from ideal β-cristobalite to α-quartz in 3D. In the present 2D case, the O-Si-O angles are alternatingly 120^o and 96^o, whereby three alternating Si atoms of a hexagon engage in planar sp^2-like and the remaining three rise upwards and form tetrahedral sp^3-like hybrid bonds. Consequently, the rotary reflection symmetry is broken. Incidentally, the lattice constant is reduced from 5.39 Å to 5.18 Å and the straight Si-O-Si bonds are bent such that all oxygen atoms remain in the same plane together with sp^2-bonded Si atoms. However, from the symmetry point of view it is equally probable that sp^3-bonded Si can be either at the top side or the bottom side of the plane of oxygen and sp^2-bonded Si atoms, which implies frustration and leads to domain structures. The Si-O-Si angles between sp^2-bonded and sp^3-bonded Si atoms, which are denoted by ϕ for oxygen protruding outwards and by ϕ' for oxygen atoms protruding inwards in the same hexagon like cell, are 140^o and 220^o, respectively. Details of this complex atomic structure and other physical properties of the optimized hα-silica are summarized in Table 10.1. Its high cohesive energy, E_c=28.6 eV per unit cell originates from mixed (covalent and ionic) bonds between Si and O atoms; high formation energy prevents it from clustering.

10.1.1 Stability

To ascertain that the optimized structure of hα-silica is stable rigorous tests are performed. First, similar structure optimizations are repeated also using a (4x4) supercell to circumvent the constraints, which may be imposed by using primitive unit cell. In these tests, no periodic reconstructions involving multiple primitive

Table 10.1: Calculated lattice parameters of hα-silica and its relevant physical properties. a_α: hexagonal lattice constant in Å; d_1: Si-O bond distance of sp^3-bonded Si in Å; d_2: same for sp^2-bonded Si; E_c: the cohesive energy per unit cell in eV; E_f: the formation energy per unit cell in eV; E_{G-gga}: the band gap calculated by GGA with van der Waals correction in eV; E_{G-hse}: the band gap calculated by HSE; C: the in-plane stiffness in N/m; ν: Poisson ratio ; Q^*_O, $Q^*_{Si-sp^3}$, $Q^*_{Si-sp^2}$: Mulliken charges in electrons for different atoms.

a_α	d_1	d_2	E_c	E_f	E_{G-gga}	E_{G-hse}	C	ν	Q_O	Q_{Si-sp^3}	Q_{Si-sp^2}
5.18	1.76	1.58	28.6	9.2	2.2	3.3	22.6	-0.21	-0.31	0.53	0.39

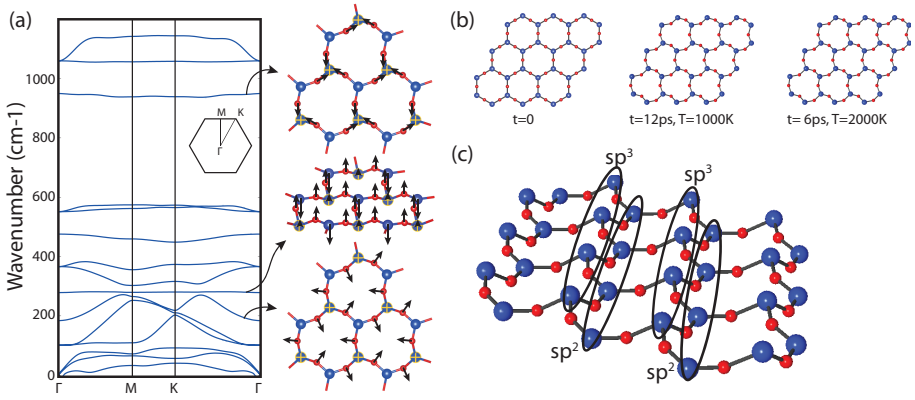

Figure 10.2: (a) Phonon frequencies and their dispersions along the symmetry directions of the Brillouin zone. Specific modes of phonons involving the vibration of oxygen atoms indicated by small arrows are also described. (b) Results of ab-initio molecular dynamics calculations performed at 1000 K and 2000 K starting from the regular hβ-silica structure and ending at hα-silica. (c) The atomic structure of hα-silica with large-blue and small-red ball standing for Si and O atoms, respectively. Silicon atoms, which are sp^3-bonded (up-buckled) and those sp^2-bonded (in the plane of oxygen atoms) are highlighted.

cells were observed. Also, specific atoms are displaced forcibly from their optimized equilibrium positions corresponding to a minimum in Born-Oppenheimer surface. The optimized structure was resistant to these large scale deformations and hence restored itself quickly demonstrating that the structure of hα-silica is robust. Furthermore, the frequencies of phonon modes are calculated in the first Brillouin zone with extreme accuracy and all are found to be positive. The dispersion relations of calculated phonon frequencies, $\Omega(\mathbf{k})$, with a minute gap between optical and acoustical modes as shown in Fig 10.2, demonstrate that in fact hα-silica remains stable as its size increases ($D \rightarrow \infty$). Otherwise, the specific eigenfrequencies of the dynamical matrix would be imaginary, if any instability due to the long wavelength transversal acoustical phonons were imposed to hα-silica. The stability of hα-silica is further investigated by performing ab-initio, molecular dynamics (MD) calculations at very high temperature. Starting from regular hβ-silica, we first excite the structure to 1000 K; the structure has transformed to hα-silica and did not change in the course of MD simulations lasting 12 ps as shown in Fig. 10.2 (b). Subsequently, we repeated the same simulations for 6 ps by raising the temperature of hβ-silica suddenly from 0 K to 2000K. No instability leading to structural transformation or dissociation of hα-silica was observed even if the specific phonon modes were softened at such a high temperature.

Our conclusions on the mechanical stability and strength of hα-silica is corroborated further by calculating its in-plane stiffness, $C = A_o^{-1}\partial^2 E_T/\partial\epsilon^2$ (in terms of the area A_o of the cell and the variation of total energy, E_T with strain, ϵ). Owing to ambiguities in defining the Young's modulus, the in-plane stiffness C is used to characterize the strength of single layer structures. Here calculations can conveniently be performed in rectangular cell by applying uniaxial strain along x- and y-directions to deduce that $C_x \simeq C_y$ =22.6 J/m^2. The calculated in-plane stiffness is smaller than that of graphene.

The Poisson's ratio $\nu = -\epsilon_y/\epsilon_x$, i.e. the ratio of the transverse strain to the strain induced by the uniaxial tensile stress is calculated as -0.21. This is remarkable in the sense that as hα-silica is stretched along x-direction it also expands in the y-direction. Hence, hα-silica is a negative Poisson's ratio material owing to its squeezed structure consisting of twisted and bent Si-O-Si bonds; three oxygen atoms in each hexagon protrude inward the hexagon with $\phi^{'}$=220^o resulting in re-entrant structure.

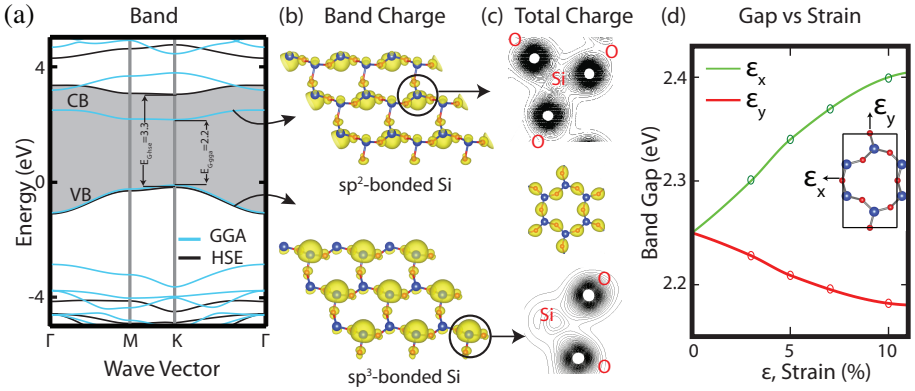

Figure 10.3: (a) The electronic band structure of hα-silica with direct band gap of E_{G-gga}=2.2 eV and E_{G-hse}=3.3 eV, which are calculated by GGA+vdW and HSE, respectively. The HSE band gap is shaded. The zero of energy is set to the top of the valance band. (b) Isosurface charge densities of the lowest conduction CB and highest valence VB band. (c) Contour plots of the total charge density in the plane of oxygen atoms passing through the sp^2-bonded Si atom and those in the O-Si-O plane passing through the sp^3-bonded Si atom. The sp^2-bonded Si atom has relatively higher charge density. Isosurfaces of the total charge density with isosurface value of 0.15 electrons/Å^3 show significant charge accumulation around oxygen atoms. d) Variation of the band gap as a function of the strain, ϵ applied in the x- and y-directions. The inset shows the rectangular unit cell and the directions of the uniaxial strains ϵ_x and ϵ_y.

10.1.2 Electronic Properties

Electronic and electromechanical properties of hα-silica are summarized in Fig. 10.3: It is a nonmagnetic, wide band gap semiconductor with a HSE corrected [83] direct band gap of E_{G-hse}=3.3 eV. As expected, the band gap predicted using GGA calculations,[58] E_{G-gga}=2.2 eV, is relatively smaller. While conduction and valance band edges are mainly derived from the dangling orbitals of sp^2-bonded and sp^3-bonded Si, respectively, the bands of oxygen-p orbitals occur below $\sim$-4 eV. It is a rather rare circumstance that the calculated band gap of hα-silica increases with increasing uniaxial strain, ϵ_x; but it decrease with increasing ϵ_y. Hence, the response of the electronic structure is different for uniaxial strains ϵ in different directions, since the displacement of oxygen atoms are direction dependent.

According to Mulliken charge analysis[21] Si-O bonds have a strong ionic character. Due to the special bond configuration, each oxygen atoms receives $\sim$0.31 excess electrons, while 0.53 electrons and 0.39 electrons are donated by sp^3- and sp^2-bonded Si atoms, respectively. The details of charge transfer are depicted by charge density isosurfaces and contour plots. Also, because of significant charge transfer between Si and O atoms, the dipole moments along x- and y-directions of the perpendicular unit cell are high and are P_x=13.1 eÅ and P_y=3.5 eÅ, respectively.

10.1.3 Nanoribbons

While an infinite structure subjected to the periodic boundary conditions is a theoretical abstraction, its finite size is used for various applications. In Fig. 10.4 we consider zigzag and armchair nanoribbon specified by the number of hexagons across their widths w, N_Z=4 and N_A=4 , respectively. Apart from the minute reconstruction at their edges, these nanoribbons are stable. The zigzag N_Z=4 nanoribbons is a metal, where the flat band at the Fermi level is derived from the orbitals of sp^2-bonded atoms located at one edge. Another band crossing the Fermi level has small dispersion and originates from the orbitals of sp^3-bonded Si atoms at the other edge. In contrast, the armchair nanoribbon is a semiconductor with a direct band gap of 1.9 eV calculated within GGA.[58] The bands at the

conduction and valance band edges are derived from the sp^2-bonded and sp^3-bonded Si atoms at both edges, respectively. Due to small coupling between edges the bands are slightly split. These nanoribbons with or without foreign adatoms attached to the edges and their networks consisting of the combination of zigzag and armchair nanoribbons with different N_Z and N_A, can display diversity of electronic properties, which is beyond the scope of the present study. Here we point out a property of hα-silica, which may be of potential importance. Due to the significant charge transfer between Si and O atoms and also its re-entrant structure a finite size flake of hα-silica is expected to be influenced by the applied electric field. Because of the induced divergences, the effect of the in-plane electric field, $\vec{E}$, is investigated on the armchair nanoribbons. As illustrated in Fig. 10.4 (b), applied in-plane electric field induces significant changes in the width Δw and Si-O-Si bond angle ϕ of armchair nanoribbons. The piezoelectric coefficient is estimated from Δw as 5.7x10^{-12} m/V, which is more than twice the value measured for quartz.[142] This is an important property, which is crucial for piezo devices.

It should be noted that hα-silica and its ribbons discussed so far are rather reactive due to dangling bonds or π-orbitals oozing from Si atoms. Thus, they can acquire new functionalities by adsorption of adatoms to Si, such as H, O, F, Cl etc. When oxidized through the saturation of these dangling and π-orbitals alternatingly from the top and bottom sides, the structure attains further stability and increased inertness. Upon oxidation the filled band at the top of the valance band derived from Si-sp^3 dangling bonds and empty band at the bottom of the conduction band derived from Si-π orbital in Fig. 10.3 are removed and the band gap increases from 2.2 eV to $\sim$6 eV attributing a high insulating character like 3D silica. This way, Si atoms acquire the fourfold coordination of oxygen atoms as in 3D silica. While the hexagon like geometry in Fig. 10.1 is maintained, sp^2-bonded Si atoms change to sp^3-bonded Si atoms and hence restore the rotary reflection symmetry.

10.1.4 Bilayers and Functionalization

Two parallel, single layer hα-silica can form bilayer by lowering the total energy. By examining various, possible relative positions of two layers we determined

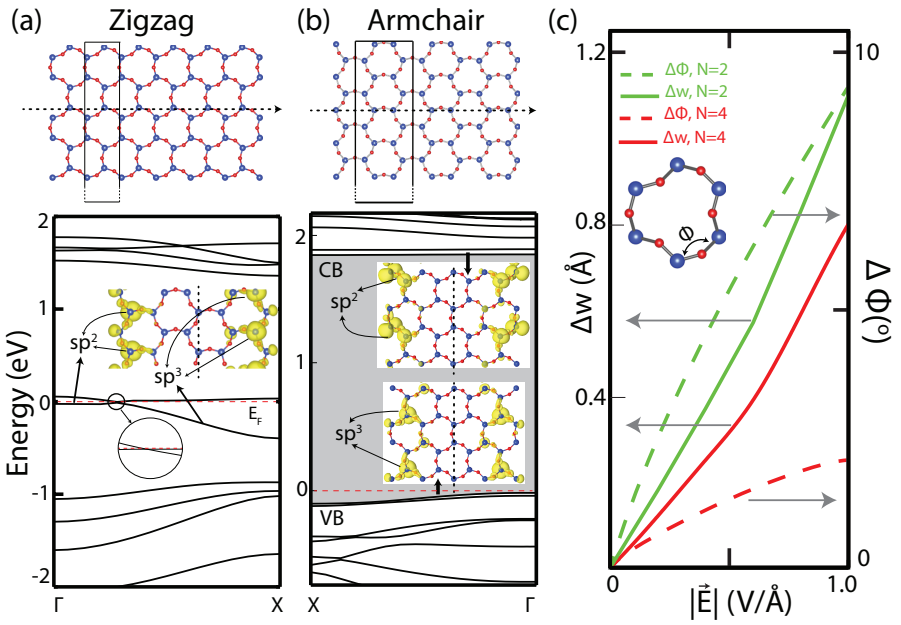

Figure 10.4: (a) Zigzag nanoribbon N_Z=4 and its electronic structure. The orbital characters of two bands crossing the Fermi level are shown by inset. The axis of the ribbons are indicated by dash-dotted lines ending with an arrow. (b) Armchair nanoribbon with N_A=4 and its electronic structure. The bands at the edges of valance VB and conduction CB bands originate from the edge states having sp^3- and sp^2- orbitals of Si atoms localized at both edges, respectively. The nanoribbon is a semiconductor with a gap of 1.9 eV. (c) Variation of the width of the armchair nanoribbon and $\Delta\phi$ under an in-plane electric field $\vec{E}$ perpendicular to the axis.

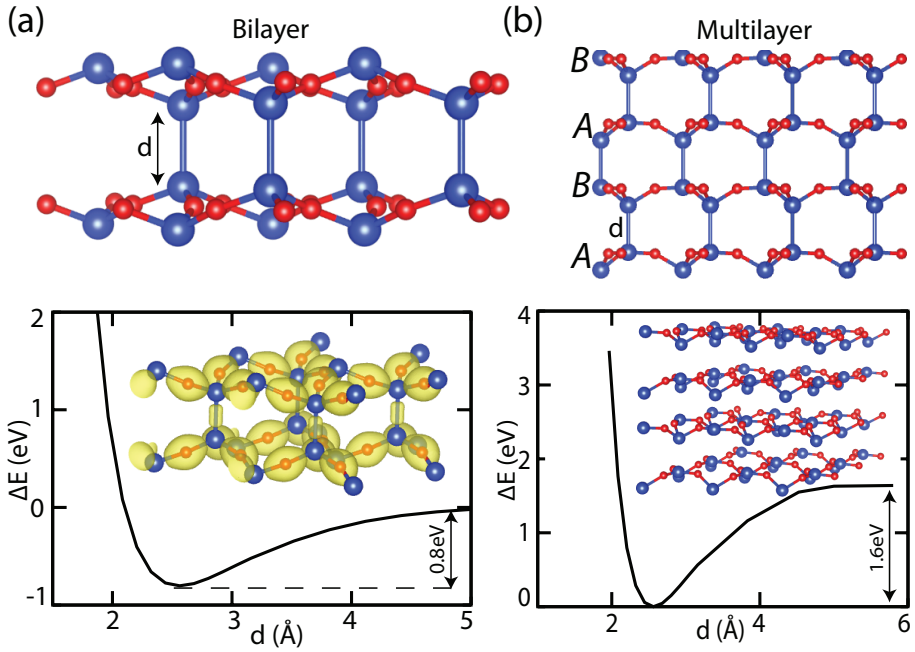

Figure 10.5: (a) Atomic structure of bilayer constructed from hα-silica layers together with variation of the total energy, ΔE with the distance d. (b) Atomic structure of multilayer constructed through the ABABA.. stacking of hα-silica layers together with the variation of the total energy with the interlayer distance d.

the optimized stacking of bilayer structure as presented Fig. 10.5 (a). From the calculation of the variation of the total energy with the layer distance, we infer that the energy of two hα-silica is lowered by 0.8 eV per unit cell upon the formation of bilayer. In equilibrium, the Si-Si bond between two silica layers is 2.53 Å. We note that in the bilayer three Si atoms forming planar sp^2 bonding are buckled for sp^3-type hybridization.

In Fig. 10.5 (b) the formation of multilayer silica through the ABABA.. stacking of single layer silica is presented. Upon the multilayer formation all Si atoms become identical by forming sp^3-type bonding.

The buckled honeycomb-like structure of silica resembles that of monolayer silicene and graphene. Of these, after the synthesis of graphene efforts were mainly devoted to modify its properties through chemical and physical treatments. Previously, absorbtion of foreign adatoms and creating a full coverage on

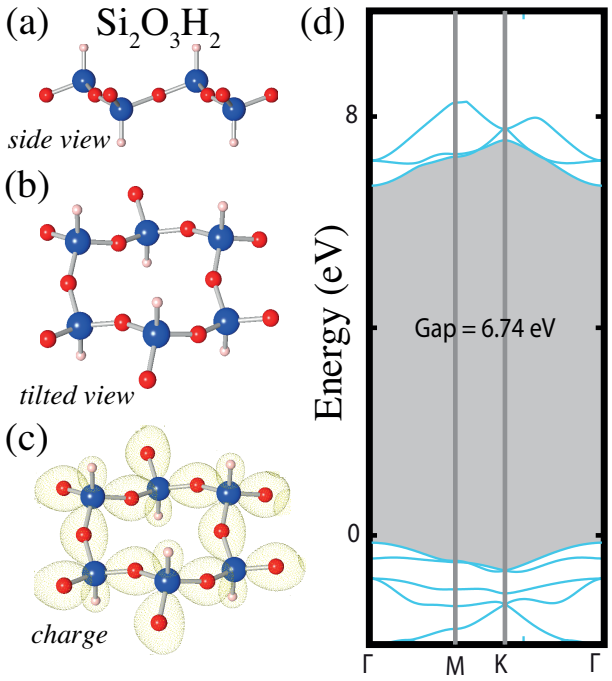

Figure 10.6: Hydrogenated hα-silica, $Si_2O_3H_2$. The side (a) and (b) the top views of atomic structure with the blue, red and the pink balls representing Si, O and H atoms, respectively. (c) The isosurfaces of the total charge distributions. (d) Electronic band structure with the band gap is shaded.

the monolayer structure with suitable elements has been effectively achieved for graphene. In this way, the hybridization of carbon atom in graphene transforms from sp^2 to sp^3, which eventually modifies the electronic properties of graphene. Such efforts had resulted in hydrogrenated graphene (graphane), fluorographene and grapheneoxide, which modify the gap and electronic structure and provide protective layers for the bare structure.

Having predicted the new silica structure whose details were fully investigated in the main text, we also followed a similar route with previous graphene studies to fully cover the bare silica with O, H, F and O adatoms, which result in $Si_2O_3H_2$, $Si_2O_3F_3$ and Si_2O_5, respectively. All of these coverages increase the band gap of the silica increases significantly upon coverage with H, F and O. In Fig. 10.6, Fig. 10.7 and Fig. 10.8 the atomic configurations, charge distributions and the electronic properties of these structures are presented.

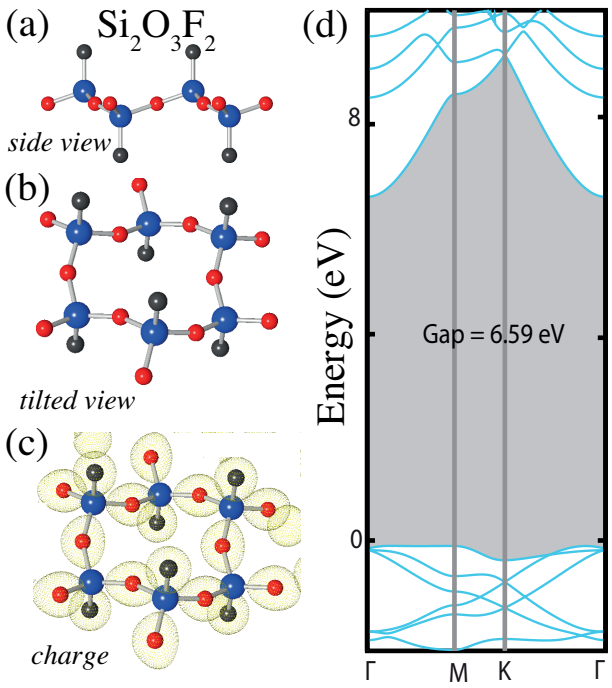

Figure 10.7: Same as Fig. 10.6, but for fluorinated hα-silica.

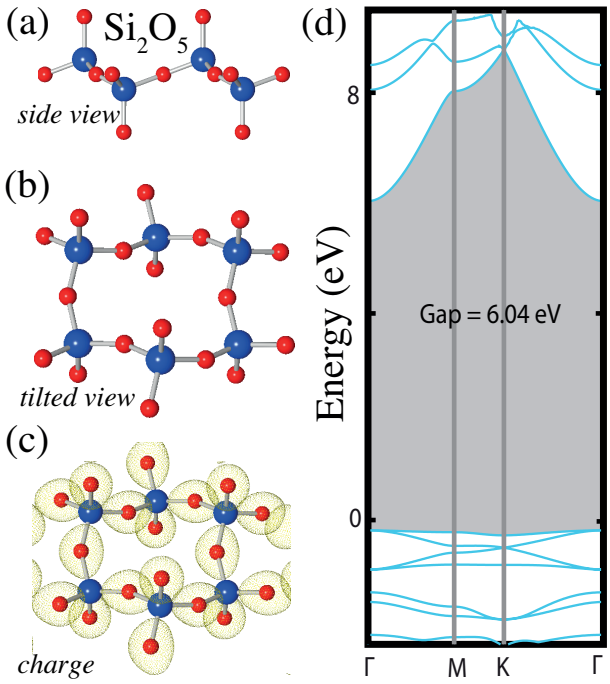

Figure 10.8: Same as Fig. 10.6, but for oxygenated hα-silica.

The additional atoms attach to the Si atoms which were previously bonded to three O atoms only. Hence, after the saturation of dangling Si orbitals, the coordination number of each Si raises to four, three of which are previous O atoms. In the bare silica, there exists two kinds of Si atoms in the unit cell: one in the same plane with the O atoms, which makes sp^2 bonds and the other one in a buckled position which makes sp^3-type bonds with the O atoms. Hence, sp^2 and sp^3-type bonds coexist in the bare monolayer structure. However, with the additional adatoms, both Si atoms arrange themselves so that they are geometrically identical to each other. Since the dangling Si orbitals are saturated, the band gap increases by ~ 4 eV. The newly formed structures, $Si_2O_3H_2$, $Si_2O_3F_3$ are stable under MD simulations performed for 5ps at 1000K. The MD simulations which were performed in enlarged 4×4 unitcell have further continued for 2ps at 2000K where Si_2O_5 undergoes a structural transformation at elevated temperature and forms silicatene as explained in the main text.

10.2 Nitrogene

We performed further theoretical analysis to exploit the idea of whether Group V elements can form single layer structures. The conclusion of our analysis has been positive and revealed that nitrogen can also form 2D crystalline structures like silicene or phosphorene. In particular, nitrogen has liquid phase at 77K; molecular/non-molecular solid phases[143, 144, 145, 146, 147, 148] and 3D cubic gauche(cg-N) crystalline phase[149, 150] but normally it is gaseous at room temperature. Here we show that nitrogene can also form crystalline phase with 2D hexagonal lattice in single-layer, buckled honeycomb structure, named as *nitrogene*. Notably, while N_2 molecule is triple bonded, nitrogene is constructed from threefold coordinated and single bonded N atoms similar to the 3D cg-N crystalline phase. We showed that nitrogene can remain stable above the room temperature and can form stable nanoribbons, bilayer and 3D graphitic structure named *nitrogenite*. However, unlike semi-metallic graphene or silicene having perfect electron-hole symmetry, nitrogene is a wide band gap insulator.

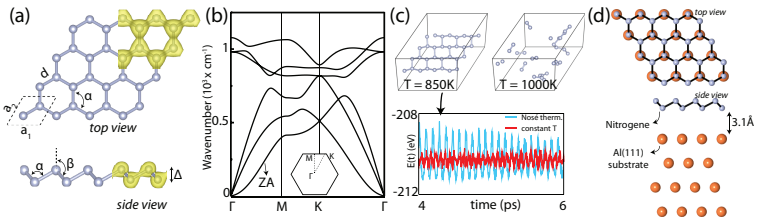

Figure 10.9: (a) 2D crystalline structure of nitrogene with optimized lattice constants $a_1 = a_2 = 2.27$Å, the buckling $\Delta = 0.7$Å, single bonded N-N distance $d = 1.49$Å, bond angles $\alpha = 99^o$ and $\beta = 118^o$. Bonding is depicted by isosurface of the total charge density. (b) Vibrational bands. (c) ab-initio MD snapshots of atomic structure at temperatures 850K and 1000K. Energy versus time plots calculated using the Nosé thermostat and constant temperature value are shown with blue and red lines, respectively. (d) Atomic configuration of nitrogene on Al(111) substrate. In the top view, only the Al atoms belonging to the top Al(111) surface are shown for clarity. N and Al atoms are shown by small blue and large orange balls, respectively.

10.2.1 Structures

Among different possible geometries, the washboard structure of black phosphorene [140], which we adapted to nitrogene underwent an instability in the course of structure optimization and dissociated into N_2 molecules. Planar honeycomb structure constructed from 2D hexagonal lattice with two nitrogen atoms in the primitive cell is buckled in the course of structure optimizations; while nitrogen atoms at three alternating corners of planar hexagon are displaced downwards, the other three raised upwards with a buckling distance of Δ=0.7 Å. Fully optimized nitrogene structure is described in Fig. 10.9. To avoid possible artifacts of single cell calculations, where reconstructions extending to few primitive cells can be hindered and thus the structure may fictitiously appear stable, we also optimized the structure using (4×4) supercell providing higher degrees of freedom; this ended with the same structure obtained from (1×1) single cell optimization. Nitrogene structure has a nonmagnetic ground state. In the buckled honeycomb structure, three $sp^{n\alpha}$ orbitals of nitrogene atoms having bond angle $\alpha = 99^o$ form covalent σ-bonds with three nearest N atoms and provide the strength of nitrogene. Remaining two electrons on each nitrogen form $sp^{n\beta}$ orbitals with relatively high p contribution, which ooze perpendicularly. They involve in π- and π^*-like bonds with nearest atoms and ensure the layer geometry constructed

from two parallel planes of nitrogen atoms. The single bonding of nitrogene is illustrated by the isosurfaces of the total charge density in Fig. 10.9(a). Since the optimized structure of nitrogene has a cohesive energy of E_C=3.67eV/atom, its formation energy relative to strong N_2 molecule is -1.33eV. Accordingly, nitrogene corresponds to a local minimum in the Born-Oppenheimer surface. Even if the structure optimizations using CG favors stability of free standing nitrogene, we perform further tests to assure that nitrogene is stable and can sustain application above the room temperature.

10.2.2 Stability

In order to verify the stability of nitrogene against small frequency acoustic vibrations and small transversal/longitudinal displacements in different directions, we calculate frequencies of vibrational modes using a fine graded **k**-point sampling. All calculated frequencies are positive ensuring the stability of nitrogene. The vibration bands along the symmetry directions of BZ are presented in Fig. 10.9(b). The optic branches are separated from acoustic branches, except at the K-point where one optical branch touches the acoustic one. Even if all acoustic and ZA branches with positive frequencies ensure stability, the optimized structure by itself may correspond to a local shallow minimum and hence it may turn to be unstable at a finite temperature. We clarified this critical situation by performing ab-initio MD calculations at 850K and 1000K. The stability is maintained at 850K for 6ps, but at 1000K the crystalline structure was dissociated into N_2 molecules as shown in Fig. 10.9(c). These MD calculations confirm at least the stability above the room temperature. Furthermore, we calculated in-plane stiffness to be C= 270 N/m^2, which indicates the strong covalency of N-N bonds in the buckled honeycomb structure. The calculated in-plane stiffness of nitrogene can be compared with those of graphene (330 N/m^2), h-BN (240 N/m^2), silicene (65 N/m^2) and MoS_2 (138 N/m^2), all having single layer honeycomb structure. Apparently, nitrogene marks an in-plane stiffness value, which is second highest among these nanostructures.

Finally we address the question whether the stability is endangered by vacancy defect, or by adsorption of single adatoms like H and O. We consider a single vacancy periodically repeating in a 5×5 supercell of nitrogene, where the coupling

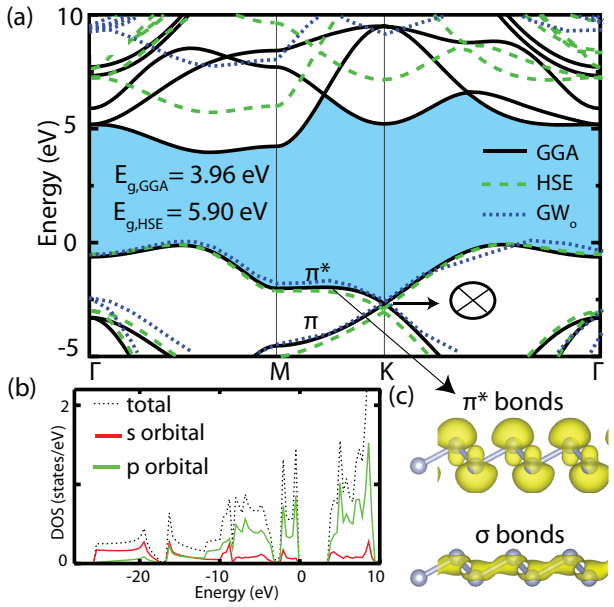

Figure 10.10: Free nitrogene: (a) Electronic band structure, (b) total and s- and p- orbital projected densities of states, (c) the charge density isosurfaces of states associated with π^* and σ bonds. The bands calculated by HSE and GW_o are shown with green dashed and blue dotted lines. The crossing at the K-point is highlighted. The zero of energy is set to the top of the valence band.

with nearest defects is minute. Upon the optimization of atomic structure no re-bonding took place between the two-folded nitrogen atoms surrounding the vacancy and hence the structure remained symmetric. The atoms surrounding the vacancy underwent a small relaxation, but a reconstruction observed in defect graphene [151, 152, 133] did not occur in nitrogene. The N-N bond lengths of the two-folded atoms reduce to 1.34 Å from their equilibrium value of 1.49 Å in pristine structure. The vacancy formation is endothermic with formation energy E_V=5.59eV. At the end, the defect structure remained stable by gaining 3 μ_B permanent magnetic moment per vacancy. The magnetic ground state of the defect structure complies with Lieb's theorem [153]. In addition, the buckled honeycomb structure of pristine nitrogene is preserved with a minute deformation at the close proximity of adsorbates such as H and O atoms that are adsorbed with binding energies of 2.06eV and 3.20eV, respectively.

Even if the above analysis predicts stability, it does not mean that free standing nitrogene can form by itself. Neither it can be exfoliated, since nitrogen does not

have a layered allotrope like graphite. Nonetheless, nitrogene can be grown on suitable substrates. Our stability analysis regarding the free standing nitrogene so far supports the fact that the nitrogene layers grown on substrates can remain stable. Although there are substrate surfaces which have lattice constants close to that of nitrogene, we consider Al(111) surface to examine the interaction between a reactive metal substrate and nitrogene. To compensate 7% lattice mismatch, we compress Al(111) uniformly. The binding energy of nitrogene to the Al(111) substrate is 190 meV/atom and consequently its spacing from the substrate is large as illustrated in Fig. 10.9(d). Notably, the equilibrium binding energy of fully relaxed nitrogene on graphene substrate is even weaker and 39 meV/atom. A weak interaction with these substrates does not alter the properties calculated for free nitrogene in the rest of the chapter. For example, the electronic structure of nitrogene on Al(111) is not modified.

10.2.3 Electronic Properties

Nitrogene is a nonmagnetic insulator with a band gap of E_g=3.96eV. Because of honeycomb structure, the bands originating from π- and π^*-like bonds cross each other and form cones around the K-point. However, in contrast to graphene and silicene, these π- and π^*-bands at the top of the valence band are filled, since the corresponding bonds are saturated. Calculations carried out by HSE show that the DFT band gap is underestimated by $\sim$ 2eV. Whereas the many body corrections through GW_o method overestimates the HSE band gap by 1.3 eV as seen in Fig. 10.10(a). The bands at the edges of conduction and valence bands are composed of mainly $2p$-valence orbitals of nitrogen. The bands at the bottom of the valence band are dominated by $2s$-orbitals. The charge density isosurfaces of π- and π^*-bands at the edge of the valence band clarify the role of the corresponding bonds in layer geometry. Since these bands are filled and separated from the empty bands by a large gap, free standing nitrogene is chemically inert. For example, H_2 and O_2 molecules can be bound by a weak vdW attraction of 89meV and 64meV, respectively. Single vacancy formation in nitrogene gives rise to three filled spin-down states and three empty spin-up states. These states are localized in the band gap and have a gap $\sim$ 0.4eV between them. The energy position of these localized gap states and the resulting high magnetic moments can be monitored by the decoration of vacancy in diverse patterns.

Since finite size ribbons are used in various applications, their stability and electronic properties become critical for the characterization of nitrogene. Here we consider armchair and zigzag edge geometries, which are specified by the number of nitrogen atoms n in their primitive unitcell. In Fig. 10.11(a) we show the primitive unitcell of the armchair nanoribbon with n=22 and the corresponding band structure with E_g=2.16eV direct band gap. The variation of E_g with the width of the ribbon or n shows a family behavior, especially for small n. The band gap E_g is small for low values of n, but it gradually increases with decreasing coupling between edges for large n, and eventually saturates at $E_g \sim$ 2.2eV for $n >$22. Two bands at the edge of valence and conduction bands (V and C) are derived from the edge states as demonstrated by the band decomposed charge density isosurfaces.

The edge atoms of the zigzag nanoribbon undergo a reconstruction. The structure optimization using primitive unitcell with n atoms mandates a fictitious, metallic structure. However, upon a Peierls type structural transformation, the metallic state changes to semiconductor. In Fig. 10.11(b) we present reconstructed structure of zigzag nanoribbon with $2n$=32 which is optimized in the 2×1 unitcell. The corresponding band structure with $E_g \sim$0.76eV gap is convenient for 2D electronic application. However, the band gap varies with $2n$; it is small for low values of $2n$, but increases and saturates to E_g=0.75eV for $2n > 32$ as presented in Fig. 10.11(b). The charge density isosurfaces of V and C bands clearly show that they are associated with edge states. Both armchair and zigzag nanoribbons have nonmagnetic ground state; as an example the nonmagnetic zigzag nanoribbon with $2n$=32 is favorable than the magnetic state by 394meV. In contrast to inert π- and π^*-bonds of nitrogene, the bonds of two folded atoms at the edge of nanoribbons are chemically active and can form strong bonds with foreign atoms. Upon the saturation of nitrogene at the edges by hydrogen atoms, the bands associated with edge states are discarded and the DFT band gap increases to $\sim$ 4eV for both armchair and zigzag nanoribbons.

10.2.4 Multilayers of Nitrogene

Not only single layer nitrogene, but also bilayer and its 3D graphitic phase constructed from the stacking of single nitrogene layers, namely nitrogenite are stable.

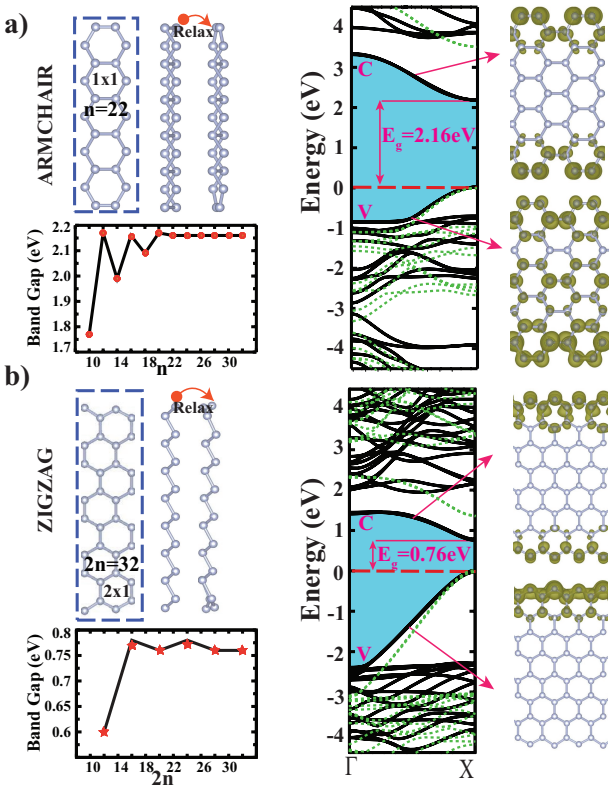

Figure 10.11: Nitrogene nanoribbons: (a) Atomic configuration and the energy band structure of the armchair nitrogene nanoribbon. Variation of band gap with n and charge density isosurfaces of specific band states at the edges of conduction(C) and valence(V) bands are shown. Energy bands calculated by HSE are shown by dashed lines. (b) Same for zigzag nanoribbon, where calculations are performed for 2×1 unit cell.

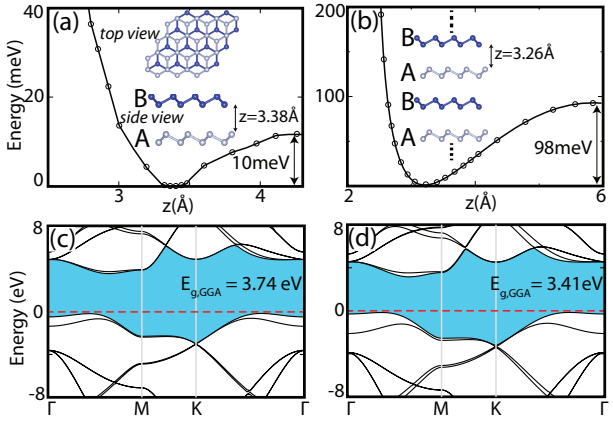

Figure 10.12: Bilayer and 3D layered nitrogene: (a) Minimum energy stacking geometry of bi-layer and the variation of the binding energy of layers with the distance z between them. The binding energies of layers E_b are given relative to $z \to \infty$. (b) Same for 3D nitrogenite. The electronic band structures of bi-layer (c) and nitrogenite (d).

The relative lateral displacement of adjacent nitrogene layers by $\mathbf{r} = (\mathbf{a}_1 + \mathbf{a}_2)/3$ leads to minimum energy, AB stacking for bi-layer as well as ABAB... stacking for 3D nitrogenite. Accordingly, three nitrogen atoms at the alternating corners of a hexagon face similar nitrogen atoms of the adjacent layers, while the remaining three nitrogen atoms face the centers of hexagons. This way the N-N bonds in each nitrogene become staggered relative to ones in the adjacent layers. The stacking geometry of layers described in Fig. 10.12 is reminiscent of graphene stacking in graphite. In the same figure, the variation of total energy relative to the spacing z between two layers is shown; the minimum energy occurs for z=3.38 Å, and the binding energy of layers is weak and is only E_b= 10meV/cell. However, owing to increased interlayer interactions from both sides, nitrogenite has relatively higher binding energy relative to free standing nitrogene layers (or exfoliation energy) E_b=98meV/cell and a relatively smaller interlayer distance of z=3.26Å . The weak interlayer interaction exhibits predominantly a vdW character. Consequently, bands of bilayer and nitrogenite are not affected significantly by the weak coupling between adjacent nitrogene layers.

10.3 Antimonene

Here we first examined the 3D bulk crystal of Sb having the trigonal lattice and R3-mh space group, which display a pseudo layered atomic configuration as if it is constructed by the stacking of the layers having buckled honeycomb structure. Using structure optimizations based on conjugate gradient method we then revealed two single-layer phases of Sb, namely buckled antimonene (B-antimonene or simply B-Sb) similar to silicene and washboard antimonene (W-antimonene or simply W-Sb) similar to black phospherene. While W-Sb is prone to long wavelength instability, an asymmetric washboard structure (aW-antimonene or simply aW-Sb) is found to have slightly lower energy. We carried out an extensive analysis to ensure that B-Sb and aW-Sb single-layer structures are stable above the room temperature. We examined the character of their bonding and investigated the effects of vacancy defects. We then characterized these phases, their quasi 1D nanoribbons, bilayers and multilayers by calculating their mechanical, electronic and magnetic properties. Furthermore we showed how these properties deduced for suspended antimonene are modified when antimonene was grown on substrates like germanene and Ge(111) surfaces.

10.3.1 3D Crystal of Sb

Antimony has a 3D crystal with trigonal lattice and (R3-mh) space group. Experimental values[154] of this 3D crystalline phase structure are the cohesive energy, E_C=2.75 eV/atom and the trigonal lattice constants a=b=4.31 Å, c=11.27 Å, and Sb-Sb bond distance 2.91 Å. Our calculated values obtained from full structure optimization are E_C=3.12 eV/atom, a=b=4.28 Å, and c=11.18 Å. In Fig. 10.13 (a), the atomic configuration together with the relevant structural parameters are illustrated. This 3D bulk phase can be viewed as consisting of ABCABC type of stacking of the single-layer structure. Each isolated single-layer can be identified as a buckled honeycomb structure with three fold rotation axis passing through the center of hexagons. Because of the ABC stacking, the Sb-Sb bonds exhibit a staggered arrangement in the top view. The smallest interlayer spacing between single layers is z=2.3 Å and hence it allows not only vdW attraction, but also significant chemical interaction. This is clarified by the contour plots of the total charge density on a plane including two atoms in different layers. In

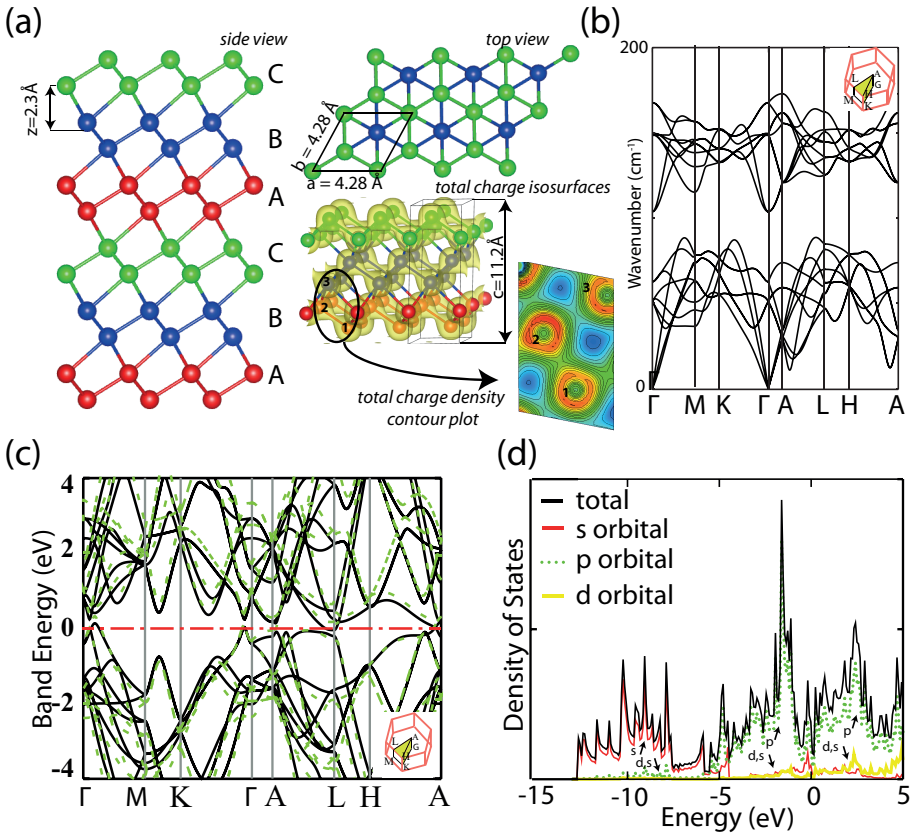

Figure 10.13: 3D bulk crystal of Sb. (a) Side and top views of the optimized atomic configuration and structural parameters. Pseudo layered character of the crystal is highlighted by atomic layers exhibiting ABCABC.. stacking. Inlayer and interlayer bonding is depicted by isosurface and contour plots of the total charge density. (b) Calculated dispersion relations of bands of vibrational frequencies. The Brillouin zone is shown by inset. (c) Electronic energy bands calculated within PBE. The correction by HSE is shown by green-dashed lines. The zero of energy is set to the Fermi level. (d) Total and orbital projected densities of states.

this respect, 3D Sb is different from graphite and MoS_2, where interlayer binding is mainly vdW attraction. Because of significant interaction between layers we identify this 3D crystal as pseudo-layered. The calculated bands of the vibration frequencies are presented in Fig. 10.13 (b). As shown in Fig. 10.13 (c), the phase of antimonene crystal studied in this chapter is a metal. Corrections to DFT band energies using HSE06 method confirmed the metallic state. Metallicity is attained by strong coupling between adjacent layers of buckled honeycomb structure. The total and orbital projected densities of states in Fig. 10.13 (d) show that $5p$-like orbital states dominate the top of the valence band and the bottom of the conduction band, whereas lower part of the valence band is derived from $5s$-orbitals. Pseudo layered character of the 3D Sb crystal has led us to consider first the 2D single-layer, buckled honeycomb structure of Sb similar to silicene.[155, 93]

10.3.2 Monolayer Antimonene

Considering the atomic structure of the layers in 3D bulk crystal in Fig. 10.13 (a), we performed structure optimizations including lattice constants using CG method, and found that the suspended buckled honeycomb structure with 2D hexagonal lattice can be indeed a candidate for a stable structure corresponding to a local minimum on the Born-Oppenheimer surface. We specify this single-layer structure as B-antimonene. To increase the degrees of freedom of structure optimization using (1×1) primitive cells, we repeated the structure optimization calculations using (4×4) supercells, which also ended with the same geometry and cohesive energy. Incidentally, the planar honeycomb structure did not survive after structure optimization despite its cohesive energy of 2.20 eV/atom.

B-antimonene structure has a cohesive energy of 2.87 eV/atom and formation energy of -0.25 eV/atom relative to the 3D pseudo layered Sb crystal structure (having R3-mh space group). In Fig. 10.14 (a), the atomic structure, 2D hexagonal lattice, the primitive unit cell and various relevant structural parameters including bond angles, α and β are presented. In the B-antimonene structure, the sp^2-bonds of unstable planar honeycomb structure are rehybridized to maintain the stability through the buckling of Δ=1.67 Å, whereby the three $sp^{n\alpha}$ orbitals of one Sb atom having the bond angle $\alpha = 89^o$ with three nearest Sb

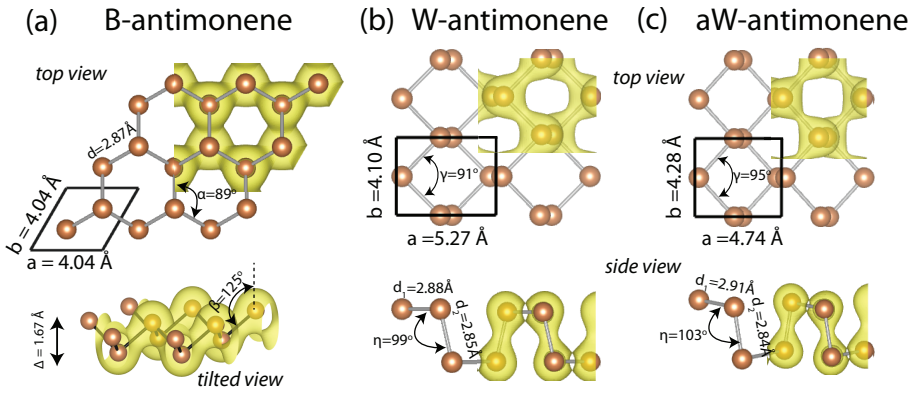

Figure 10.14: 2D structures of antimony. (a)The equilibrium 2D crystalline structure of buckled honeycomb structure, *i.e.* B-antimonene, with hexagonal lattice. The primitive unit cell has two Sb atoms. Optimized values of the structural parameters, such as lattice constants, bond lengths and bond angles are also shown. Bonding between Sb atoms is depicted by the isosurfaces and contour plots of the total charge density. Δ is the buckling, where Sb atoms on the corners of the hexagon alternatively move up and down. (b) Same for 2D, symmetric washboard structure, *i.e.* W-antimonene, having 2D rectangular lattice. Rectangular primitive unit cell has four Sb atoms. In the side view one deduces two atomic planes. (c) Same for 2D, asymmetric washboard structure, *i.e.* aW-antimonene, with rectangular lattice. The primitive unit cell has four Sb atoms; single-layer structure is composed of four atomic planes.

atoms form covalent σ-bonds and provide the rigidity of antimonene. Remaining two electrons on each Sb atom form $sp^{n\beta}$ orbitals with relatively high p contribution, which ooze perpendicularly. They are involved in the π- and π^*-like bonds between the pairs of up and down Sb atoms in the primitive unit cell. In this respect, unlike graphene and silicene, which have unsaturated metallic bonds, the bonds of B-antimonene are saturated. The bonding of B-antimonene is illustrated by the isosurfaces of the total charge density in Fig. 10.14 (a).

The mechanical properties of B-antimonene are characterized by its in-plane stiffness, $C = A_0^{-1}\delta^2 E_T/\delta\epsilon_T^2$ and the Poisson's ratio, $\nu = -\epsilon_x/\epsilon_y$, A_0 being the equilibrium area of the unit cell. The calculated values are $C_x = C_y$=41 N/m and ν_{xy}=ν_{yx}=0.21. Apparently, the stiffness of B-Sb is much lower than that of graphene (with C=350 N/m) or BN (with C=240 N/m), but comparable to that silicene (with C=65 N/m^2). Antimony being the fifth row element makes longer but weaker bonds as compared to the second row elements.

The optimized atomic structure with relevant structural parameters and the bonding of the single-layer, symmetric washboard structure, namely W-antimonene are described in Fig. 10.14 (b). This structure has 2D rectangular lattice like black phospherene and contains four Sb atoms in the primitive unit cell. Its calculated cohesive energy and formation energy are 2.88 eV/atom and -0.24 eV/atom, respectively. Like B-antimone, each Sb atoms are threefold coordinated with in-plane Sb-Sb bond distance of 2.85 Å and interplanar Sb-Sb bond distance of 2.88 Å. The corresponding bond angles are γ=91^o and η=99^o. Accordingly, the single-layer W-antimonene consists of two parallel atomic planes. This atomic configuration attributes directional elastic properties to W-antimonene, namely C_x=14 N/m and ν_{xy}=0.42, but C_y=34 N/m and ν_{yx}=1.01.

The total energy of symmetric W-antimonene can be further lowered by 10 meV/atom, if one of two Sb atoms, which were located in either plane in the primitive unit cell of symmetric W-Sb, are slightly displaced outwards and also the lattice constants of the rectangular primitive cell are modified. This asymmetric reconstruction takes place to prevent the structure from the long wave length instability, as we discuss in the forthcoming sections. We specify the asymmetric structure as aW-antimonene in the rest of the chapter. In Fig. 10.14 (c) we describe the atomic structure of aW-Sb together with its relevant structural parameters and isosurfaces of total charge distribution. Similar to W-Sb, aW-Sb has

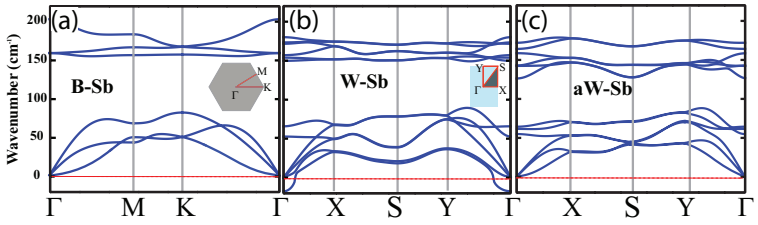

Figure 10.15: Vibrational frequencies of 2D Sb. The Brillouin zones and their symmetry directions are shown by insets. (a) B-antimonene. (b) W-antimonene with imaginary frequencies as $\mathbf{k} \rightarrow 0$. (c) aW-antimonene.

strongly directional mechanical properties with C_x=12 N/m and ν_{xy}=0.36, but C_y=29 N/m and ν_{yx}=1.20. High Poisson;s ratio is indigenous to the washboard structure.

10.3.3 Stability

Rather high cohesive energies of optimized structures at T=0 K may not ensure that 2D antimonene phases correspond to deep minima in the Born-Oppenheimer surface. In fact, these 2D structures may undergo instabilities due to long wavelength lateral/transversal displacements, as well as thermal excitations at high temperatures. The most critical issue we have to clarify is whether these 2D antimonene phases are stable and remain stable at high temperature. In order to verify B-, W-, and aW-antimonene remain stable against low frequency acoustic vibrations inducing long wavelength transversal/longitudinal displacements in different directions of the BZ, we calculated the frequencies of vibrational modes using a fine grained **k**-point sampling. The vibrational bands including the ZA band along symmetry directions of BZ are presented in Fig. 10.15(a)-(c). The optical branches are well separated from the acoustic branches. All calculated frequencies are positive ensuring the stability of B-antimonene. However, for the symmetric W-Sb, the vibrational frequencies of specific branches becomes imaginary as $\mathbf{k} \rightarrow 0$ as shown in Fig. 10.15 (b). This indicates instability in W-Sb structure for long wavelength acoustic vibrations. This instability has been restored through the reconstruction of the atomic structure leading to aW-Sb, all of its modes attained positive vibrational frequencies in Fig. 10.15 (c).

Even if the stability is assured through the positive frequencies of all vibrational

modes in BZ, the structure may correspond to a shallow local minimum on the Born-Oppenheimer surface. Thus, the structure can be prone to instability at finite temperature. Further to the calculations of vibrational frequencies, we performed ab-initio MD calculations to test the stability at high temperature. First, both structures remained stable at 700 K for 3 picosecond. Then the temperature increased to 1000 K. Both B-Sb and aW-Sb structures remained stable for ab-initio MD simulations lasting 2 picosecond at 1000 K. These MD results indicate that both antimonene structures can maintain their stability at least above the room temperature and hence the local minima corresponding to these phases are deep enough to sustain their various applications above the room temperature.

Next we address the questions of whether the stability of antimonene phases are affected by vacancy defects. The isolated vacancy defects are treated b y periodically repeating them in a 5×5 supercell of antimonene, whereby the coupling with nearest defects is minimized. For single vacancy defect in B-Sb, three two folded Sb atoms around the vacancy are relaxed and formed an equilateral triangle, whereby the second nearest neighbor distance is reduced from 4.05 Å to 3.72 Å. Accordingly, the structure around the vacancy is squeezed, but remained symmetric without re-bonding of surrounding atoms. This situation is in contrast to the vacancy in graphene, where reconstruction or re-bonding of carbon atoms surrounding the vacancy is observed. [151, 152, 133] The vacancy formation is an endothermic process and the formation energy of the single vacancy in B-Sb is 5.03 eV. At the end, the defect structure remained stable by gaining permanent magnetic moment μ=1.0 μ_B per vacancy. The single-vacancy defect in aW-Sb displays similar behavior. Vacancy formation energy is relatively smaller and is 4.22 eV. Three Sb atoms surrounding the vacancy undergo a relaxation without re-bonding. They form a triangle with edges of $\sim$ 3.60 Å. The single vacancy in aW-Sb structure attained also a permanent magnetic moment of 0.6 μ_B per vacancy. Clearly, like B-Sb, the single vacancy defect does not cause any instability in aW-Sb.

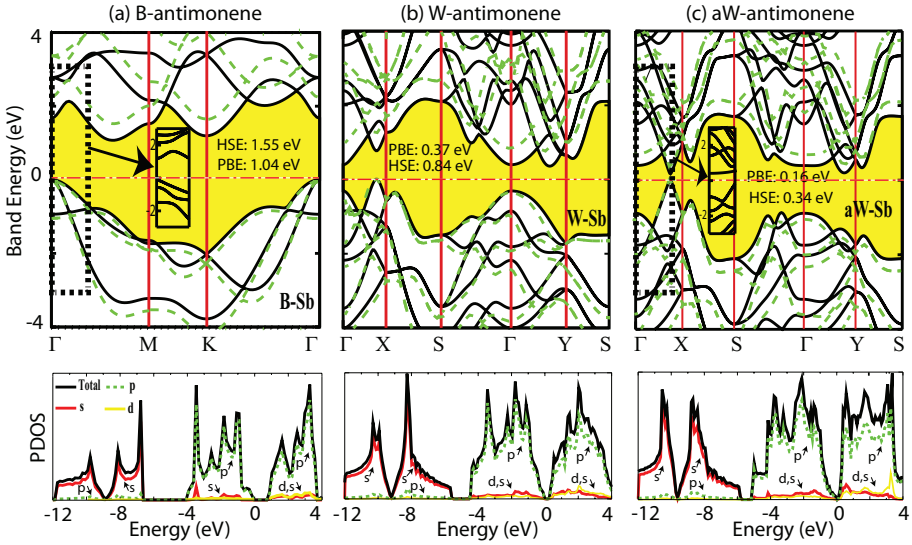

Figure 10.16: The electronic band structure together with the total and orbital projected densities of states of the single-layer antimonene phases. Zeros of the band energy are set at the maximum of the valance bands. Bands corrected by HSE are shown by green-dashed lines. Bands calculated by including spin-orbit coupling are shown by insets. (a) B-antimonene. (b) W-antimonene. (c) aW-antimonene.

10.3.4 Electronic Structure

We gain insight into electronic properties of antimonene phases. As shown in Fig. 10.16 (a), B-antimonene is a nonmagnetic insulator with an indirect band gap of 1.04 eV calculated within PBE approximation, which occurs between the minimum of the conduction band along $\Gamma - M$ direction and maximum of the valance band at the Γ point. Calculations carried out by HSE show that the DFT band gap is underestimated by $\sim$ 0.51 eV, hence this indirect band gap increases to 1.55 eV after HSE correction. As shown by inset in Fig. 10.16 (a), under the spin orbit coupling the degeneracies at the top of the valance band are removed to split the bands further and the indirect band gap is reduced by 0.25 eV. Apparently, the bad gap of B-antimonene lies in the range, which is convenient for several electronic applications. In this respect B-antimonene keeps the promise of potential applications in 2D flexible electronics. The total and s-, p- and d-orbital projected densities of states indicate that $5p$ orbital states dominate the top of the valence and the bottom of the conduction bands. While the contribution s-orbital states increases in lower parts of the valence band,

d-orbital states contribute to the upper parts of the conduction band.

We also discuss the calculated electronic structure of symmetric W-antimonene for the sake of completeness. In Fig. 10.16 (b), the indirect band gap occurs between the minimum of the conduction band at Γ point and the maximum of the valance band along the $\Gamma - X$-direction. The band gap is calculated within the PBE approximation is found to be 0.37 eV, which increases to 0.84 eV after HSE correction. In Fig. 10.16 (c), the band gap of the aW-antimonene decreases to 0.16 eV upon asymmetric Sb-Sb bond formation. After HSE correction this band gap increases to 0.34 eV. The direct band gap calculated by PBE increases from 0.16 eV to 0.19 eV, when the spin orbit coupling is taken into account.

10.3.5 Multilayers

For single-layer structures like MoS_2 it is known that the electronic properties undergo to gradual changes when additional layers are stacked above the first layer. To reveal whether similar changes can occur in antimonene, we investigated bilayer and trilayer structures of B-Sb. Furthermore, we explored whether the multilayer structure may be the precursor for the 3D graphitic structures or they can be associated with the thin slab of the 3D bulk crystal. The total energies of the bilayer and trilayer are calculated as a function of the interlayer distance z. For each value of z the atomic positions and lattice constants are optimized. In Fig. 10.17 (a) we show the variation of the total energy as a function of z. In the same figure is shown also the minimum energy AB stacking of B-antimonene single layers, whereby the B-layer is displaced by $\mathbf{r} = (\mathbf{a} + \mathbf{b})/3$ relative to the adjacent A-layer. The equilibrium spacing is found to be z=3.81 Å, which is approximately 30% longer than the Sb-Sb bonds. The binding energy in equilibrium is 333 meV per cell or $\sim$ 83 meV/atom. This binding energy is also confirmed by calculating the difference of the total energies of the free B-Sb single-layer and of the bilayer from the expression, $E_b = E_T[B - Sb]/2 - E_T[bilayer]/4$. The binding energy is composed of vdW and chemical interactions between two layers. However, the chemical interaction leads to significant changes in the electronic structure of bilayer. Specifically, the semiconducting, single-layer B-antimonene changes into a metal when two of them are AB stacked to form a bilayer as shown in Fig. 10.17 (b).

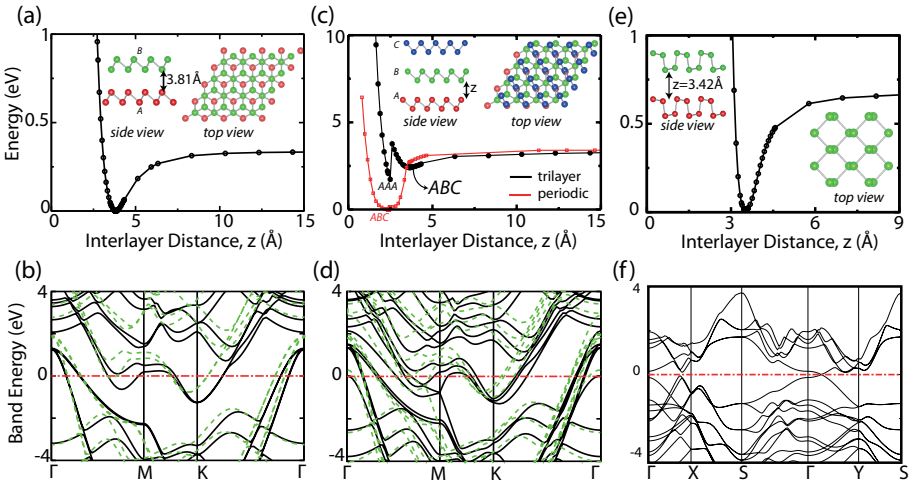

Figure 10.17: (a) Minimum energy AB stacking geometry of the B-antimonene bilayer and the variation of its total energy with the distance z between the layers. The total energies are given relative to $z \rightarrow$ infinity. (b) Energy band structure of bilayer corresponding to the equilibrium spacing. Calculations using HSE presented by green dashed lines. (c) Same for trilayer of B-antimonene in ABC stacking. The first minimum of the total energy occurs at z=3.65 Å. Upon overcoming an energy barrier the second minimum occurs at z=2.5 Å. The variation of the optimized total energy of the periodic 3D structure as a function of z, which exhibits a single minimum at z=2.37 Å corresponding to the pseudo layered 3D bulk crystal. (d) The energy band structure of the trilayer in the first minimum at z=3.65 Å. (e) Minimum energy AA stacking geometry of aW-antimonene bilayer and the variation of its total energy with the distance z between layers. Top and side views of atomic structures are shown by insets. (f) Energy band structure of aW-antimonene bilayer in (e).

In the trilayer the interlayer interaction is relatively stronger and is calculated to be 0.7 eV per cell or $\sim$ 117 meV/atom, since the middle layer is capped from both sides. This is reflected to the equilibrium interlayer separation, which is calculated to be z=3.65 Å. It is 0.16 Å smaller than that of bilayer. The variation of the structure optimized total energy as a function of z is presented by the black (dark) curve in Fig. 10.17 (c). The ABC stacking is found to be the most energetic stacking. Decreasing the interlayer separation of the trilayer z from equilibrium value requires to overcome an energy barrier of 1.35 eV. Thereafter, a structural transformation takes place, where the interlayer separation is reduced suddenly to z=2.5 Å and the total energy drops to a second minimum. In this transformation, the ABC stacking changes to either AAA or ABA stacking. The energy difference between these two different stacking geometries is minute; their binding energies approximately 113 meV/atom stronger than that in the first minimum. Similar structural transformation is explored for multilayers, which are treated by a periodically repeating structure with ..ABCABC.. stacking as in the 3D pseudo layered bulk crystal in Sec.III. Here the structure optimized total energy is calculated as a function of the interlayer spacing, z ranging from z=15 Å to z=2 Å. As shown with the red curve in Fig. 10.17 (c), this periodic structure has a single minimum at z=2.37 Å with the binding energy of 3.40 eV per cell; it is identical to the 3D pseudo layered structure. Accordingly, the single-layer B-antimonene does not construct a 3D graphitic structure with wide interlayer spacing, it rather replicates 3D pseudo layered bulk crystal as the number of antimonene layers increases. The electronic structure of the trilayer with z=3.65 Å is similar to that of bilayer and displays a metallic character in Fig. 10.17 (d)

In the bilayer of aW-antimonene, the AA stacking attains the minimum energy. The equilibrium interlayer separation occurs at z=3.42 Å and the binding energy is 83 meV as shown in Fig. 10.17 (e). Similar to the bilayer of B-antimonene, the electronic structure exhibits a metallic character with bands crossing at the Fermi level along the $\Gamma - Y$ direction in Fig. 10.17 (f).

10.3.6 Antimonene on substrates

Since suspended single layers cannot form by itself, they can be grown on suitable substrates. Under these circumstances, the substrate-antimonene interaction

becomes crucial and may affect the properties revealed for the suspended single-layers. To explore to what extent the properties of grown layers are influenced we investigated binding energy and electronic band structure of B-Sb grown on germanene and Ge(111) substrates, which are nearly lattice matched.

The atomic structure of B-Sb grown on germanene with AA and AB stacking has been optimized. As shown in Fig. 10.18 (a), we found that AB stacking is favorable energetically and has binding energy 250 meV per Sb atom. The equilibrium separation between Sb and Ge layers is z=3.01 Å. This material consisting of two single-layer honeycomb structures is a metal due to a significant interlayer coupling as shown in Fig. 10.18 (b). The comparison made between TDOS of free B-Sb and DOS projected to B-Sb grown on germanene in Fig. 10.18 (c) clearly indicates the influence of germanene substrate . The stability and significant interaction between germanene and antimonene suggests that composite materials derived from lateral stacking of $(\text{B-Sb})_p/(\text{Germanene})_q$ (p and q denote the numbers of layers) or their periodic alternation can be fabricated to achieve diverse functionalities. Notably, owing to significant interlayer chemical interaction this composite structure is rather different from van der Waals heterostructures.

As an alternative substrate, the Ge(111) surface is considered, which is mimicked by a slab of bulk Ge consisting of three (111) atomic planes. The top and side views of the optimized atomic structure of B-Sb on the Ge(111) substrate are shown by insets in Fig. 10.18 (d), where the optimized total energy versus the spacing between Ge(111) and B-Sb is also presented. The binding energy is 400 meV per Sb atom, and the equilibrium separation is 2.37 Å. The energy bands corresponding to the equilibrium structure of B-antimonene grown on Ge(111) is metallic in Fig. 10.18 (e). The total and projected densities states and their comparison with the total density of states of free B-Sb single-layer in Fig. 10.18 (f) clearly indicates significant substrate effects on the properties of antimonene. In particular, high density of states of grown Sb layer at the Fermi level is noted. While Ge and germanene engaged in significant interaction with the grown B-Sb and they modified its electronic band structure, there might be substrates, which do not affect the properties of grown antimonene phases.

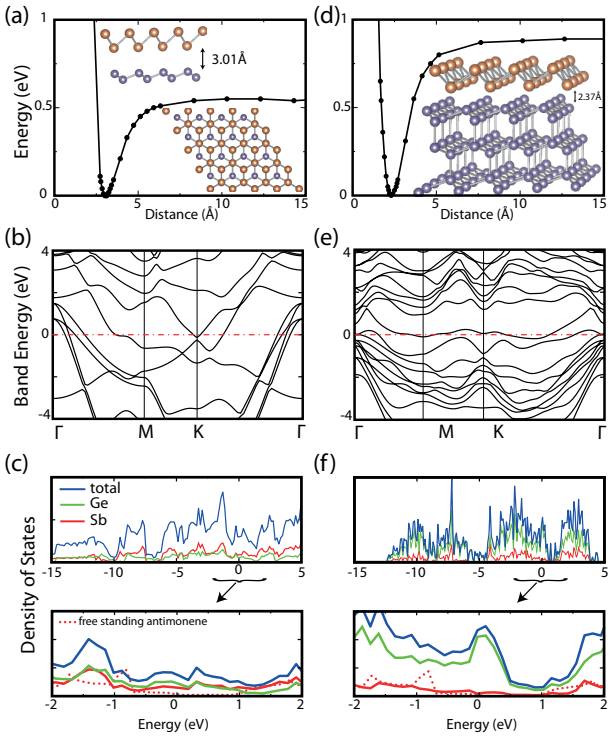

Figure 10.18: (a) The optimized atomic structure and binding interaction of B-antimonene grown on germanene surface (i.e. graphene like structure of Ge atoms). The registry of Sb and Ge atoms are shown by inset. (b) Corresponding electronic energy band structure. (c) Total and partial densities of states (DOS) projected on Sb and Ge atoms. The comparison of the total density of states of free B-Sb single-layer structure with the density of states projected on the Sb atoms grown on germanene indicates significant substrate influence. (d)-(f) Same for B-antimonene grown on the Ge(111) substrate. The zero of energy is set to the Fermi level shown by dash-dotted line.

10.4 Nanoribbons

Since finite size ribbons or patches of antimonene shall be used in various applications, their stability and electronic properties become relevant for the characterization of antimonene phases. Here we consider armchair and zigzag edge geometries, which are specified by the number of Sb atoms, n in their primitive unitcell. In Fig. 10.19(a) we show the primitive unitcell and optimized atomic structure of the B-antimonene armchair nanoribbon with n=22 and the corresponding electronic energy band structure. Relaxations occur mainly at the edges. B-antimonene nanoribbon has nonmagnetic ground state. Two bands, each located at the edge of valence and conduction bands (V and C, respectively) delineate the band gap in the momentum space. They are derived from the states localized at the edges as demonstrated by band decomposed charge density isosurfaces. The PBE indirect band gap is calculated to be E_g=0.218 eV, which increases to E_g=0.574 eV after HSE correction. The variation of the PBE band gap E_g with the width of the ribbon or n is also shown.

Since the edge atoms of the zigzag B-Sb nanoribbon undergo a reconstruction, the structure optimization using the primitive unitcell with n atoms mandates a fictitious, metallic structure. However, upon a Peierls type structural transformation in the 2×1 cell, the metallic state changes to ferromagnetic semiconductor. Because of reconstruction the structure optimization and energy band structures are performed using the 2×1 unit cell. The atomic configuration, energy band structure, charge density isosurfaces of specific states of the zigzag B-Sb with $2n$=32 are presented in Fig. 10.19 (b). The variation of the band gap with $2n$ is also given in the same figure. The small energy gap between filled spin up and empty spin down bands is calculated within PBE to be E_g=0.200 eV. Upon HSE correction this band increases to 0.872 eV. Isosurfaces of charge density of specific states at the band edges demonstrate that they are constructed predominantly from the orbitals of edge atoms. Hence these states are localized at the edges of the nanoribbon. The PBE band gap is $\sim$ 0.1 eV for $2n$=20, but increases to 0.23 eV for $2n$=40.

In Fig. 10.20 (a) we present atomic configuration, electronic band structure of armchair and zigzag nanoribbons of aW-antimonene. The armchair nanoribbon with n=22 is a nonmagnetic semiconductor with a PBE band gap of 0.20 eV,

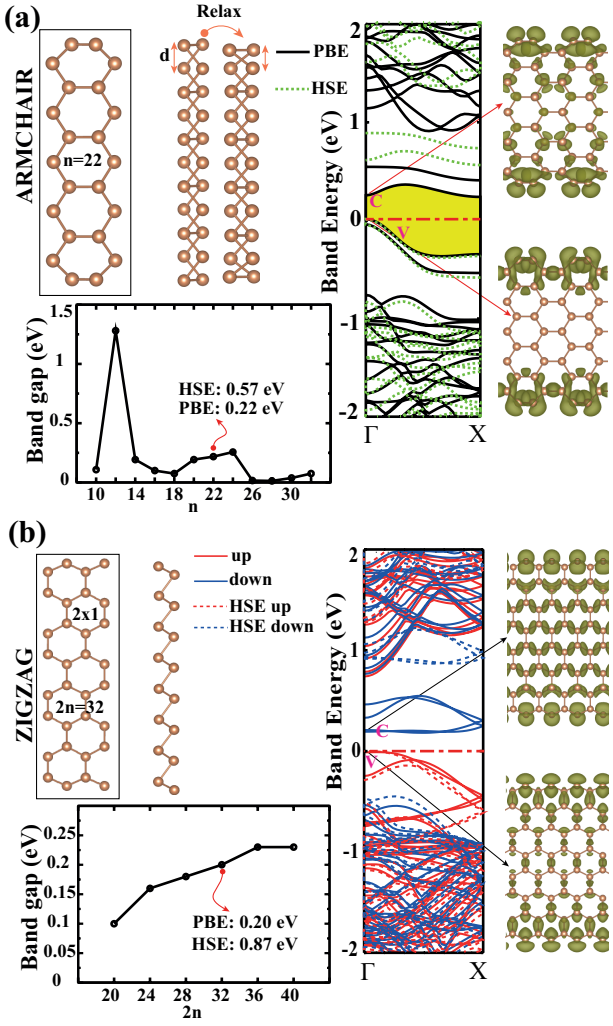

Figure 10.19: (a) The primitive unit cell, optimized atomic configuration and the energy band structure of the armchair B-antimonene nanoribbon. The variation of band gap with n and charge density isosurfaces of specific band states at the edges of conduction(C) and valence(V) bands are also shown. Energy bands corrected using HSE are shown by dashed lines. (b) Same for the zigzag B-antimonene nanoribbon. Structure optimization and band calculations are performed using 2×1 unit cell. The zero of energy is set at the top of the valence band. Spin up and spin-down bands are shown by red and blue lines, respectively. Spin-up and spin-down bands corrected using HSE are also shown by dashed red and blue lines, respectively.

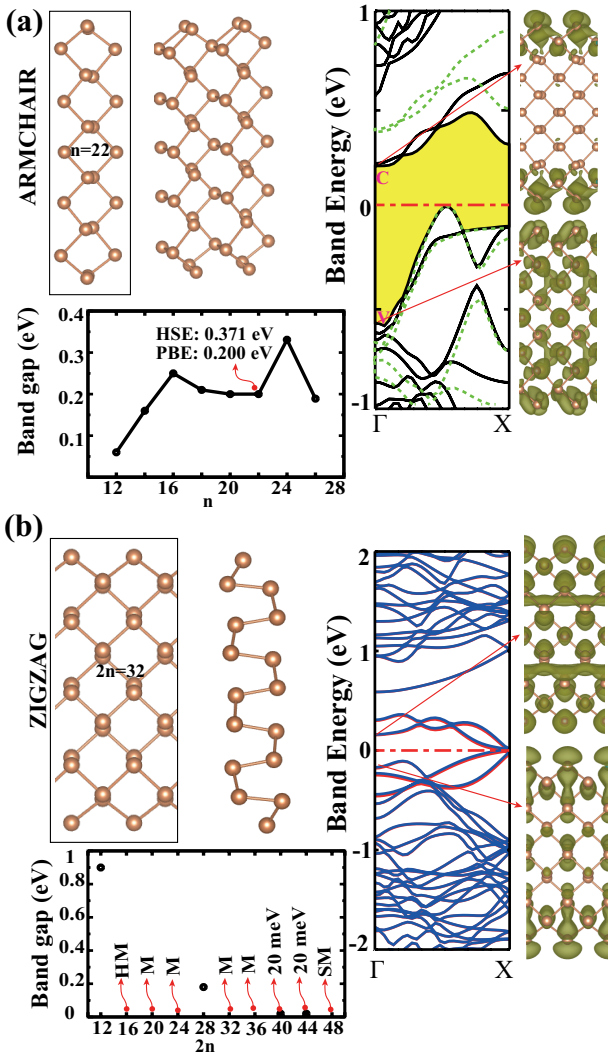

Figure 10.20: (a) The primitive unitcell having n Sb atoms, optimized atomic structure and the energy band structure of the armchair aW-antimonene nanoribbon. The variation of band gap with n and charge density isosurfaces of specific band states at the edges of conduction (C) and valence(V) bands are also shown. Energy bands calculated by HSE are shown by dashed lines. The zero of the energy is set at the top of the valence band. (b) Same for the zigzag aW-antimonene nanoribbon, where due to the reconstructions of edges calculations are performed using 2×1 unit cell. Spin up and spin-down bands are shown by red and blue lines, respectively. The zero of energy is set at the Fermi level.

which increases to 0.37 eV after HSE correction. Isosurfaces of the selected states at the band edges illustrate the contribution of the edge atoms. The PBE bands vary between 0.1 eV and 0.33 eV depending on the values of n. The zigzag nanoribbon of aW-Sb is treated in 2×1 unit cell due to edge reconstruction. For $2n$=32 the zigzag nanoribbon is a metal. However, the character of the ribbon appears to strongly depend on its width. Depending on the values of $2n$, the zigzag nanoribbon of aW-Sb can exhibit diverse properties, such as metallic, semimetallic, half-metallic and semiconducting, as shown in in Fig. 10.20 (b).

10.5 Summary

In this chapter, we focus on new material design and prediction using first principles calculations. We first investigated silica or SiO_2, the main constituent of earth's rocks which has several 3D complex crystalline and amorphous phases, but does not have a graphite like layered structure in 3D. Our theoretical analysis and numerical calculations predicts that a single-layer honeycomb like allotrope, hα-silica, can be derived from the oxidation of silicene and it has intriguing atomic structure with re-entrant bond angles in hexagons. It is a wide band gap semiconductor, which attains remarkable electromechanical properties showing geometrical changes under external electric field. In particular, it is an auxetic material with negative Poisson's ratio and has a high piezoelectric coefficient. While it can form stable bilayer and multilayer structures, its nanoribbons can show metallic or semiconducting behavior depending on their chirality. Coverage of dangling Si orbitals by foreign adatoms can attribute new functionalities to hα-silica. In particular, Si_2O_5, where Si atoms are saturated by oxygen atoms from top and bottom sides alternatingly can undergo a structural transformation to make silicatene, another stable, single layer structure of silica.

In the following section, we predict that nitrogen can form single layer, buckled honeycomb structure called nitrogene, which is rigid and stable even above the room temperature. This 2D crystalline phase of nitrogen is a nonmagnetic insulator and rather inert due to the saturated π-bonds. Its zigzag and armchair nanoribbons have fundamental band gaps derived from reconstructed edge states. These band gaps are tunable with size and suitable for the emerging field of 2D electronics. Nitrogene forms not only bilayer, but also 3D graphitic multilayer

structures. When grown on a substrate like Al(111) surface and graphene, nitrogene binds weakly to substrates and hence preserves its free standing properties, but it can easily be pealed off.

Similar to nitrogen, the pseudo layered character of 3D bulk crystal of antimony (Sb films) has led us to predict its 2D single-layer crystalline phase named as antimonene in buckled honeycomb structure like silicene. Sb atoms also form asymmetric washboard structure like black phospherene. Based on an extensive analysis comprising ab-initio phonon and finite temperature molecular dynamics calculations, we show that these two single-layer phases are robust and can remain stable at high temperatures. They are nonmagnetic semiconductors with band gaps ranging from 0.3 eV to 1.5 eV, and are suitable for 2D electronic applications. The washboard antimonene displays strongly directional mechanical properties, which may give rise to strong influence of strain on the electronic properties. Single-layer antimonene phases form bilayer and trilayer structures with wide interlayer spacings. In multilayer, this spacing is reduced and eventually the structure changes to 3D pseudo layered bulk crystal. The zigzag and armchair nanoribbons of the antimonene phases have fundamental band gaps derived from reconstructed edge states and display diversity of magnetic and electronic properties depending on their width and edge geometry. Their band gaps are tunable with the widths of the nanoribbons. When grown on substrates, such as germanene or Ge(111), the buckled antimonene attains significant influence of substrates.

Chapter 11

Conclusions

This thesis was dedicated to investigation of the electronic, mechanical and optical properties of honeycomb-like monolayer structures for understanding the fundamental laws of physics at nanoscale and utilizing them for designing new device models. Our explorations follow three main routes; utilizing formerly known materials for new device design and characterizing their properties, explaining experimental observations present in the literature by means of first principle quantum mechanical calculations and discovering new stable monolayer materials which do not exist in nature.

In the first part of the thesis, graphene / boron nitride heterostructures were investigated. First, in Chapter 3, the growth mechanism of epitaxial graphene on boron nitride was revealed. Although experimental procedures for synthesizing boron nitride on graphene was known, the atomistic mechanisms taking place during the epitaxial growth and nucleation of graphene growth was missing. Here we showed that there are two mechanisms which play crucial roles in the growth of graphene. First mechanism is the formation of large carbon rings at the edges which eventually collapse to form honeycomb structure with defects. This collapse is found to be initiated by the new coming carbon atoms which replace one of the bonds in the ring, and expands it until the critical size is reached. Second mechanism is the formation of pentagon-heptagon defects near the edge and their healing. We have shown that the energy barrier needed to overcome during the

healing of the pentagon-heptagon defects are much lower than that of the Stone-Wales defects. We have shown that the presence of a BN or Ni substrate have crucial effect on growth. These substrates guide the formation of honeycomb structures from carbon rings and enable the healing of specific defects as growth proceeds. We also studied graphene growth using carbon dimers as building blocks and found that defect formation is less frequent as compared to growth with monomers.

Using the vertically grown graphene / boron nitride heterostructure, we proposed and characterized a nanoscale capacitor model in Chapter 4. In this model we showed that by applying electric field to vertically stacked graphene / BN layers, it is possible to create a charge separation between the metallic graphene plates. We then calculated the stored charge, energy and potential difference between the metallic layers and showed that this model has a high gravimetric capacitance value in the range of supercapacitors. More interesting results were obtained when we compared this model with the classical Helmholtz capacitor model. We showed that as the size of our model increased, it started to act exactly like a classical capacitor, however due to the quantum mechanical effects at small separations, the nano-capacitor acted differently and gave high capacitance values. Thus, by an immediate application of density functional theory on our model, we were able to observe how quantum mechanical effects become dominant as we go into nanoscale. Furthermore, one year after publishing our results, these findings were further confirmed by a following experimental study [17].

Similar to vertical heterostructures, we also studied lateral graphene / boron nitride composites and their applications as a nanoscale planar capacitor in Chapter 5 and 6. Our study fills an important gap in this field regarding the size dependence of the electronic properties of Graphene/BN composites consisting of planar stripes of each. Although there are various studies in the literature about graphene / BN heterostructures, a systematical study graphene/BN composite stripes and the dependence of their properties on geometrical modifications were missing. We revealed 1D, as well as 2D aspects together with the transition between 1D to 2D. We showed important features of the 2D aspect, which was absent before. We presented an extensive analysis of electronic structure for laterally repeating (periodic) graphene/BN heterostructures with varying widths which is essential for the understanding of these heterostructures and their applications.

The concept of δ-doping and its dramatic effects to modify the electronic structures has been introduced to in-plane heterostructures for the first time. Charge separation in Graphene/BN/Graphene nanoribbons under the external in-plane electric field was explained which leads to planar nanoscale dielectric capacitors. The proposed planar nanoscale model which allows diverse parallel, series and mixed combinations to achieve desired values of charge separation, energy storage and potential difference values can be fabricated in the same plane of micro or nano-circuits for crucial electronic applications.

Apart from their planar honeycomb geometries, carbon and boron nitride composite nanustructures were further investigated in one dimension in the form of short atomic chains in Chapter 7. We revealed the growth mechanism of carbon and BN atomic chains on single layer honeycomb structures. We found that with the inclusion of each new carbon atom, the existing atomic chain consisting of n carbon atom leaves its previous position to join with the new carbon atom to from a chain of $n+1$ carbon atom. These growth processes were simulated by ab-initio molecular dynamics calculations at various temperatures and the resulting chain structures were shown to be stable even though they are free to bend and slightly tilt. The growth of atomic chains on the single layer honeycomb structures heralds a self-assembly process, which may have fundamental and technological implications. The grown chains by themselves, exhibit interesting physical and chemical properties depending on the number of atoms forming the chain and the type of chain atom attaching to the substrate. In particular, the physical properties of even numbered and odd numbered carbon chains can behave differently leading to interesting even-odd disparity. We also showed that atomic chains grown on single layer substrates attribute useful functionalities to bare h-BN and graphene. These properties are dependent on the number of carbon atoms in the chains. Apart from creating localized electronic states in the band gap and local magnetic moments it is demonstrated that carbon chains can also be used for increasing the interlayer spacing between BN flakes, where specific molecules can be stored.

Originating from the chain structures, in Chapter 8 we described new two dimensional allotropes of carbon and boron nitride atoms, namely α-graphyne and α-BNyne. By performing both phonon frequency and finite temperature molecular dynamics analysis, we showed that both α-graphyne and α-BNyne are stable structures for even chains, but unstable for odd chains. We also calculated

the electronic structures for each of these materials and showed that α-graphyne structures have Dirac cones and their Fermi velocities decrease with increasing size. It is also implied that, all atoms being chemically equivalent is not a prerequisite for the existence of Dirac cones in the electronic structure. Upon hydrogenation, the Dirac cones are replaced by a large band gap. Since the formation of a single hydrogen vacancy renders a magnetic moment of 1 μ_B, magnetic nanomaterials can be designed by creation of domains of hydrogen vacancies. Our calculations of mechanical properties revealed α-graphyne and α-BNyne are not as stiff as graphene and the single layer h-BN, but they are strong enough to sustain the technological applications.

In Chapters 9, we diverge from graphene / boron nitride compounds to investigate other similar honeycomb-like structures which form the the second major part of the thesis. In the literature, one of the interesting experimental result that lacked theoretical explanation was the formation of layered silicene on certain substrates, which is crucial for future silicon technology. Although experimental observations made in several different research groups proved the existence of layered silicene; the mechanisms behind this layered structure was unknown. To this end, the new dumbbell structure of silicon atoms explained in Chapter 9 explained these experimental results. The dumbbell unit of silicon revealed in this theses is a cage-like orientation of silicon atoms in tetrahedral geometry, and form the building blocks of multilayer silicene. By covering the substrate with appropriate amounts and orientations of dumbbells; it becomes possible to obtain layered silicene. Our optimized layered silicene constructed from dumbbells match well with experimental results and explains the experimental data. Interestingly, it turns out that dumbbells exist not only on silicene, but also on other monolayer structures such as germanene, graphene and silicon-carbide.

In Chapter 10, we focus on new material design based on first principle simulations. First, we revealed a new honeycomb-like two dimensional material which forms after the oxygenation of silicene. We showed that a single oxygen atom can easily penetrate the silicene monolayer, but when silicene is bombarded with massive amounts of oxygen, single O atoms stay between the Si atoms, buckle the structure further and finally stabilize in a new orientation. We proved the stability of this new structure, which we name as silicatene, by means of ab-initio molecular dynamics calculations, phonon curves and total energy calculations.

Silicatene turns out to be a wide band gap semiconductor, which attains remarkable electromechanical properties showing geometrical changes under an external electric field. In particular, it is a material with a negative Poisson's ratio and has a high piezoelectric coefficient. The existence of this material was also confirmed by recent experimental studies, in which monolayer silicatene was grown on ruthenium surfaces covered by silicon carbide.

In the final section we focused on other possible two dimensional allotropes composed of Group V elements nitrogen and antimony, investigated various different 2D allotropes of these elements and revealed their stable forms using phonon calculations and molecular dynamics simulations at high temperatures. We predict that nitrogen can form single layer, buckled honeycomb structure called nitrogene, which is rigid and stable even above the room temperature. This 2D crystalline phase of nitrogen is a nonmagnetic insulator and rather inert due to the saturated π-bonds. Its zigzag and armchair nanoribbons have fundamental band gaps derived from reconstructed edge states. These band gaps are tunable with size and suitable for the emerging field of 2D electronics. Nitrogene forms not only bilayer, but also 3D graphitic multilayer structures. When grown on a substrate like Al(111) surface and graphene, nitrogene binds weakly to substrates and hence preserves its free standing properties, but it can easily be pealed off. Results of our ab-initio simulations and NEB[33] calculations suggest that nitrogene can nucleate at the edges of nitrogene and h-BN seeds. When grown on substrates, nitrogene interacts weakly even with reactive metal substrates and maintain the properties of free nitrogene. Similar analysis was also performed for monolayer structure of Sb atoms, resulting in a stable structure called antimonene.

Finally, this thesis reveals new fundamental properties of honeycomb structures, nanoscale device models and material predictions from ab-initio calculations. We hope our predictions and computational results presented in this thesis will be further confirmed by experimental studies in the near future

Bibliography

[1] K. S. Novoselov, A. K. Geim, S. V. Morozov, D. Jiang, Y. Zhang, S. V. Dubonos, I. V. Grigorieva, and A. A. Firsov, "Electric field effect in atomically thin carbon films," *Science*, vol. 306, pp. 666–669, 2004.

[2] K. Novoselov, D. Jiang, F. Schedin, T. Booth, V. Khotkevich, S. Morozov, and A. Geim, "Two-dimensional atomic crystals," *Proc. Natl. Acad. Sci. U.S.A.*, vol. 102, no. 30, pp. 10451–10453, 2005.

[3] A. K. Geim and K. S. Novoselov, "The rise of graphene," *Nat. Mater.*, vol. 6, no. 3, pp. 183–191, 2007.

[4] C. Darwin, "On the origins of species by means of natural selection," *London: Murray*, 1859.

[5] W. Paszkowicz, J. Pelka, M. Knapp, T. Szyszko, and S. Podsiadlo, "Lattice parameters and anisotropic thermal expansion of hexagonal boron nitride in the 10–297.5 k temperature range," *Applied Physics A*, vol. 75, no. 3, pp. 431–435, 2002.

[6] Z. Liu, L. Song, S. Zhao, J. Huang, L. Ma, J. Zhang, J. Lou, and P. M. Ajayan, "Direct growth of graphene/hexagonal boron nitride stacked layers," *Nano Lett.*, vol. 11, no. 5, pp. 2032–2037, 2011.

[7] K. Watanabe, T. Taniguchi, and H. Kanda, "Ultraviolet luminescence spectra of boron nitride single crystals grown under high pressure and high temperature," *Physica status solidi (a)*, vol. 201, no. 11, pp. 2561–2565, 2004.

[8] D. Pacile, J. Meyer, C. O. Girit, and A. Zettl, "The two-dimensional phase of boron nitride: Few-atomic-layer sheets and suspended membranes," *Appl. Phys. Lett.*, vol. 92, no. 13, pp. 133107–133107, 2008.

[9] N. G. Chopra, R. Luyken, K. Cherrey, V. H. Crespi, M. L. Cohen, S. G. Louie, and A. Zettl, "Boron nitride nanotubes," *Science*, vol. 269, no. 5226, pp. 966–967, 1995.

[10] Y. J. Chen, H. Z. Zhang, and Y. Chen, "Pure boron nitride nanowires produced from boron triiodide," *Nanotechnology*, vol. 17, no. 3, p. 786, 2006.

[11] C. Dean, A. Young, I. Meric, C. Lee, L. Wang, S. Sorgenfrei, K. Watanabe, T. Taniguchi, P. Kim, K. Shepard, *et al.*, "Boron nitride substrates for high-quality graphene electronics," *Nature nanotechnology*, vol. 5, no. 10, pp. 722–726, 2010.

[12] L. Ci, L. Song, C. Jin, D. Jariwala, D. Wu, Y. Li, A. Srivastava, Z. Wang, K. Storr, and L. Balicas, "Atomic layers of hybridized boron nitride and graphene domains," *Nat. Mater.*, vol. 9, no. 5, pp. 430–435, 2010.

[13] P. Zomer, S. Dash, N. Tombros, and B. Van Wees, "A transfer technique for high mobility graphene devices on commercially available hexagonal boron nitride," *Applied Physics Letters*, vol. 99, no. 23, p. 232104, 2011.

[14] M. Son, H. Lim, M. Hong, and H. C. Choi, "Direct growth of graphene pad on exfoliated hexagonal boron nitride surface," *Nanoscale*, vol. 3, no. 8, pp. 3089–3093, 2011.

[15] M. Wang, S. K. Jang, W.-J. Jang, M. Kim, S.-Y. Park, S.-W. Kim, S.-J. Kahng, J.-Y. Choi, R. S. Ruoff, Y. J. Song, *et al.*, "A platform for large-scale graphene electronics–cvd growth of single-layer graphene on cvd-grown hexagonal boron nitride," *Advanced Materials*, vol. 25, no. 19, pp. 2746–2752, 2013.

[16] Y. Gong, G. Shi, Z. Zhang, W. Zhou, J. Jung, W. Gao, L. Ma, Y. Yang, S. Yang, G. You, *et al.*, "Direct chemical conversion of graphene to boron- and nitrogen-and carbon-containing atomic layers," *Nature communications*, vol. 5, p. 3193, 2014.

[17] G. Shi, Y. Hanlumyuang, Z. Liu, Y. Gong, W. Gao, B. Li, J. Kono, J. Lou, R. Vajtai, P. Sharma, and P. Ajayan, "Boron nitride–graphene nanocapacitor and the origins of anomalous size-dependent increase of capacitance," *Nano letters*, vol. 14, no. 4, pp. 1739–1744, 2014.

[18] P. Hohenberg and W. Kohn, "Inhomogeneous electron gas," *Physical review*, vol. 136, no. 3B, p. B864, 1964.

[19] G. Kresse and J. Furthmuller, "Efficient iterative schemes for ab initio total-energy calculations using a plane-wave basis set," *Phys. Rev. B*, vol. 54, pp. 11169–11186, 1996.

[20] P. e. a. Giannozzi, "Quantum espresso: a modular and open-source software project for quantum simulations of materials," *J. Phys.: Condens. Matter*, vol. 21, p. 395502, 2009.

[21] J. M. Soler, E. Artacho, J. D. Gale, A. Garcia, J. Junquera, P. Ordejon, and D. Sanchez-Portal, "The siesta method for ab initio order-n materials simulation," *Journal of Physics: Condensed Matter*, vol. 14, no. 11, pp. 2745–2779, 2002.

[22] S. Grimme, "Semiempirical gga-type density functional constructed with a long-range dispersion correction.," *J. Comput. Chem.*, vol. 27, no. 15, pp. 1787–1799, 2006.

[23] D. Alfè, "Phon: A program to calculate phonons using the small displacement method," *Comp. Phys. Comm.*, vol. 180, no. 12, pp. 2622–2633, 2009.

[24] P. e. a. Giannozzi, "Quantum espresso: A modular and open-source software project for quantum simulations of materials.," *J. Phys.: Condens. Matter*, vol. 21, p. 395502, 2009.

[25] Y. Zhang, Y.-W. Tan, H. L. Stormer, and P. Kim, "Experimental observation of the quantum hall effect and berry's phase in graphene," *Nature*, vol. 438, no. 7065, pp. 201–204, 2005.

[26] Y. Zhang, J. P. Small, M. E. Amori, and P. Kim, "Electric field modulation of galvanomagnetic properties of mesoscopic graphite," *Physical review letters*, vol. 94, no. 17, p. 176803, 2005.

[27] J. S. Bunch, Y. Yaish, M. Brink, K. Bolotin, and P. L. McEuen, "Coulomb oscillations and hall effect in quasi-2d graphite quantum dots," *Nano letters*, vol. 5, no. 2, pp. 287–290, 2005.

[28] C. Berger, Z. Song, T. Li, X. Li, A. Y. Ogbazghi, R. Feng, Z. Dai, A. N. Marchenkov, E. H. Conrad, P. N. First, *et al.*, "Ultrathin epitaxial graphite:

2d electron gas properties and a route toward graphene-based nanoelectronics," *The Journal of Physical Chemistry B*, vol. 108, no. 52, pp. 19912–19916, 2004.

[29] P. E. Blochl, "Projector augmented-wave method," *Phys. Rev. B*, vol. 50, p. 17953, 1994.

[30] J. Perdew, J. Chevary, S. Vosko, K. Jakson, M. Pederson, M. Singh, and C. Fiolhais, "Atoms, molecules, solids, and surfaces: Applications of the generalized gradient approximation for exchange and correlation.," *Phys. Rev. B*, vol. 46, pp. 6671–6687, 1992.

[31] H. J. Monkhorst and J. D. Pack, "Special points for brillouin-zone integrations," *Phys. Rev. B*, vol. 13, no. 12, p. 5188, 1976.

[32] J. Kotakoski, J. Meyer, S. Kurasch, D. Santos-Cottin, U. Kaiser, and A. Krasheninnikov, "Stone-wales-type transformations in carbon nanostructures driven by electron irradiation," *Physical Review B*, vol. 83, no. 24, p. 245420, 2011.

[33] G. Henkelman, B. P. Uberuaga, and H. Jónsson, "A climbing image nudged elastic band method for finding saddle points and minimum energy paths," *J. Chem. Phys.*, vol. 113, no. 22, pp. 9901–9904, 2000.

[34] M. Winter and R. J. Brodd, "What are batteries, fuel cells, and supercapacitors?," *J. Chem. Rev.*, vol. 104, no. 10, pp. 4245–4270, 2004.

[35] A. G. Pandolfo and A. F. Hollenkamp, "Carbon properties and their role in supercapacitors," *Journal of Power Sources*, vol. 157, pp. 11–27, 2006.

[36] M. Toupin, T. Brousse, and D. Bélanger, "Charge storage mechanisms of mno_2 electrode used in aqueous electrochemical capacitor," *Chem. Mater.*, vol. 16, pp. 3184–3190, 2004.

[37] A. Rudge, J. Davey, I. Raistrick, S. Gottesfeld, and J. P. Ferraris, "Conducting polymers as active materials in electrochemical capacitors," *J. Power Sources*, vol. 47, no. 1-2, pp. 89–107, 1994.

[38] C. G. Liu, M. Liu, F. Li, and H. M. Cheng, "Frequency response characteristics of single-walled carbon nanotubes as supercapacitor electrode material," *Appl. Phys. Lett.*, vol. 92, p. 143108, 2008.

[39] C. M. Niu, E. Sichel, R. Hoch, D. Moy, and H. Tennent, "High power electrochemical capacitors based on carbon nanotube electrodes," *Appl. Phys. Lett.*, vol. 70, p. 1480, 1997.

[40] S. Yongchao and E. T. Samulski, "Exfoliated graphene separated by platinum nanoparticles," *Chem. Mater.*, vol. 20, pp. 6792–6797, 2008.

[41] M. D. Stoller, S. Park, Y. Zhu, J. An, and R. S. Ruoff, "Graphene-based supercapacitors," *Nano Lett.*, vol. 8, no. 10, pp. 3498–3502, 2008.

[42] S. R. C. Vivekchand, C. S. Rout, K. S. Subrahmanyam, A. Govindaraj, and C. N. Rao, "Graphene-based electrochemical supercapacitors," *J. Chem. Sci.*, vol. 120, no. 1, pp. 9–13, 2008.

[43] J. J. Yoo, K. Balakrishnan, J. Huang, V. Meunier, B. G. Sumpter, A. Srivastava, M. Conway, A. L. M. Reddy, J. Yu, R. Vajtai, and A. P. M., "Ultrathin planar graphene supercapacitors," *Nano Lett.*, vol. 11, pp. 1423–1427, 2011.

[44] Y. Wang, Z. Shi, Y. Huang, Y. Ma, C. Wang, M. Chen, and Y. Chen, "Supercapacitor devices based on graphene materials," *J. Phys. Chem. C*, vol. 113, pp. 13103–13107, 2009.

[45] A. Yu, I. Roes, A. Davies, and Z. Chen, "Ultrathin, transparent, and flexible graphene films for supercapacitor application," *Appl. Phys. Lett.*, vol. 96, p. 253105, 2010.

[46] M. Stengel and N. A. Spaldin, "Origin of the dielectric dead layer in nanoscale capacitors.," *Nature*, vol. 443, pp. 679–682, 2006.

[47] S. Sorel, U. Khan, and J. N. Coleman, "Flexible, transparent dielectric capacitors with nanostructured electrodes.," *Appl. Phys. Lett.*, vol. 101, p. 101106, 2012.

[48] K. K. Uprety, L. E. Ocola, and O. Auciello, "Growth and characterization of transparent pb(zi,ti)0_3 capacitor on glass substrate.," *J. Appl. Phys.*, vol. 102, p. 084107, 2007.

[49] J. Y. Lee, S. T. Connor, Y. Cui, and P. Peumans, "Solution-processed metal nanowire mesh transparent electrodes," *Nano Lett.*, vol. 8, no. 2, pp. 689–692, 2008.

[50] H. Tang and H. A. Sodano, "Ultra high energy density nanocomposite capacitors with fast discharge using nanowires," *Nano Lett.*, vol. 13, pp. 1373–1379, 2013.

[51] P. Kim, N. M. Doss, J. P. Tillotson, P. J. Hotchkiss, M. J. Pan, S. R. Marder, J. Li, J. P. Calame, and J. W. Perry, "High energy density nanocomposites based on surface modified $batio_3$ and a ferroelectric polymer," *ACS Nano*, vol. 3, pp. 2581–2592, 2009.

[52] H. Tang, Y. Lin, C. Andrews, and H. A. Sodano, "Nanocomposites with increased energy density through high aspect ratio pzt nanowires," *Nanotechnology*, vol. 22, p. 015702, 2011.

[53] K. T. Chan, H. Lee, and M. L. Cohen, "Gated adatoms on graphene studied with first-principles calculations," *Phys. Rev. B*, vol. 83, p. 035405, 2011.

[54] K. T. Chan, H. Lee, and M. L. Cohen, "Possibility of transforming the electronic structure of one species of graphene adatoms into that of another by application of gate voltage: First-principles calculations," *Phys. Rev. B*, vol. 84, p. 165419, 2011.

[55] A. M. Suarez, L. R. Radovic, E. Bar-Ziv, and J. O. Sofo, "Gate-voltage control of oxygen diffusion on graphene," *Phys. Rev. Lett.*, vol. 106, p. 146802, 2011.

[56] M. Topsakal and S. Ciraci, "Effects of static charging on exfoliation of layered crystals," *Phys. Rev. B*, vol. 85, p. 045121, 2012.

[57] M. Topsakal, H. H. Gurel, and S. Ciraci, "Effects of charging and electric field on graphene oxide," *J.Phys. Chem. C.*, vol. 117, p. 5943, 2013.

[58] J. P. Perdew, K. Burke, and M. Ernzerhof, "Generalized gradient approximation made simple," *Phys. Rev. Lett.*, vol. 77, pp. 3865–3868, 1996.

[59] N. Troullier and J. L. Martins, "Efficient pseudopotentials for plane-wave calculations," *Phys. Rev. B*, vol. 43, pp. 1993–2006, 1991.

[60] G. Markov and M. C. Payne, "Periodic boundary conditions in ab initio calculations," *Phys. Rev. B*, vol. 51, pp. 4014–4022, 1995.

[61] C. Ataca, M. Topsakal, E. Akturk, and S. Ciraci, "A comparative study of lattice dynamics of three- and two-dimensional mos_2.," *J. Phys. Chem. C*, vol. 115, no. 33, pp. 16354–16361, 2011.

[62] M. Topsakal, E. Aktürk, and S. Ciraci, "First-principles study of two and one dimensional honeycomb structures of boron nitride," *Phys. Rev. B*, vol. 79, p. 115442, 2009.

[63] H. Sahin, S. Cahangirov, M. Topsakal, E. Bekaroglu, E. Akturk, R. Senger, and S. Ciraci, "Monolayer honeycomb structures of group-iv elements and iii-v binary compounds: First-principles calculations.," *Phys. Rev. B*, vol. 80, p. 155453, 2009.

[64] C. Ataca, H. Sahin, E. Akturk, and S. Ciraci, "Mechanical and electronic properties of mos2 nanoribbons and their defects.," *J. Phys. Chem. C*, vol. 115, no. 10, pp. 3934–3941, 2011.

[65] R. Geick, C. H. Perry, and G. Ruppercht, "Normal modes in hexagonal boron nitride," *Phys. Rev.*, vol. 146, pp. 543–547, 1966.

[66] J. Li and V. B. Shenoy, "Graphene quantum dots embedded in hexagonal boron nitride sheets," *Appl. Phys. Lett.*, vol. 98, no. 1, p. 013105, 2011.

[67] J. He, K.-Q. Chen, Z.-Q. Fan, L.-M. Tang, and W. Hu, "Transition from insulator to metal induced by hybridized connection of graphene and boron nitride nanoribbons," *Appl. Phys. Lett.*, vol. 97, no. 19, p. 193305, 2010.

[68] J. Bai, X. Zhong, S. Jiang, Y. Huang, and X. Duan, "Graphene nanomesh," *Nat. Nanotechnol.*, vol. 5, no. 3, pp. 190–194, 2010.

[69] J. Lahiri, Y. Lin, P. Bozkurt, I. I. Oleynik, and M. Batzill, "An extended defect in graphene as a metallic wire," *Nat. Nanotechnol.*, vol. 5, no. 5, pp. 326–329, 2010.

[70] R. Balog, B. Jorgensen, L. Nilsson, M. Andersen, E. Rienks, M. Bianchi, M. Fanetti, E. Lægsgaard, A. Baraldi, and S. Lizzit, "Bandgap opening in graphene induced by patterned hydrogen adsorption," *Nat. Mater.*, vol. 9, no. 4, pp. 315–319, 2010.

[71] Z. Yu, M. Hu, C. Zhang, C. He, L. Sun, and J. Zhong, "Transport properties of hybrid zigzag graphene and boron nitride nanoribbons," *J. Phys. Chem. C*, vol. 115, no. 21, pp. 10836–10841, 2011.

[72] M. P. Levendorf, C.-J. Kim, L. Brown, P. Y. Huang, R. W. Havener, D. A. Muller, and J. Park, "Graphene and boron nitride lateral heterostructures for atomically thin circuitry," *Nature*, vol. 488, no. 7413, pp. 627–632, 2012.

[73] J. Jung, Z. Qiao, Q. Niu, and A. H. MacDonald, "Transport properties of graphene nanoroads in boron nitride sheets," *Nano Lett.*, vol. 12, no. 6, pp. 2936–2940, 2012.

[74] Y. Lin and J. W. Connell, "Advances in 2d boron nitride nanostructures: Nanosheets, nanoribbons, nanomeshes, and hybrids with graphene," *Nanoscale*, vol. 4, no. 22, pp. 6908–6939, 2012.

[75] R. Drost, A. Uppstu, F. Schulz, S. K. Hamalainen, M. Ervasti, A. Harju, and P. Liljeroth, "Electronic states at the graphene–hexagonal boron nitride zigzag interface," *Nano Lett.*, vol. 14, no. 9, pp. 5128–5132, 2014.

[76] H. Lim, S. I. Yoon, G. Kim, A.-R. Jang, and H. S. Shin, "Stacking of two-dimensional materials in lateral and vertical directions," *Chem. Mater.*, vol. 26, no. 17, pp. 4891–4903, 2014.

[77] Z. Liu, L. Ma, G. Shi, W. Zhou, Y. Gong, S. Lei, X. Yang, J. Zhang, J. Yu, and K. P. Hackenberg, "In-plane heterostructures of graphene and hexagonal boron nitride with controlled domain sizes," *Nat. Nanotechnol.*, vol. 8, no. 2, pp. 119–124, 2013.

[78] L. Song, L. Balicas, D. J. Mowbray, R. B. Capaz, K. Storr, L. Ci, D. Jariwala, S. Kurth, S. G. Louie, and A. Rubio, "Anomalous insulator-metal transition in boron nitride-graphene hybrid atomic layers," *Phys. Rev. B*, vol. 86, no. 7, p. 075429, 2012.

[79] Y. Liu, X. Wu, Y. Zhao, X. C. Zeng, and J. Yang, "Half-metallicity in hybrid graphene/boron nitride nanoribbons with dihydrogenated edges," *J. Phys. Chem. C*, vol. 115, no. 19, pp. 9442–9450, 2011.

[80] V. O. Özçelik and S. Ciraci, "Nanoscale dielectric capacitors composed of graphene and boron nitride layers: A first-principles study of high capacitance at nanoscale," *J. Phys. Chem. C*, vol. 117, no. 29, pp. 15327–15334, 2013.

[81] L. Chang, L. Esaki, and R. Tsu, "Resonant tunneling in semiconductor double barriers," *Appl. Phys. Lett.*, vol. 24, no. 12, pp. 593–595, 1974.

[82] H. H. Gürel, V. O. Özçelik, and S. Ciraci, "Effects of charging and perpendicular electric field on the properties of silicene and germanene," *J. Phys. Condens. Matter*, vol. 25, no. 30, p. 305007, 2013.

[83] J. Paier, M. Marsman, K. Hummer, G. Kresse, I. C. Gerber, and J. G. Ángyán, "Screened hybrid density functionals applied to solids," *J. Chem. Phys.*, vol. 124, no. 15, p. 154709, 2006.

[84] A. V. Krukau, O. A. Vydrov, A. F. Izmaylov, and G. E. Scuseria, "Influence of the exchange screening parameter on the performance of screened hybrid functionals," *J. Chem. Phys.*, vol. 125, p. 224106, December 2006.

[85] Y.-W. Son, M. L. Cohen, and S. G. Louie, "Energy gaps in graphene nanoribbons," *Phys. Rev. Lett.*, vol. 97, no. 21, p. 216803, 2006.

[86] C. Ataca, H. Sahin, and S. Ciraci, "Stable, single-layer mx_2 transition metal oxides and dichalcogenides in a honeycomb-like structure," *J. Phys. Chem. C*, vol. 116, no. 16, pp. 8983–8999, 2012.

[87] Z. Ao, A. Hernandez-Nieves, F. Peeters, and S. Li, "The electric field as a novel switch for uptake / release of hydrogen for storage in nitrogen doped graphene," *Phys. Chem. Chem. Phys.*, vol. 14, no. 4, pp. 1463–1467, 2012.

[88] Z. Ao and F. Peeters, "Electric field activated hydrogen dissociative adsorption to nitrogen-doped graphene," *J. Phys. Chem. C*, vol. 114, no. 34, pp. 14503–14509, 2010.

[89] J. Zhou, M. M. Wu, X. Zhou, and Q. Sun, "Tuning electronic and magnetic properties of graphene by surface modification," *App. Phys. Lett.*, vol. 95, no. 10, p. 103108, 2009.

[90] Z. Wang, "Alignment of graphene nanoribbons by an electric field," *Carbon*, vol. 47, no. 13, pp. 3050–3053, 2009.

[91] Z. Osvath, F. Lefloch, V. Bouchiat, and C. Chapelier, "Electric field-controlled rippling of graphene," *Nanoscale*, vol. 5, no. 22, pp. 10996–11002, 2013.

[92] Y.-J. Yu, Y. Zhao, S. Ryu, L. E. Brus, K. S. Kim, and P. Kim, "Tuning the graphene work function by electric field effect," *Nano Lett.*, vol. 9, no. 10, pp. 3430–3434, 2009.

[93] S. Cahangirov, M. Topsakal, E. Aktürk, H. Şahin, and S. Ciraci, "Two- and one-dimensional honeycomb structures of silicon and germanium," *Phys. Rev. Lett.*, vol. 102, p. 236804, Jun 2009.

[94] M. G. Menezes and R. B. Capaz, "Half-metallicity induced by charge injection in hexagonal boron nitride clusters embedded in graphene," *Phys. Rev. B*, vol. 86, no. 19, p. 195413, 2012.

[95] S. Tang and X. Cao, "Realizing semiconductor half-metal transition in zigzag graphene nanoribbons supported on hybrid fluorographene graphane nanoribbons," *Phys. Chem. Chem. Phys.*, vol. 16, no. 42, pp. 23214–23223, 2014.

[96] A. Abdurahman, A. Shukla, and G. Seifert, "*Ab initio* many-body calculations of static dipole polarizabilities of linear carbon chains and chainlike boron clusters," *Phys. Rev. B*, vol. 66, p. 155423, Oct 2002.

[97] S. Tongay, R. T. Senger, S. Dag, and S. Ciraci, "*ab-initio* electron transport calculations of carbon based string structures," *Phys. Rev. Lett.*, vol. 93, p. 136404, 2004.

[98] S. Tongay, S. Dag, E. Durgun, R. Senger, and S. Ciraci, "Atomic and electronic structure of carbon strings," *J. Phys. Condens. Matter*, vol. 17, no. 25, p. 3823, 2005.

[99] S. Eisler, D. Aaron, E. Elliott, T. Luu, R. McDonald, F. A. Hegmann, and R. R. Tykwinski, "Polyynes as a model for carbyne: synthesis, physical properties, and nonlinear optical response," *J. Am. Chem. Soc.*, vol. 127, pp. 2666–26676, 2005.

[100] C. Jin, H. Lan, L. Peng, K. Suenaga, and S. Iijima, "Deriving carbon atomic chains from graphene," *Phys. Rev. Lett.*, vol. 102, p. 205501, May 2009.

[101] W. A. Chalifoux and R. R. Tykwinski, "Synthesis of polyynes to model the sp-carbon allotrope carbyne," *Nature Chem.*, vol. 2, pp. 967–971, 2010.

[102] J. C. Meyer, C. O. Girit, M. Crommie, and A. Zettl, "Imaging and dynamics of light atoms and molecules on graphene," *Nature*, vol. 454, no. 7202, pp. 319–322, 2008.

[103] R. H. Baughman, H. Eckhardt, and M. J. Kertesz, "Structureproperty predictions for new planar forms of carbon: Layered phases containing sp2 and sp atoms," *J. Chem. Phys.*, vol. 87, pp. 6687–6698, 1987.

[104] D. Malko, C. Neiss, F. Vines, and A. Gorling, "Competition for graphene: Graphynes with direction-dependent dirac cones," *Phys. Rev. Lett.*, vol. 108, p. 086804, 2012.

[105] A. Hirsch, "The era of carbon allotropes," *Nature Mater.*, vol. 9, pp. 868–871, 2010.

[106] F. Diederich, "Carbon scaffolding: building acetylenic all-carbon and carbon-rich compounds," *Nature (London)*, vol. 369, pp. 199–207, 1994.

[107] F. Diederich and M. Kivala, "All-carbon scaffolds by rational design," *Adv. Mater.*, vol. 22, pp. 803–812, 2010.

[108] M. M. Haley, "Synthesis and properties of annulenic subunits of graphyne and graphdiyne nanoarchitectures," *Pure Appl. Chem.*, vol. 80, no. 3, pp. 519–532, 2008.

[109] J. M. Kehoe, J. H. Kiley, J. J. English, C. A. Johnson, R. C. Petersen, and M. M. Haley, "Synthesis of graphyne substructures," *Org. Lett.*, vol. 2, pp. 969–972, 2000.

[110] N. Narita, S. Nagai, S. Suzuki, and K. Nakao, "Optimized geometries and electronic structures of graphyne and its family," *Phys. Rev. B*, vol. 58, pp. 11009–11014, 1998.

[111] V. R. Coluci, S. F. Braga, S. B. Legoas, D. S. Galvao, and R. H. Baughman, "Families of carbon nanotubes: Graphyne-based nanotubes," *Phys. Rev. B*, vol. 68, p. 035430, 2003.

[112] J. Zhou, K. Lv, Q. Wang, X. S. Chen, Q. Sun, and P. Jena, "," *J. Chem. Phys.*, vol. 134, p. 174701, 2011.

[113] L. D. Pan, L. Z. Zhang, B. Q. Song, S. X. Du, and H. J. Gao, "," *Appl. Phys. Lett.*, vol. 98, p. 173102, 2011.

[114] S. Cahangirov, M. Topsakal, and S. Ciraci, "Long-range interactions in carbon atomic chains," *Phys. Rev. B*, vol. 82, p. 195444, 2010.

[115] M. Topsakal, S. Cahangirov, and S. Ciraci, "The response of mechanical and electronic properties of graphane to the elastic strain," *Appl. Phys. Lett.*, vol. 96, p. 091912, 2010.

[116] S. W. Cranford and M. J. Buehler, "Mechanical properties of graphyne," *Carbon*, vol. 49, pp. 4111–4121, 2011.

[117] J. Kang, J. Li, F. Wu, S. S. Li, and J. B. Xia, "Elastic, electronic, and optical properties of two-dimensional graphyne sheet," *J. Phys. Chem. C*, vol. 115, pp. 20466–20470, 2011.

[118] H. Sahin and S. Ciraci, "Structural, mechanical, and electronic properties of defect-patterned graphene nanomeshes from first principle," *Phys. Rev. B*, vol. 84, p. 035452, 2011.

[119] T. Björkman, A. Gulans, A. V. Krasheninnikov, and R. M. Nieminen, "Helicity in ropes of chiral nanotubes: Calculations and observation," *Phys. Rev. Lett.*, vol. 108, p. 235501, 2012.

[120] B. Partoens and F. M. Peeters, "From graphene to graphite: Electronic structure around the k point," *Phys. Rev. B*, vol. 74, p. 075404, 2006.

[121] S. Lebegue and O. Ericson, "Electronic structure of two-dimensional crystals from ab initio theory," *Phys. Rev. B*, vol. 79, p. 115409, 2009.

[122] J. C. Garcia, D. B. de Lima, L. V. C. Assali, and J. F. Justo, "Group iv graphene- and graphane-like nanosheets," *J. Phys. Chem. C*, vol. 115, p. 13242, 2011.

[123] J. Bai, H. Tanaka, and X. C. Zeng, "Graphene-like bilayer hexagonal silicon polymorph," *Nano Res.*, vol. 3, p. 694, 2010.

[124] T. Suzuki and Y. Yokomizo, "Energy bands of atomic monolayers of various materials: Possibility of energy gap engineering," *Physica E: Low-dimensional Systems and Nanostructures*, vol. 42, no. 10, pp. 2820–2825, 2010.

[125] L. Pan, H. J. Liu, Y. W. Wen, X. J. Tan, H. Y. Lv, J. Shi, and X. F. Tang, "First-principles study of monolayer and bilayer honeycomb structures of group-iv elements and their binary compounds," *Phys. Lett. A*, vol. 375, p. 614, 2011.

[126] S. Wang, "A comparative first-principles study of orbital hybridization in two-dimensional c, si, and ge," *Phys. Chem. Chem. Phys.*, vol. 13, p. 11929, 2011.

[127] S. Cahangirov, M. Audiffred, P. Tang, A. Iacomino, W. Duan, G. Merino, and A. Rubio, "Electronic structure of silicene on ag(111): Strong hybridization effects," *Phys. Rev. B*, vol. 88, p. 035432, 2013.

[128] B. Aufray, A. Kara, S. Vizzini, H. Oughaddou, C. Leandri, B. Ealet, and G. Le Lay, "Evidence of graphene-like electronic signature in silicene nanoribbons," *Appl. Phys. Lett.*, vol. 96, p. 261905, 2010.

[129] P. Vogt, P. De Padova, C. Quaresima, J. Avila, E. Frantzeskakis, M. C. Asensio, A. Resta, E. B., and G. Le Lay, "Silicene: Compelling experimental evidence for graphenelike two-dimensional silicon," *Phys. Rev. Lett.*, vol. 108, p. 155501, 2012.

[130] P. D. Padova, C. Ottaviani, C. Quaresima, B. Olivieri, P. Imperatori, E. Salomon, T. Angot, L. Quagliano, C. Romano, and A. V. et al, "24h stability of thick multilayer silicene in air," *2D Mater.*, vol. 1, no. 2, p. 021003, 2014.

[131] C. C. Liu, H. Jiang, and Y. Yao, "Low-energy effective hamiltonian involving spin-orbit coupling in silicene and two-dimensional germanium and tin," *Phys. Rev. B*, vol. 84, p. 195430, 2011.

[132] L. Li, S.-z. Lu, J. Pan, Z. Qin, Y.-q. Wang, Y. Wang, G.-y. Cao, S. Du, and H.-J. Gao, "Buckled germanene formation on pt (111)," *Advanced Materials*, vol. 26, no. 28, pp. 4820–4824, 2014.

[133] V. O. Özçelik, H. H. Gurel, and S. Ciraci, "Self-healing of vacancy defects in single-layer graphene and silicene," *Phys. Rev. B*, vol. 88, no. 4, p. 045440, 2013.

[134] C. Ataca, E. Akturk, H. Sahin, and S. Ciraci, "Adsorption of carbon adatoms to graphene and its nanoribbons," *J. Appl. Phys*, vol. 109, p. 013704, 2011.

[135] W. A. Harrison and S. Ciraci, "Bond-orbital model ii," *Phys. Rev. B*, vol. 10, p. 1516, 1974.

[136] C. Ataca and S. Ciraci, "Perpendicular growth of carbon chains on graphene from first-principles," *Phys. Rev. B*, vol. 83, p. 235417, 2011.

[137] V. O. Özçelik and S. Ciraci, "Self-assembly mechanisms of short atomic chains on single-layer graphene and boron nitride," *Phys. Rev. B*, vol. 86, p. 155421, 2012.

[138] D. Kaltsas and L. Tsetseris, "Stability and electronic properties of ultra-thin films of silicon and germanium," *Phys. Chem. Chem. Phys.*, vol. 15, pp. 9710–9715, 2013.

[139] L. Li, Y. Yu, G. J. Ye, Q. Ge, X. Ou, H. Wu, D. Feng, X. H. Chen, and Y. Zhang, "Black phosphorus field-effect transistors," *Nat. Nanotech.*, vol. 9, no. 5, pp. 372–377, 2014.

[140] Z. Zhu and D. Tománek, "Semiconducting layered blue phosphorus: A computational study," *Phys. Rev. Lett.*, vol. 112, no. 17, p. 176802, 2014.

[141] T. Low, A. Rodin, A. Carvalho, Y. Jiang, H. Wang, F. Xia, and A. C. Neto, "Tunable optical properties of multilayer black phosphorus thin films," *Phys. Rev. B*, vol. 90, no. 7, p. 075434, 2014.

[142] V. E. Bottom, "Measurement of the piezoelectric coefficient of quartz using the fabry-perot dilatometer," *Journal of Applied Physics*, vol. 41, no. 10, pp. 3941–3944, 1970.

[143] R. Mills and A. Schuch, "Crystal structure of gamma nitrogen," *Phys. Rev. Lett.*, vol. 23, no. 20, p. 1154, 1969.

[144] W. Nellis, N. Holmes, A. Mitchell, and M. Van Thiel, "Phase transition in fluid nitrogen at high densities and temperatures," *Phys. Rev. Lett.*, vol. 53, no. 17, p. 1661, 1984.

[145] A. McMahan and R. LeSar, "Pressure dissociation of solid nitrogen under 1 mbar," *Phys. Rev. Lett.*, vol. 54, no. 17, p. 1929, 1985.

[146] C. Mailhiot, L. Yang, and A. McMahan, "Polymeric nitrogen," *Phys. Rev. B*, vol. 46, no. 22, p. 14419, 1992.

[147] L. Mitáš and R. M. Martin, "Quantum monte carlo of nitrogen: Atom, dimer, atomic, and molecular solids," *Phys. Rev. Lett.*, vol. 72, no. 15, p. 2438, 1994.

[148] E. Gregoryanz, A. F. Goncharov, R. J. Hemley, H.-k. Mao, M. Somayazulu, and G. Shen, "Raman, infrared, and x-ray evidence for new phases of nitrogen at high pressures and temperatures," *Phys. Rev. B*, vol. 66, no. 22, p. 224108, 2002.

[149] M. I. Eremets, R. J. Hemley, H.-k. Mao, and E. Gregoryanz, "Semiconducting non-molecular nitrogen up to 240 gpa and its low-pressure stability," *Nature*, vol. 411, no. 6834, pp. 170–174, 2001.

[150] M. I. Eremets, A. G. Gavriliuk, I. A. Trojan, D. A. Dzivenko, and R. Boehler, "Single-bonded cubic form of nitrogen," *Nat. Mater.*, vol. 3, no. 8, pp. 558–563, 2004.

[151] O. V. Yazyev and L. Helm, "Defect-induced magnetism in graphene," *Phys. Rev. B*, vol. 75, no. 12, p. 125408, 2007.

[152] A. W. Robertson, B. Montanari, K. He, C. S. Allen, Y. A. Wu, N. M. Harrison, A. I. Kirkland, and J. H. Warner, "Structural reconstruction of the graphene monovacancy," *ACS Nano*, vol. 7, no. 5, pp. 4495–4502, 2013.

[153] E. H. Lieb, "Two theorems on the hubbard model," *Phys. Rev. Lett.*, vol. 62, pp. 1201–1204, Mar 1989.

[154] C. Barrett, P. Cucka, and K. Haefner, "The crystal structure of antimony at 4.2, 78 and 298 k," *Acta Crystallographica*, vol. 16, no. 6, pp. 451–453, 1963.

[155] E. Durgun, S. Tongay, and S. Ciraci, "Silicon and iii-v compound nanotubes: Structural and electronic properties," *Phys. Rev. B*, vol. 72, p. 075420, Aug 2005.